Design, Synthesis, and Characterization of Aluminum(III) Porphyrin Assemblies for use in Photochemical Cells

A thesis submitted to the University of Minnesota by

Benjamin Gabriel Boe

In partial fulfillment of the requirements for the degree of Master of Science

Advisor: Dr. Prashanth K. Poddutoori

May 2020

ACKNOWLEDGEMENTS:

Modern research is a team sport, and it is wise for any aspiring scientist, no matter how solitary their work, to acknowledge the friends and colleagues that make it possible. My own small successes at UMD have been enable by countless direct and indirect contributions, only some of which I have the space to acknowledge.

This work was supported in part through the UMD Siders Graduate fellowship, established in 2006 in honor of Frances Siders, Charles Siders, and Mary Siders Carson, in acknowledgment of their lifelong dedication to education and personal initiative.

I want to thank Dr. Prashanth Kumar Poddutoori, on whose expertise the work in this document was built. I have the privilege of being Dr. Poddutoori's first graduate student researcher, and fully expect to be the first in a long line of scientists to benefit from Dr. Poddutoori's generous instruction and painstaking standards of quality.

Additional thanks to the rest of the Poddutoori Research Group: thank you Noah Holzer, for doing a fantastic job of cleaning the NMR tubes which I almost never "borrowed". Thanks to Brandon Bayard for providing software support at a crucial juncture. And especial thanks go to one of my oldest UMD graduate program colleagues, Michael Shea; Michael, your synthetic expertise was always on point, your personal and emotional support were always timely, and your height was never threatening.

On a personal level, I will forever be grateful to all the people that make up the UMD Chemistry graduate program. I'm indebted both personally and professionally to more people than I can name here. Thank you to Alvin Burrows and Maeve Ryan for giving me a second home and, occasionally, a third office. Thank you to Dr. Paul Siders; it was an honor to work for you. Dr. Wainman, thank you for always offering me 15 minutes of your time, and not getting too irritated when I took 50.

Finally, this work would not have been possible without the constant and continuing support of the indefatigable Roxanna Boe who, in addition to filling many roles in her life (e.g., being my mother), has performed the indispensable task of taking care of my cat, Yuki, while I was away doing science-things.

Abstract:

A series of axially-coordinated aluminum(III) porphyrins were synthesized and evaluated as potential photosensitizers of a ruthenium-based water oxidation catalyst. The porphyrins themselves are 5,10,15,20-tetraphenylporphyrins, and differ in the degree of fluorination on the peripheral phenyl groups. These aluminum(III) porphyrins readily assemble into catalytic dyads through formation of a covalent ester linkage between the central aluminum atom of the porphyrin and a terminal carboxyl group on the ruthenium catalyst. The aluminum center is also able to act as a Lewis acid, forming the final triad by way of a coordinate bond with a suitable Lewis base.

Catalytic dyads were successfully synthesized from all three porphyrins in the series; a set of control compounds were also prepared. The dyads and reference molecules were then characterized, with molecular structure and successful formation of the dyads being confirmed with proton NMR spectroscopy, optical properties assessed with respect to UV-Vis absorption and fluorescence spectroscopy, and redox potentials being assessed by both cyclic and differential pulse voltammetry. Formation of the final triad was achieved by titration of the catalytic dyads with a C_{60} fullerene functionalized to act as a Lewis base; absorption and fluorescence spectra were monitored during titration, allowing for confirmation of the triad formation, as well as calculation of binding constants. The characterization data were used to construct energy level diagrams, laying the groundwork for a theoretical abstraction of these molecule's functioning. the catalytic systems as synthesized, as well as how they might function in a prototypical photochemical cell.

Analysis of the results reveal these materials to be promising candidates as photoactivated water oxidation catalysts. The absorption and electrochemical data demonstrate that, when the catalytic dyads are formed, the electronic structure of the constituent parts is preserved. The fluorescence spectra of the dyads show significant quenching relative to the reference porphyrins. Control studies allowed for the exclusion of intermolecular processes as being the source of this quenching, and therefore the optically excited porphyrin must be able to interact with the attached ruthenium catalyst, either through energy or electron transfer. Based on the negligible overlap of the spectra of the catalyst with that of the porphyrins, energy transfer is unlikely. The most likely source of the fluorescence quenching is therefore electron transfer across the ester-bond. The formation and persistence of such a radical ion pair is a fundamental prerequisite for the material to function as a water oxidation catalyst, as it is on this charge-separated species that water oxidation proceeds. Coordination of the dyads with a fullerene ligand was similarly demonstrated, with the resulting triad exhibiting complete fluorescence quenching. The fullerene ligand itself was chosen specifically for its suitability as an electron acceptor, and once again the most likely cause of this quenching is intramolecular electron transfer.

TABLE OF CONTENTS

LIST OF TABLES

LIST OF FIGURES

LIST OF REACTION SCHEMES

CHAPTER 1: INTRODUCTION

1.1 THE NEED FOR GREEN ENERGY SOLUTIONS

The need for green energy solutions has become self-evident; heavy reliance on the combustion of fossil fuels as an energy source have contributed to global warming and pollution, primarily through the production of carbon dioxide.[1,2] Solar energy is an attractive solution for several reasons: energy from the sun is abundant, free, and available anywhere on the planet. The total amount of energy from the sun that strikes the earth is approximately 101 terawatts, more than 6 times the total amount of power the world's civilizations consume. However, practical concerns limit the amount of this light that can be reasonably harnessed. The sun does not shine all day; additionally, the actual light hitting the ground (and therefore a prospective solar device) is affected by weather, shade, and varies in intensity across the globe. Moreover, sunlight is diffuse and intermittent, and the use of solar energy for our needs requires energy storage in dense, transportable media via chemical energy. Such factors intensify the need for the concurrent development of green energy storage solutions.[3]

1.2 H_2 AS A CLEAN-BURNING FUEL

In terms of the production of greenhouse gases, diatomic hydrogen is an ideal alternative to fossil fuels, for the following reason: all hydrocarbons produce carbon dioxide and water as the products of combustion (Equation 1), whereas the burning of H_2 produces only water as a byproduct (Equation 2).

$$CH_4 + 2O_2 \rightarrow CO_2 + 2H_2O \qquad (1)$$

$$H_2 + \frac{1}{2}O_2 \rightarrow H_2O \qquad (2)$$

The use of hydrogen as a fuel is not a new concept, and discussions of a prospective “hydrogen economy” date back to at least the 1970’s.[4,5,6] The consumption end of this economy is well-developed; NASA has successfully used hydrogen as a combustible rocket fuel since the Centaur rocket-powered missions in the 1970’s.[7] At the consumer level, several hydrogen fuel based cars are currently available.[8,9]

Currently, the majority of domestic hydrogen gas production comes from natural gas reforming.[10] Through a series of two processes (represented by Equation 3 and Equation 4 below), natural gas reforming turns methane and water into hydrogen gas. However, as can be seen, the process still produces carbon dioxide as a byproduct.

Partial oxidation of methane: $$CH_4 + \frac{1}{2}O_2 \rightarrow CO + 2H_2 \qquad (3)$$

Water-gas shift: $$CO + H_2O \rightarrow CO_2 + H_2 \qquad (4)$$

The production of hydrogen gas from water eliminates carbon dioxide from the production step of hydrogen gas production. Electrolysis of water is a straightforward process first achieved in the 18th century (depicted in Figure 1).[11] However, this process is driven by the application of a voltage source, and therefore, the process as a whole is only as clean as the process that produces those voltage sources.

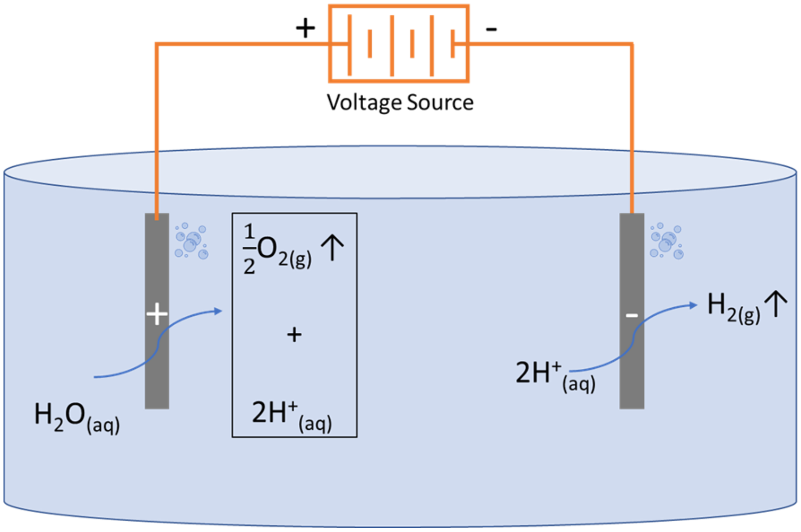

Figure 1. General overview of the Electrolysis of water.

1.3 PHOTOCHEMICAL CELLS

In contrast to photovoltaic cells, photochemical cells use solar energy to do chemical work directly, i.e. to drive otherwise unfavorable reactions. This removes the intermediate step of storing energy in batteries; as illustrated in Figure 2, the energy stored in the battery in the photovoltaic cell can subsequently be used to drive the production of hydrogen gas from water. However, the photochemical cell drives the reaction directly.

In a photochemical cell water oxidation cell, the splitting of water into its constituent elements is directly driven by solar energy. In such a photochemical cell, solar energy is used to drive the chemical reaction described in Equation 5 below; electrons are removed from H_2O, splitting the water molecule into the constituent elements of hydrogen (as solvated protons) and oxygen (as the diatomic gas).

Water Oxidation: $$H_2O_{(l)} \rightarrow 2\,e^- + 2\,H^+_{(aq)} + \frac{1}{2}O_{2\,(g)} \quad (5)$$

Hydrogen Reduction: $$2H^+_{(aq)} + 2\,e^- \rightarrow H_{2\,(g)} \quad (6)$$

Equation 6 describes the subsequent step, which involves recombining the protons and electrons to produce hydrogen gas. The oxidation step in this process is significantly more energetically demanding than the recombination of electrons and protons (E° = 0 eV for hydrogen reduction, E° = 1.23 eV for water oxidation).[12]

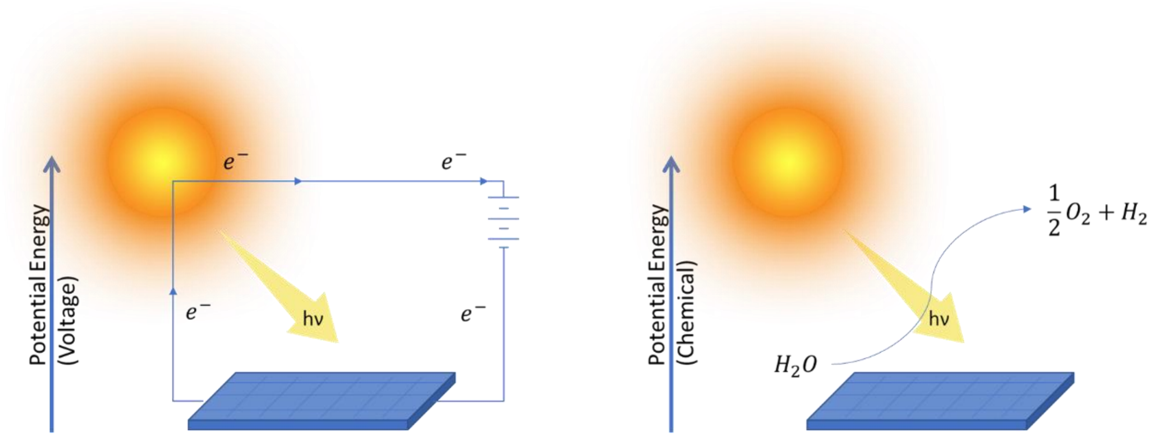

Figure 2. Potential energy storage for a photovoltaic (left) and photochemical (right) cell.

1.4 RUTHENIUM WATER OXIDATION CATALYSTS

The first ruthenium-based water oxidation catalyst (WOC) was reported by Meyer in 1981. This consisted of an oxo-bridged dimer of ruthenium(III), commonly referred to as “Meyer’s Blue Dimer” (Figure 3a).[13]

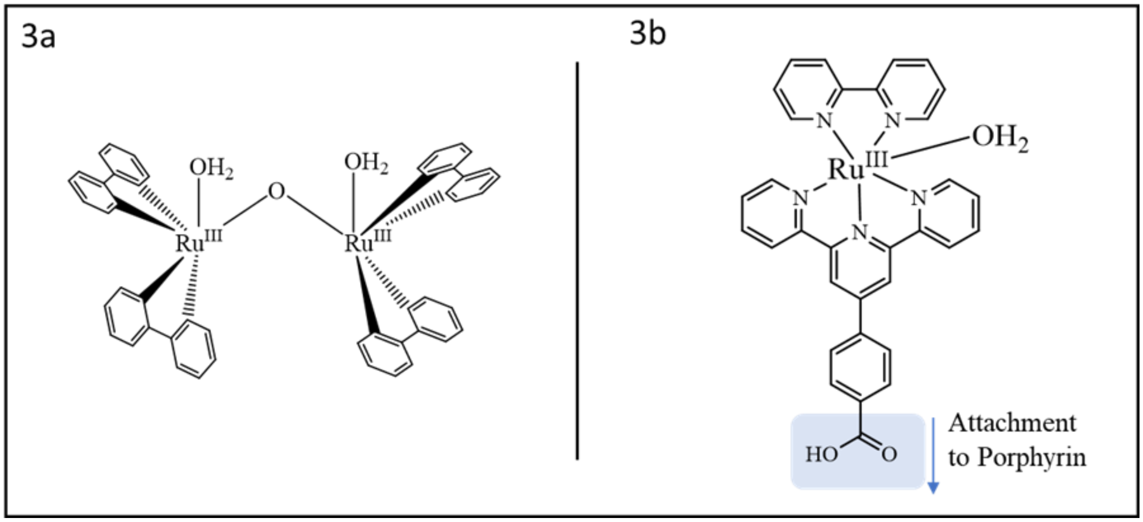

Figure 3. Left: Meyer's "blue dimer". Right: the catalyst used in this work. The carboxyl group serves as a point of attachment for the formation of a dyad (described below).

Subsequently, Meyer & others have described several mononuclear ruthenium catalysts based on some form of polypyridyl framework. Ruthenium-based water oxidation is a multistep process, involving a cycling of the metal redox state ranging from +2 to +5. The catalyst must remain stable under these conditions, and a scaffolding of coordinated polypyridyl structures have proven to be suitable for this purpose.[14, 15]

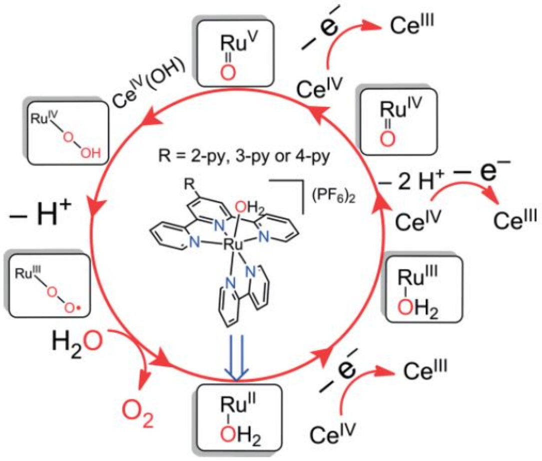

Figure 4. Multi-electron steps mediating water oxidation by a ruthenium catalyst.[14]

The design of the ruthenium catalyst described in this work is to allow structural attachment to a photosensitizer, (specifically, the series of aluminum porphyrins described below in section 1.6), without interfering with catalytic functioning. This attachment occurs via a carboxyl group on a peripheral phenyl ring (Figure 3b). Evidence for the success of this design goal is given in part in this work, and discussed further in Section 1.7, as well as Chapter 2 and Chapter 3.

1.6 ALUMINUM(III) PORPHYRINS

1.6.1 PORPHYRIN STRUCTURE

All porphyrins consist of a large aromatic macrocycle, the conjugated system of which is similar in features to [18]-annulene[16]. Porphyrins tend to be planar (or nearly so) around this area of aromaticity.

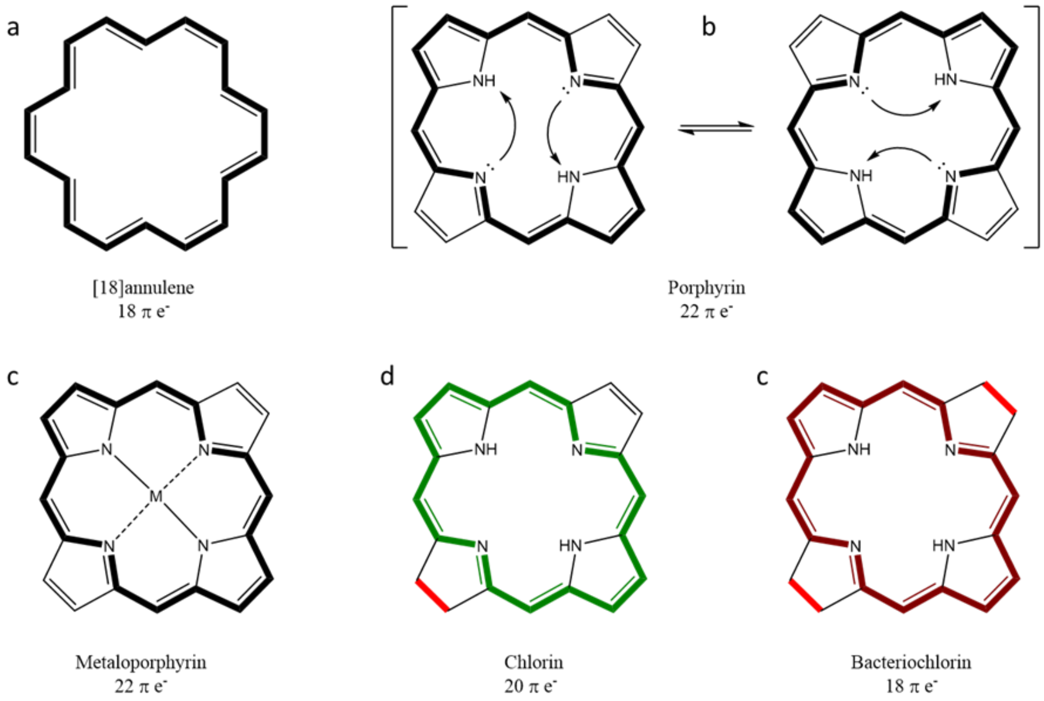

Figure 5. Variation and similarity of aromaticity in porphyrin and porphyrin-like structures.

As can be seen in Figure 5, porphyrins have 22 π electrons. Of these, only 18 electrons are delocalized, in accordance with Huckel's Rule. Because of this, aromaticity can be maintained when up to two of these π-bonds are reduced, as is the case in the closely related derivatives chlorin (Figure 5d) and bacteriochlorin (Figure 5c). Porphyrins also feature several points of substitution (Figure 6) which, because they are peripheral to the core aromatic ring described above, need not interrupt the aromatic nature of the core azoannulene ring.

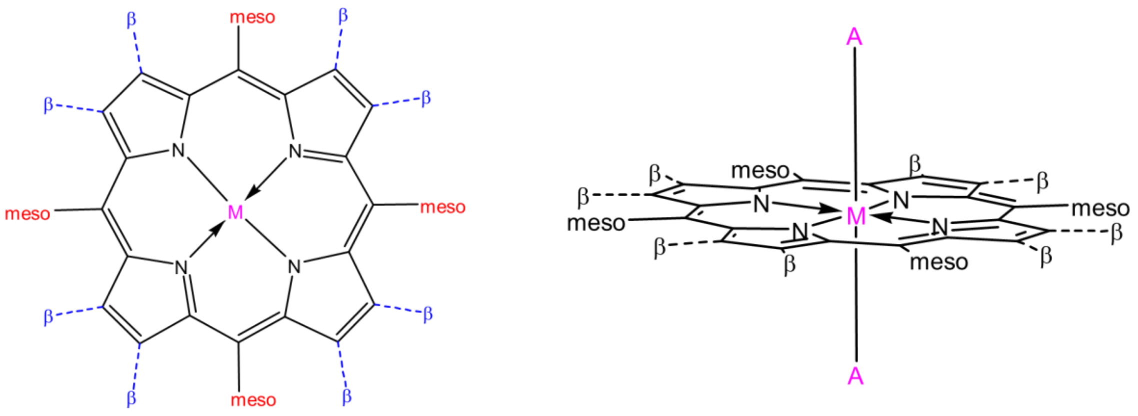

Figure 6. Common points of porphyrin substitution

As seen in Figure 6, porphyrins can be modified at 12 peripheral locations: 8 "β-pyrrole" positions, and 4 "meso" positions. Porphyrins can also host a central metal ion, which displaces the inner 2 hydrogens (compare: Figure 5b and Figure 5c). These metalloporphyrins are then able to be further axially substituted on this central metal. The number and type of axial bonds that can be formed varies depending on the metal involved; in its oxygen-bound state, heme exhibits two covalent bonds (Figure 7a), while phosphorous porphyrins always form two covalent axial bonds (Figure 7b).[17, 18, 19]

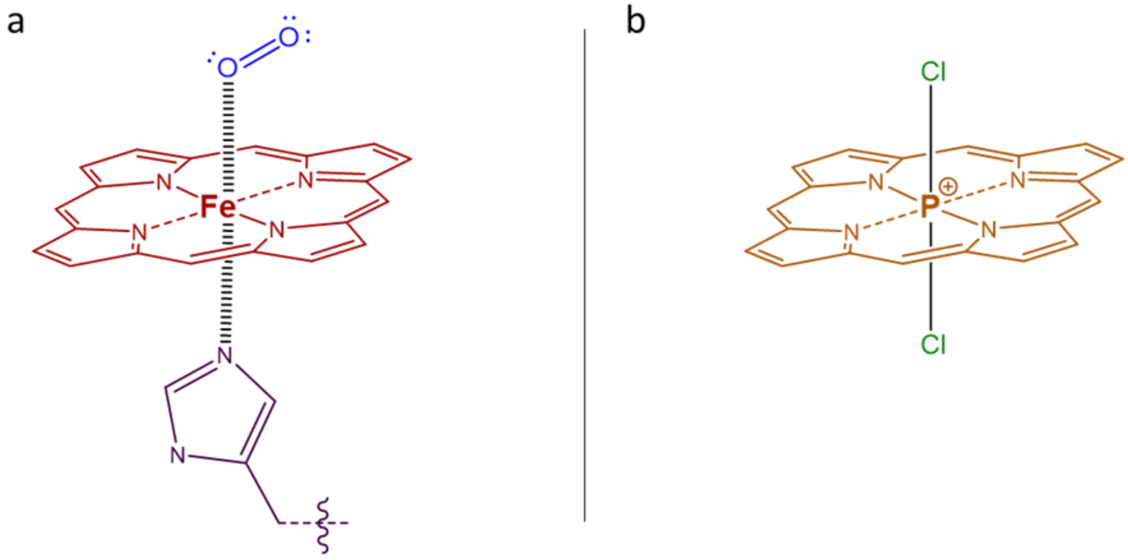

Figure 7. Axial bonding patterns of two metalloporphyrins. a: heme in its oxygen-bound state exhibits two coordinate bonds. b: phosphorous porphyrins form two coordinate bonds. (Note: substitutions at the β and meso positions have been omitted.)

1.6.2 PORPHYRIN SYMMETRY

The dianion tetraphenylporphyrin^{2-} exhibits D_{4h} symmetry (Figure 8). The presence of the central hydrogens on the neutral freebase of tetraphenylporphyrin removes the two σ_d planes in Figure 8d, reducing the symmetry to D_{2h}. The insertion of a metal ion into the porphyrin center displaces these two inner hydrogens, and in the absence of axial substitution, this restores D_{4h} symmetry. In metalloporphyrins with identical axial substituents, such as the dichloro-substituted phosphorous porphyrin shown in Figure 7b, D_{4h} symmetry is maintained. However, if there is only one axial substituent, the σ_h plane is removed, reducing the symmetry to C_{4v}.

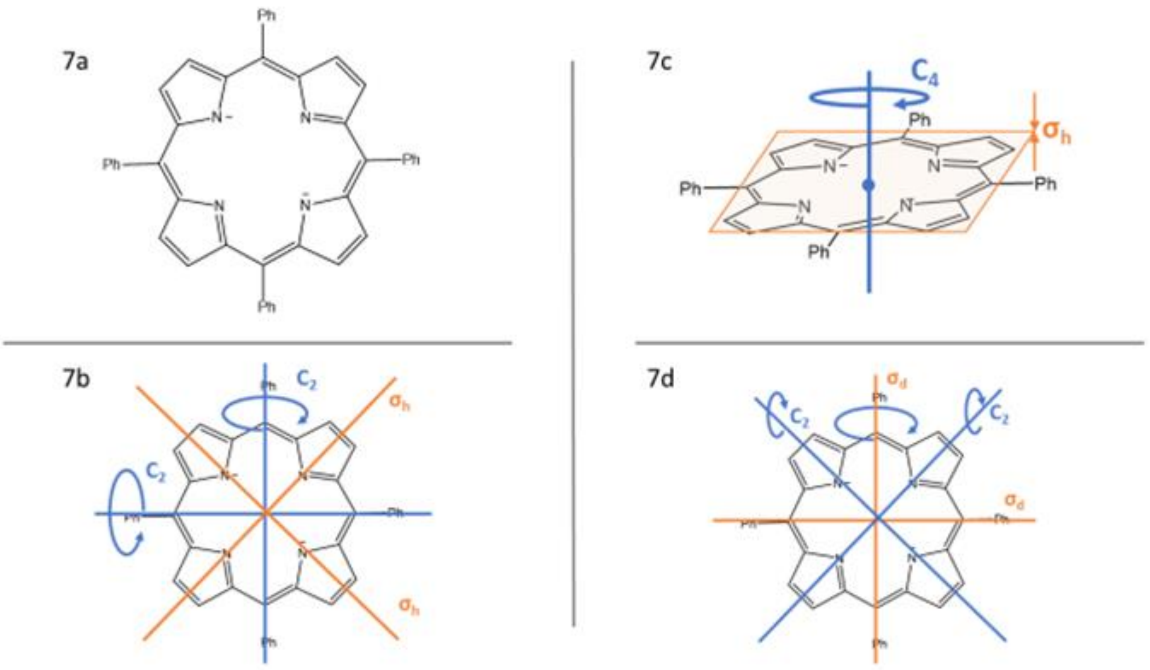

Figure 8. Structure and symmetry operations of the dianion tetraphenylporphyrin^{2-}

1.6.3 SPECTRAL FEATURES OF PORPHYRINS

The strong absorption of porphyrins in the visible-light spectrum arises from π-π* transitions which originate in the extended conjugated azoannulene system described in Section 1.6.1 (Figure 9). These transitions give rise to two major bands in the visible light absorption spectra, one in the near-UV region (~420 nm), and one in the lower-visible region (~560 nm).[20]

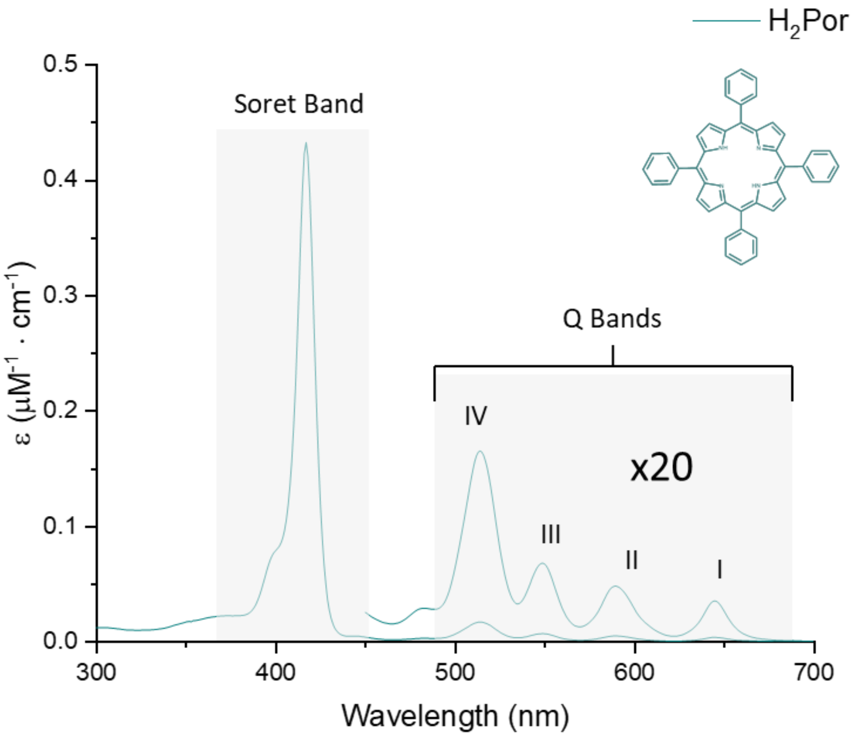

Figure 9. Characteristic features in the UV-vis absorption spectra of porphyrins (shown: freebase tetraphenylporphyrin). The region containing the Q-bands is magnified by a factor of 20. (solvent = acetonitrile).

The mechanics underlying these transitions have been rationalized by an extension of Huckel theory called the "Gouterman 4-orbital model". In brief: the absorption spectra of porphyrins arise from transitions between 2 HOMO, 2 LUMO. Orbital mixing of the excited states produces a higher and a lower energy state. The transition to the S_2 state is strongly allowed, while the transition to the S_1 state is forbidden. This explains why the S_0-S_1 transitions (the Q-band) is much weaker in intensity than those of the S_0-S_2 transition (the B-band, also known as the Soret band).[21, 22, 23]

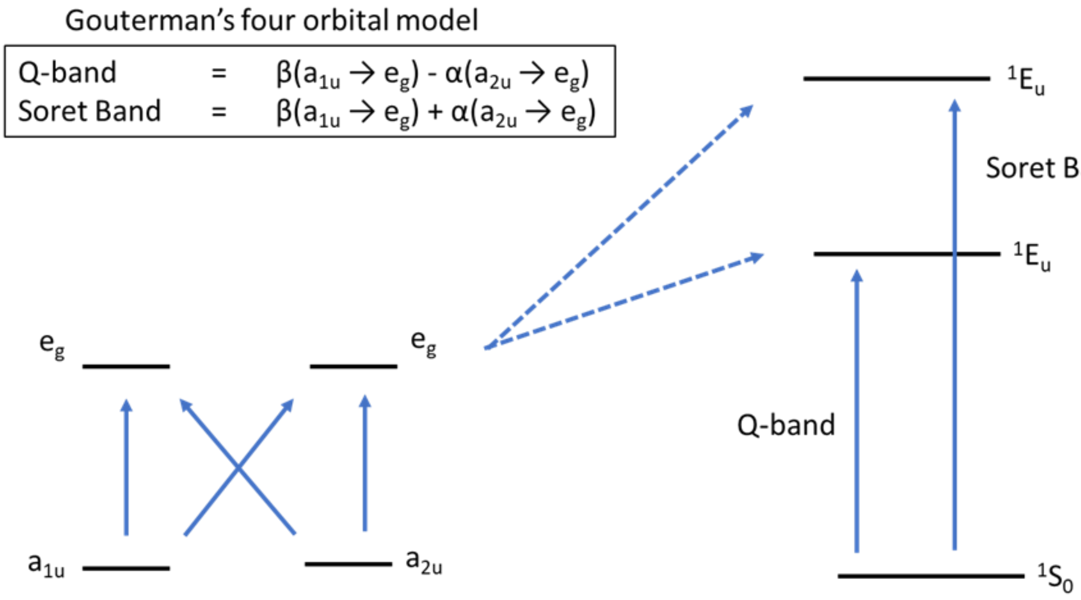

Figure 10. Gouterman's four orbital model relating orbital energy levels to spectral the transitions of a porphyrin system.

Metalloporphyrin symmetry can be perturbed by the presence of axial ligands. The presence of one such ligand tends to pull the metal-center out-of-plane, reducing the symmetry to the C_{4v} point group. This impacts the energetics of the system, and these changes can be seen in the fluorescence spectra (as described in Section 2.2.2). However, the selection rules and band patterns do not change, and the effects of ligation on the energetics of the system can still be adequately described by the "four-orbital" model.[24] The presence of a second countervailing ligand on the opposite side pulls the metal center back in-plane, restoring D_{4h} symmetry (Figure 12).

1.7 ALUMINUM PORPHYRIN-BASED CATALYTIC DYADS AND TRIADS

1.7.1 ALUMINUM(III) PORPHYRINS AS PHOTOSENSITIZERS

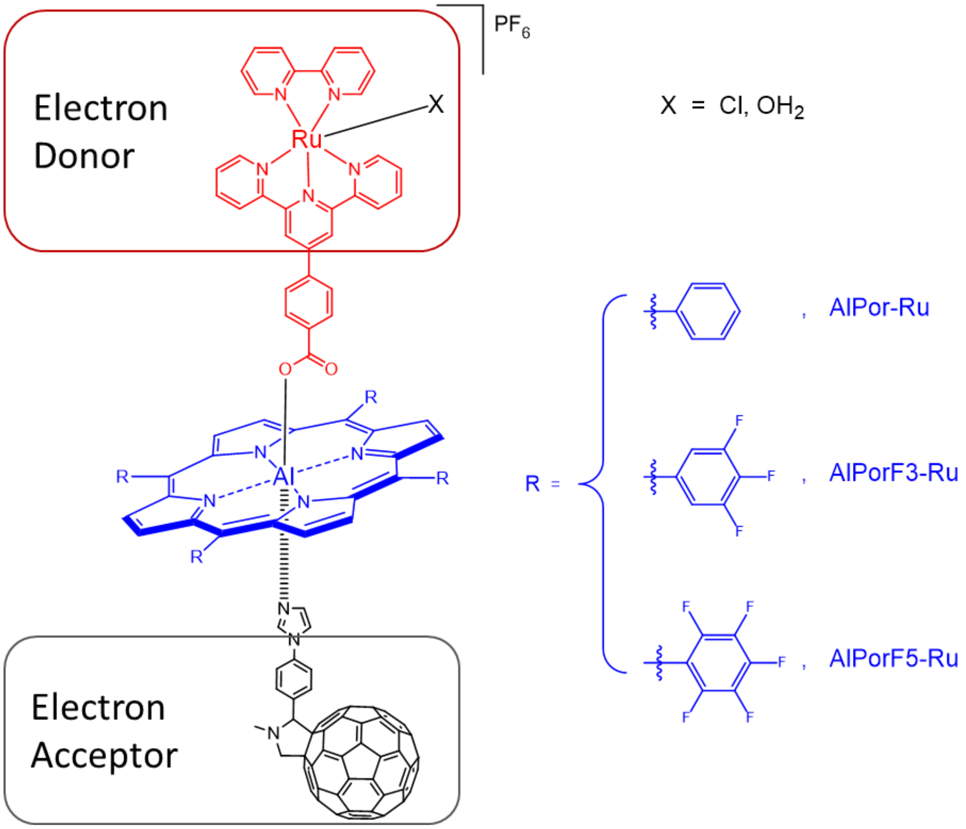

Figure 11. Structure and naming of the three catalytic dyads; the triads are simply the dyads as shown, with the addition of an axially coordinated electron acceptor.

The photoactive catalytic dyads described in this work consist of a series of aluminum(III) porphyrins axially linked (by way of a covalent ester bond to the central aluminum atom) to a ruthenium catalyst (Figure 11). (Full synthetic details for all compounds are given in Chapter 5.)

1.7.2 PROPERTIES SPECIFIC TO ALUMINUM(III) PORPHYRINS

Aluminum(III) porphyrins form exactly one covalent and one coordinate bond.[25, 26, 27] Synthesis of aluminum(III) porphyrins produces a hydroxyl axially situated on the aluminum (Scheme 4), and this readily forms a covalent bond with either an alcohol or carboxylic acid (Figure 12). The coordinate bond forms on the opposite face, with the aluminum acting as a Lewis acid. This allows for specificity in design and assembly of catalytic systems involving these porphyrins.

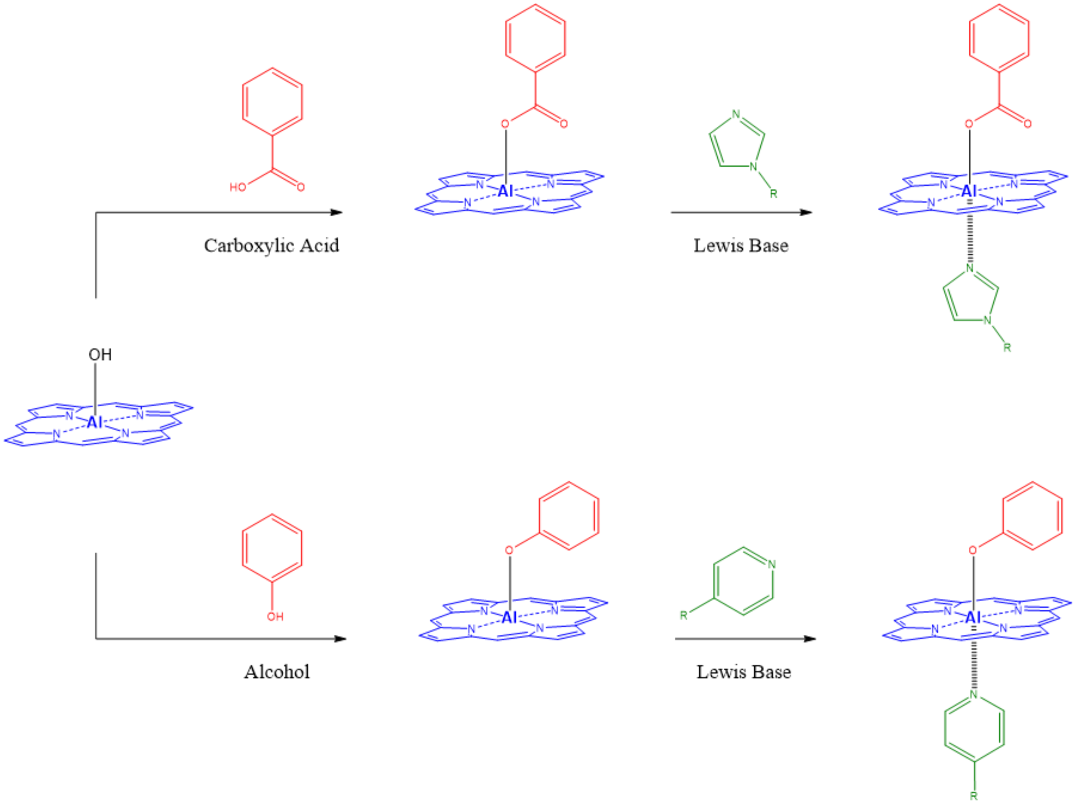

Figure 12. Axial substitution of aluminum porphyrins. Aluminum(III) porphyrins can form exactly one covalent bond with an alcohol or carboxylic acid, and one coordinate bond with a Lewis base. (Note: peripheral substituents have been omitted).

There are several benefits to the axial layout of components seen in Figure 11. One potential problem in the use of porphyrins is that, due to π -π interactions between adjacent molecules, porphyrins have a tendency to aggregate[28]. When the axial positions are occupied, the plane-parallel approach of adjacent porphyrins is sterically inhibited, and such “π -stacking” aggregation is inhibited[27]. Additionally, axial substitution situates the catalytic component perpendicular to the plane of the porphyrin, which in turn decreases orbital overlap between the π-bonds of the porphyrin core and the ruthenium catalyst. The design intent of this is to put the catalyst and porphyrin in close proximity, without disturbing either the catalytic functioning of the catalyst or the light-absorbing function of the porphyrin. In contrast to this, coplanar substitutions have been shown to interfere or greatly change the absorption spectra of porhyrins.[29] Electron and energy transfer mechanics of aluminum(III) porphyrin assemblies with this axially-situated layout of electron donor and acceptor components have been studied.[27]

In the active catalyst, the sixth coordinate position is occupied by a water molecule. This work primarily characterizes the molecules with a chloride in this position. The intent of this is to allow the characterization of the catalyst at intermediate oxidation steps. In the catalytic cycle described in Figure 4, successive oxidations are driven by addition of Ce^{4+}; consequently, the oxidation step of the catalyst can be controlled stoichiometrically. This method of control is not applicable when light provides the driving force for oxidation. The intent of the chloro-derivative is to halt or slow the oxidation of the complex. Characterization of the compounds at sequential oxidative steps (as is described in Chapter 2) reveals the energy and electron transfer behavior of the compounds. Careful analysis of these data lay the groundwork for theoretical modeling of these materials (such as the energy level diagrams described in Section 2.4). This modeling informs the continuing design involved in the eventual implementation of these materials in a functioning photochemical cell (briefly described in Section 3.3). Thus, this current work is a necessary, preparatory step towards the construction of a functional photochemical cell utilizing these materials.

Figure 13 illustrates the electron transfer processes between the electron donor (the catalyst), photosensitizer (the aluminum porphyrins), and electron acceptor.

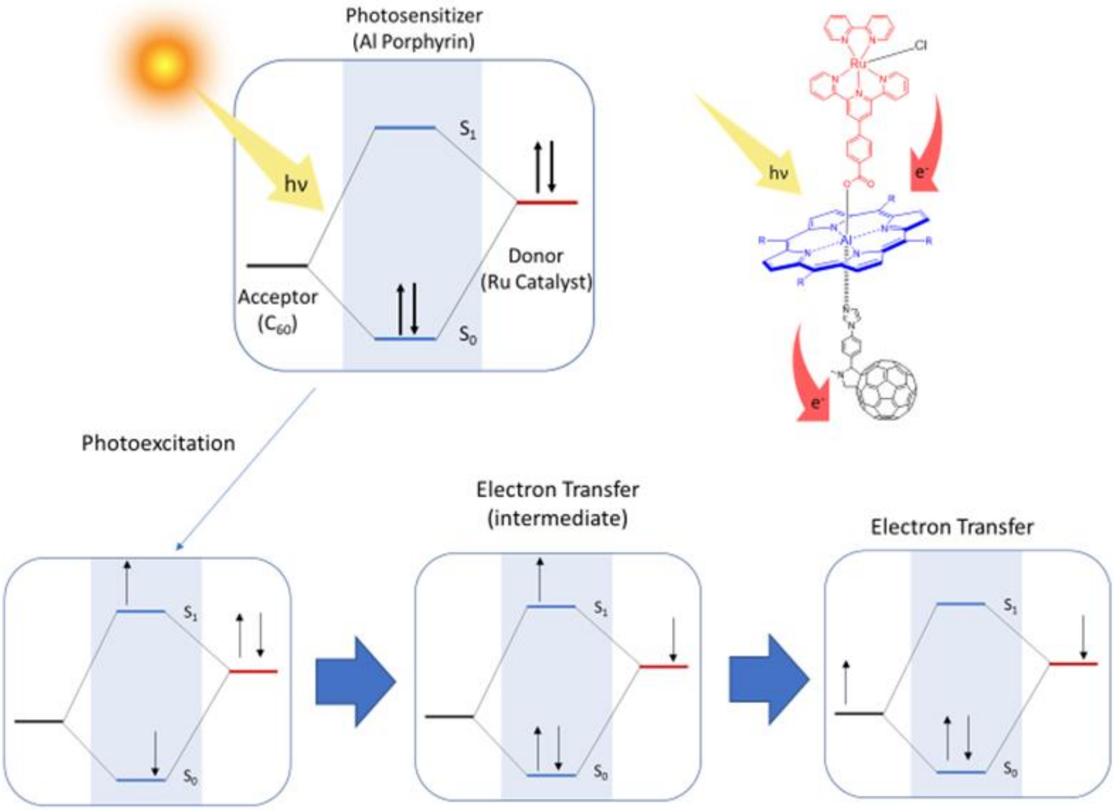

Figure 13. Diagrammatic representation of the desired function of the catalyst/photosensitizer/electron acceptor system.

As can be seen, photoexcitation promotes an electron in the HOMO of the porphyrin, leaving a vacancy. The driving force for oxidation of the catalyst is then provided by the energy gap between the HOMO of the catalyst, and the now half-vacant HOMO of the porphyrin. Similarly, the energy gap between the photoexcited electron and the destination orbital of the electron acceptor (this is either the LUMO of a molecular electron acceptor such as the C_{60} ligand described in this work, or the conduction band of a semiconductor, described further in the conclusion).

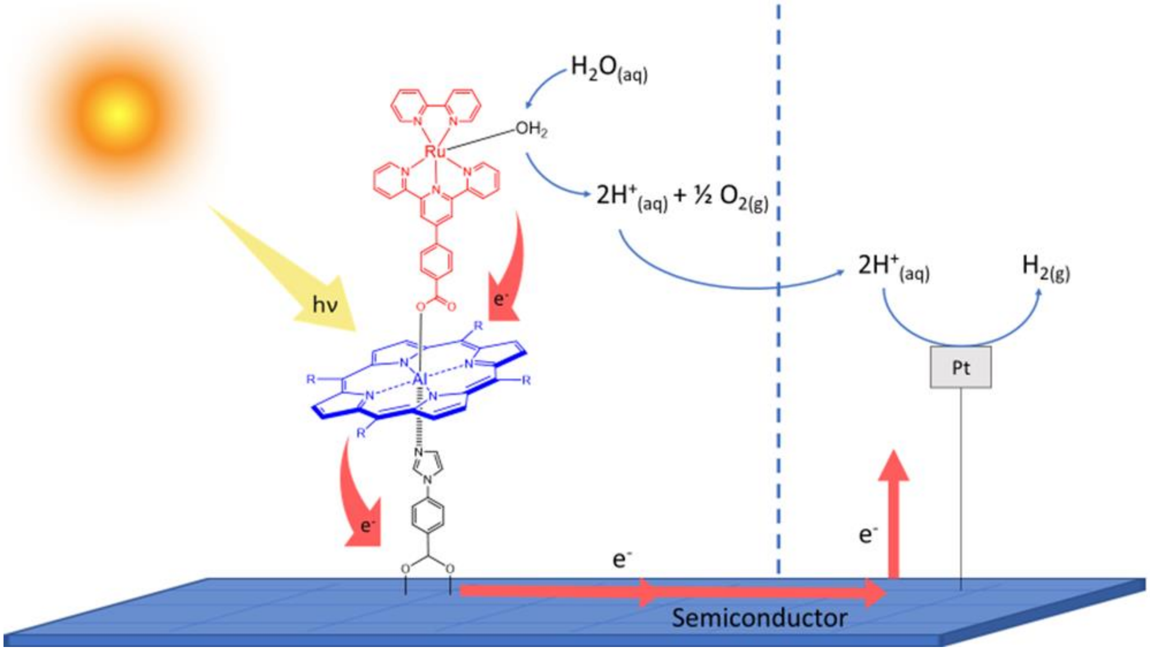

Figure 14. General overview of the compounds described in this work, as they might appear in a photochemical cell.

The three catalytic dyads described in this work differ only in the degree of fluorination on the meso-substituted phenyl groups of the porphyrins. The presence of electron accepting or donating groups on these substituents have been shown to raise or lower the ground state energy of the porphyrin. The design intent is to provide a closely related series of porphyrins, which differ only in the ground state of the photosensitizer. As described above, the ground state of the porphyrin is directly related to the hypothesized mechanisms of the photosensitizer, and therefore, being able to manipulate this variable is one way of probing and validating these proposed mechanisms.

CHAPTER 2: CHARACTERIZATION

2.1 NMR/IDENTIFICATION

The insertion of a metal into the porphyrin core displaces a central pair of hydrogens, and this is easily confirmed by way of proton NMR (Figure 15). Successful formation of the dyad is given by the following characteristic pattern: as the axial phenyl protons approach the aluminum center, they are situated perpendicular to the plane of the porphyrin. As this occurs, it exposes the phenyl protons to the toroidal electromagnetic field generated by the aromatic flow of electrons around the porphyrin. This provides a large amount of shielding, sufficient to push these proton peaks out of the normal aromatic region, and in towards the alkyl-characteristic region (Figure 15).

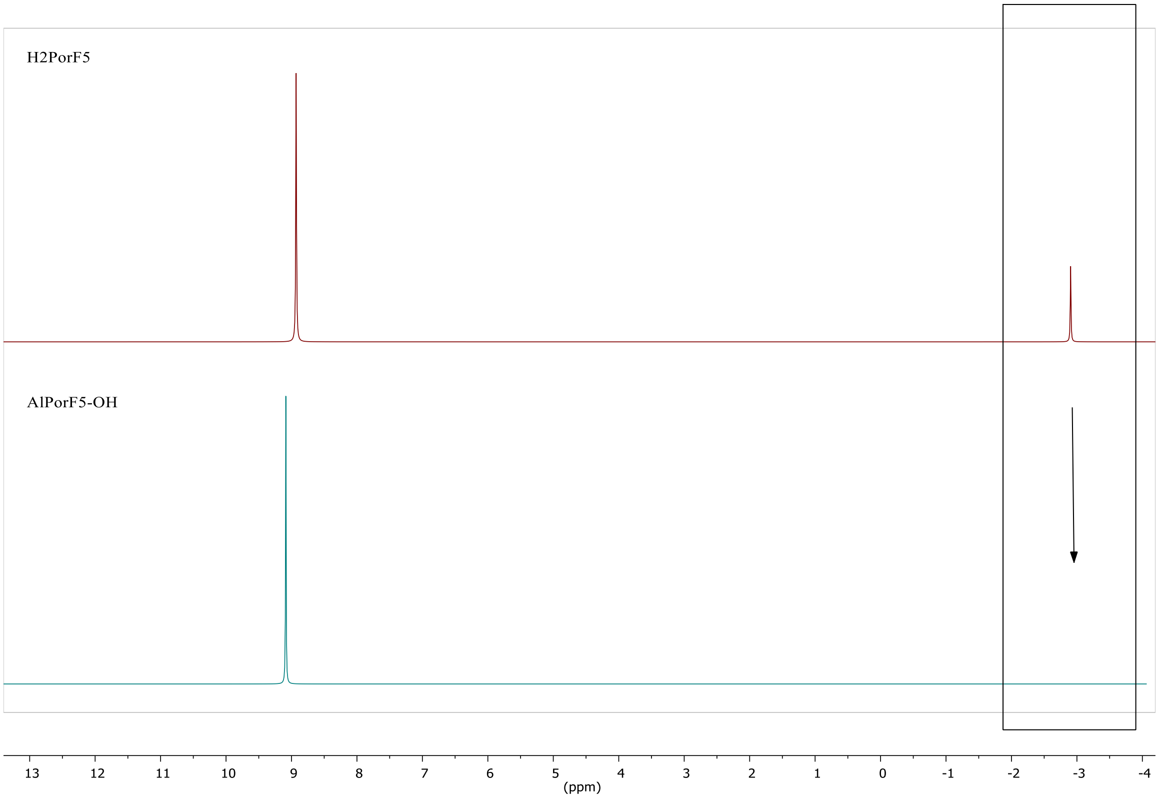

Figure 15. NMR characteristic of metalation. The inserted metal displaces the two hydrogens from the inner ring.

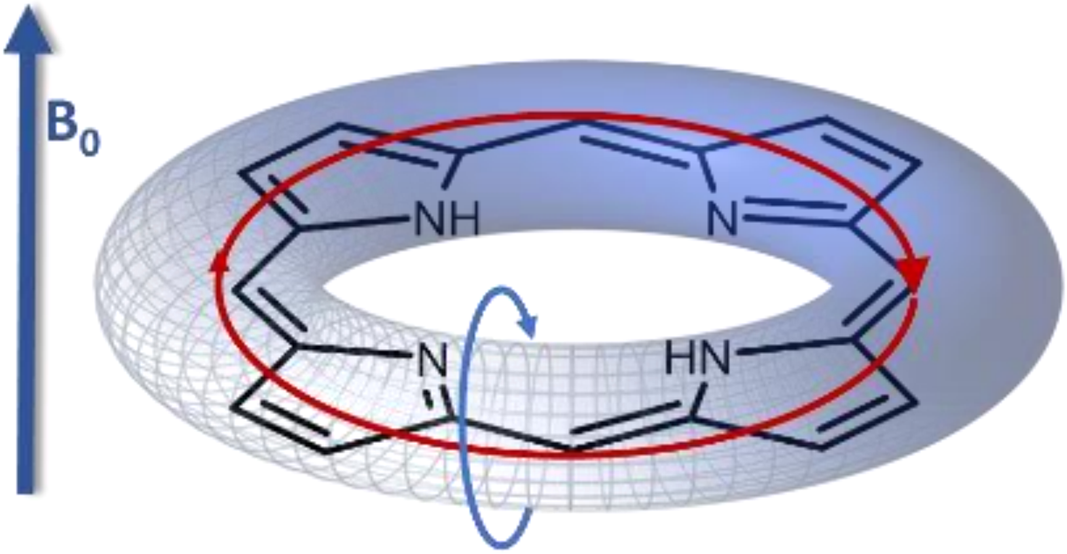

Figure 16. Toroidal magnetic field of a porphyrin. An external magnetic field induces current flow about the azoannulene ring, which in turn produces a toroidal magnetic field.

The circular flow of electrons about the porphyrin core produces a toroidal magnetic field. As an axial ligand approaches this field (as must happen in axial substitution), this toroidal field provides magnetic shielding to proximal protons, and this is readily observable in proton NMR spectra. Thus, successful formation of the porphyrin/catalyst dyads can be confirmed by observing the shifts of the phenyl protons (labeled a and b in Figure 17). This shift is significant, reversing the order of the phenyl-protons, and pushing the most proximal pair of protons out of the normal aromatic region.

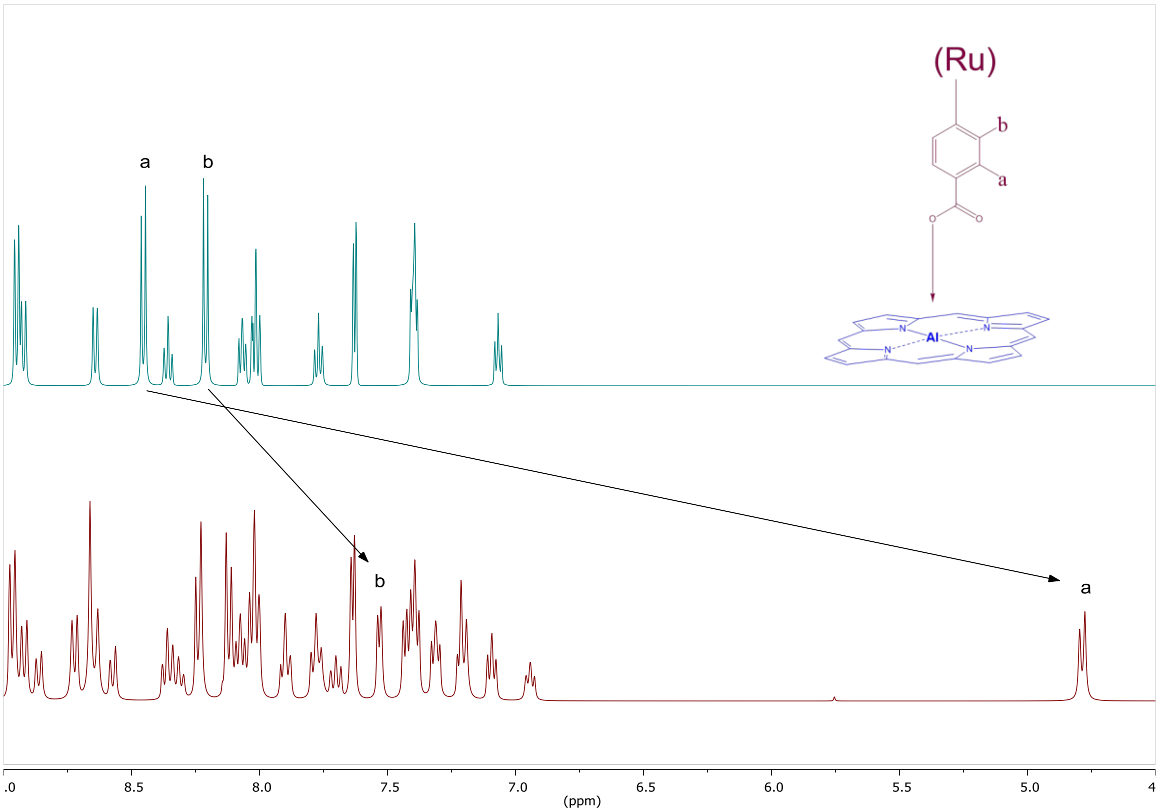

Figure 17. Characteristic shifts of the porphyrin/catalyst dyad formation. The spectrum on top is of the unattached ruthenium catalyst; the spectrum on the bottom is of the catalyst/porphyrin dyad.

2.2 OPTICAL STUDIES

2.2.1 REFERENCE COMPOUNDS: STRUCTURE AND NAMING

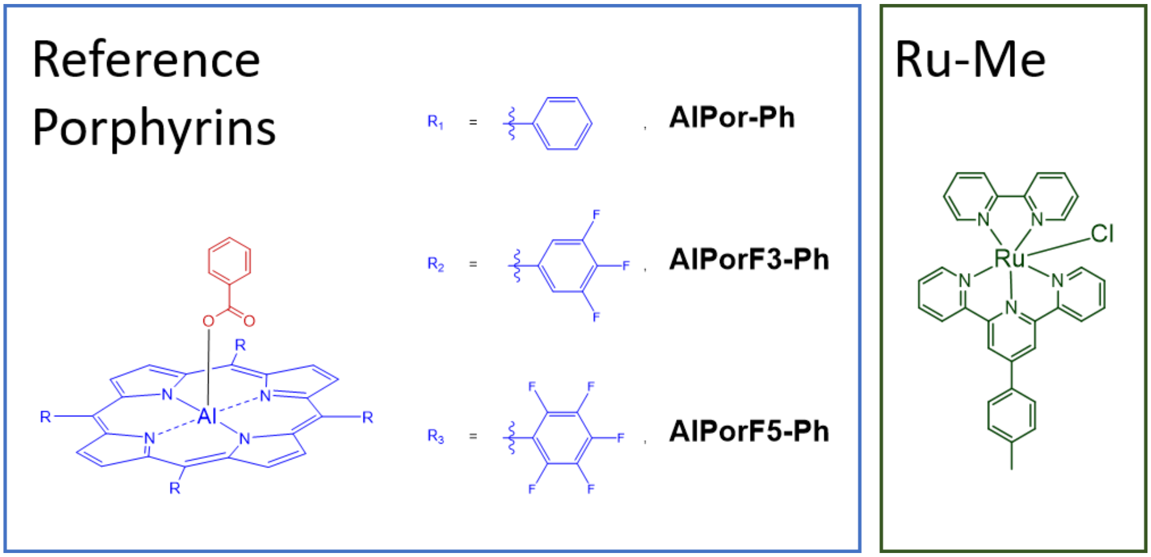

Figure 18. Structure and naming conventions of the reference compounds.

In addition to the dyads shown in Figure 11, several reference compounds were prepared, representing the uncoupled components (Figure 18). The ruthenium reference compound is identical in structure to that used to form the dyad, except that the carboxyl group has been replaced by a methyl group; this prevents unintentional linkages. In the reference compounds, this same effect is achieved by linkage of the axial hydroxyl group of the porphyrin to benzoic acid (further synthetic details are provided in Chapter 5).

2.2.2 UV-VISIBLE ABSORPTION SPECTRA

Aluminum(III) has an electron-donating effect on its constituent porphyrin, and consequently, the absorption spectra become red-shifted relative to that of their respective freebase porphyrins. This effect is most noticeable in the Q-band, where the symmetry changes characteristic of metalloporphyrins can also be seen (Figure 19).

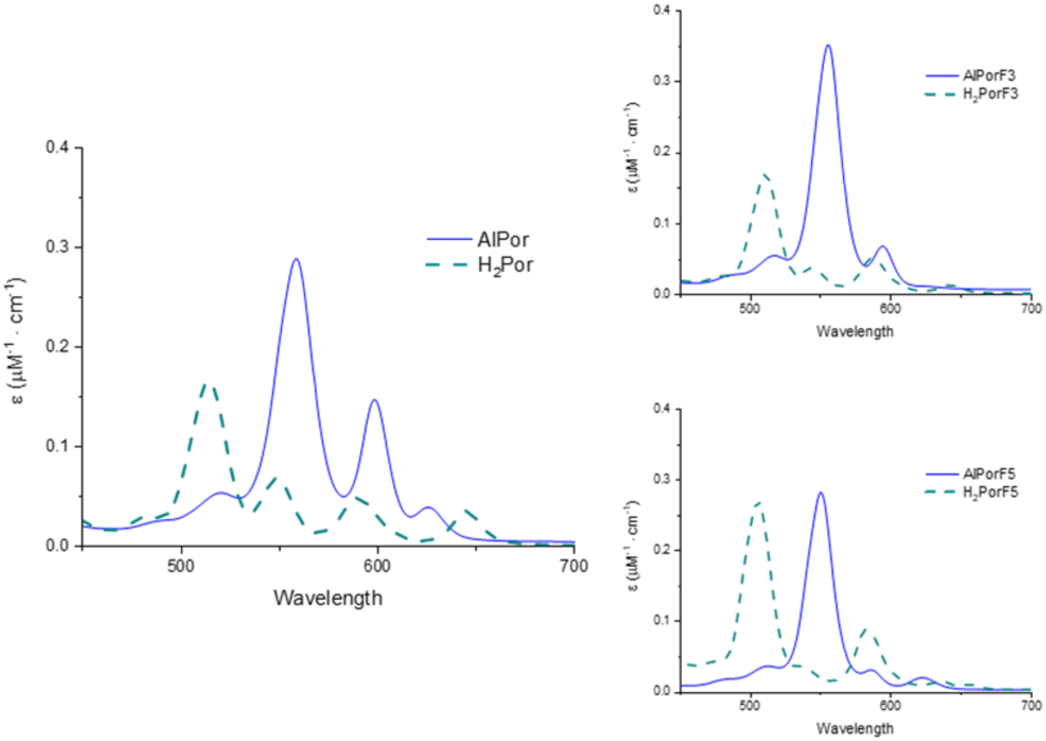

Figure 19. Q-band region of the nonfluorinated, trifluorinated, and pentafluorinated tetraphenylporphyrin derivatives. (Solvent = acetonitrile).

In general, the features of the absorption spectra of the dyads are linear combinations of the spectra of their constituent monomers. That is to say, the peaks seen in each of the reference compounds, are seen in the equivalent dyad. For example, in Figure 20, it can be clearly see that spectra of the dyad (red) preserves the peaks of the ruthenium compound in the UV region (~300 nm), the Soret band of the porphyrin (~420), and in the Q-band region, displays a linear combination of the porphyrin and ruthenium monomers. This implies that the electronic structure and function of these components is largely preserved in the dyad.

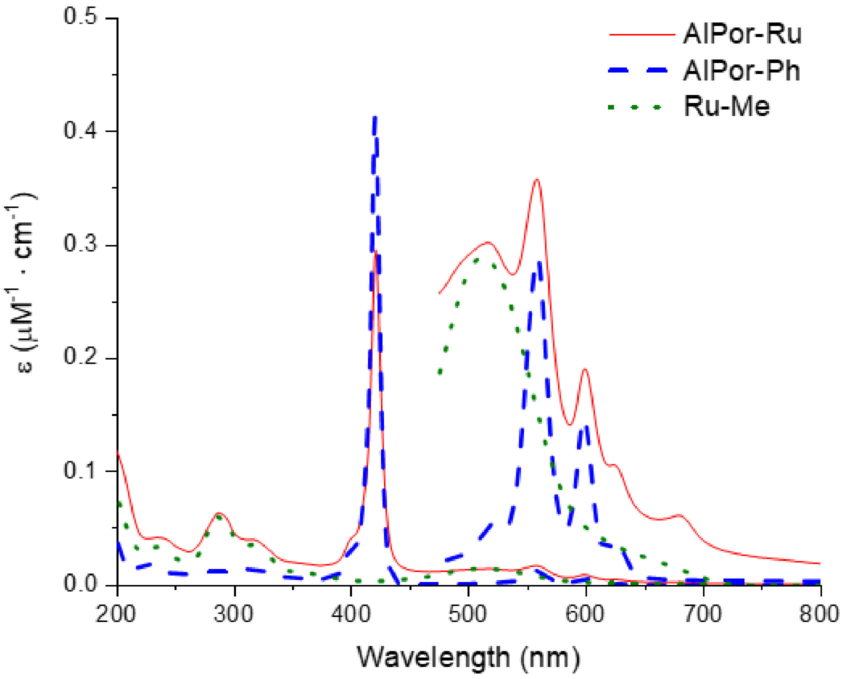

Figure 20. UV-vis spectra of the non-fluorinated reference porphyrin, the related dyad (consisting of the nonfluorinated porphyrin and attached ruthenium complex), and the ruthenium reference molecule. All spectra taken in acetonitrile, and at room temperature.

The peak wavelengths and relative intensities from the absorption spectra are compiled in Table 1; full spectra for all dyads and reference compounds can be found in the appendices.

	λ_{max} ($\log_{10}[\varepsilon]$)
Ru-Me	**236** (4.53), **285** (4.78), **316** (4.55), **511** (4.16)
AlPor-Ph	**315** (4.15), **421** (5.62), **557** (4.10)
AlPor-Ru	**235** (4.62), **287** (4.80), **316** (4.60), **421** (5.47), **517** (4.15), **558** (4.23)
AlPorF3-Ph	**320** (4.23), **419** (5.67), **556** (4.21)
AlPorF3-Ru	**237** (4.75), **287** (4.92), **317** (4.73), **419** (5.57), **514** (4.27), **555** (4.41)
AlPorF5-Ph	**323** (4.15), **415** (5.52), **550** (4.10)
AlPorF5-Ru	**236** (4.42), **287** (4.63), **319** (4.50), **415** (5.41), **512** (3.95), **549** (4.22)

Table 1 Summary of UV-vis absorption data. (Solvent: acetonitrile. Molar absorptivity (ε) in units of $M^{-1} \cdot cm^{-1}$).

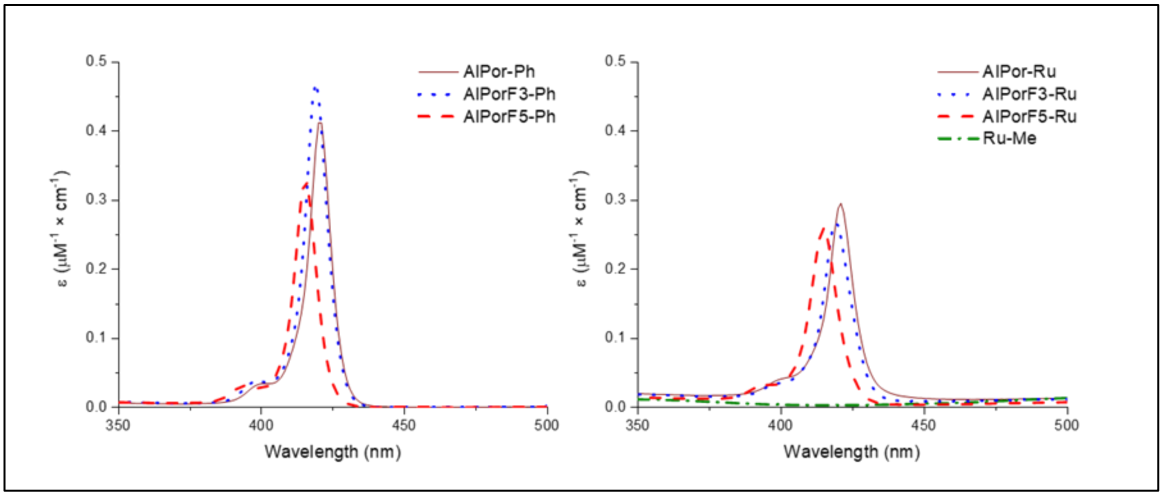

Figure 21. Comparison of the Soret-band region of the UV-vis absorption spectra. Left: spectra of the three reference porphyrins. Right: spectra of the three target compounds (dyads). Spectra taken in acetonitrile and at room temperature.

The Soret-band regions of the three reference porphyrins are compared in Figure 21. As the degree of fluorination increases, the peak wavelength decreases (and therefore energy of transition increases). This trend is consistent for both the reference porphyrin compounds, and the dyads. The intensity of the Soret band is consistently diminished when comparing a monomer to its respective dyad (e.g. AlPor-Ph and AlPor-Ru).

However, when comparing the three reference compounds, there does not appear to be a consistent linear trend in intensity with respect to increased fluorination. As fluorination increases (AlPor-Ph → AlPorF$_3$-Ph), the intensity first increases, and then (AlporF3-Ph → AlPorF5-Ph) decreases to below that of the nonfluorinated porphyrin. The peak intensities seen in the dyads do show a linear trend, with a decrease in Soret band intensity accompanying increased fluorination.

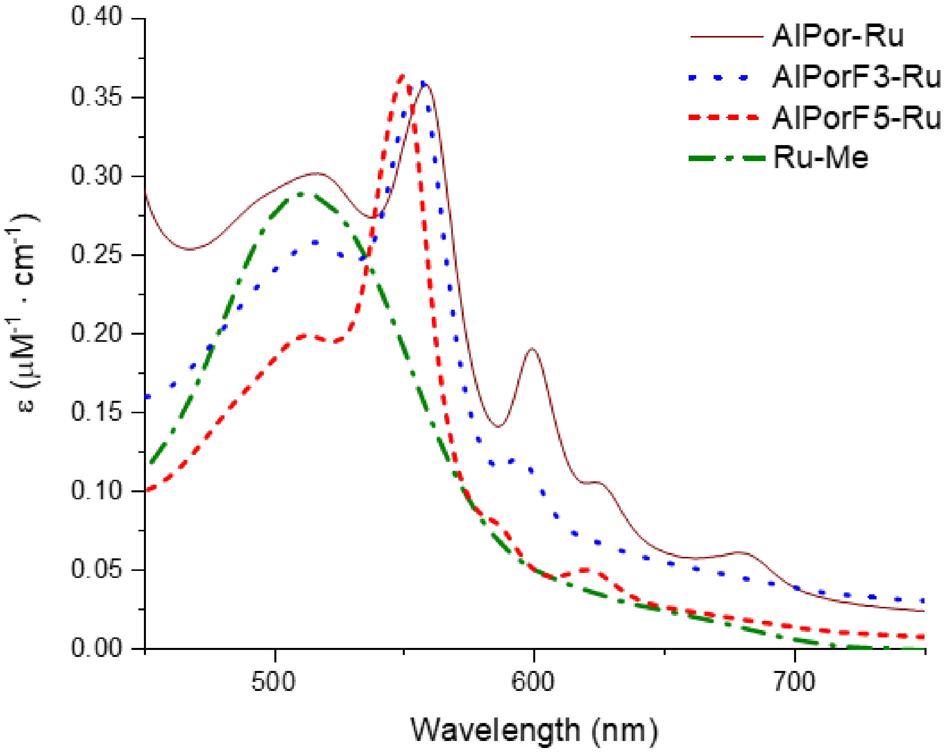

Figure 22. Comparisons between the ruthenium-containing compounds in specific segments of the UV-vis absorption spectra. All spectra taken in acetonitrile and at room temperature.

The Q-band regions of the three porphyrin/catalyst dyads are compared in Figure 22. The non-fluorinated porphyrin shows, as would be expected, an absorption peak that is a linear combination of that of the porphyrin and ruthenium reference compounds; consequently, the AlPor-Ru peak is higher than that of Ru-Me. As the degree of fluorination increases, the ability of the ruthenium component to absorb in this region appears to decrease; both AlPorF3-Ru and AlPorF5-Ru absorb less-strongly than that of the free ruthenium monomer. This is clearly seen in Figure 22, as the peaks for AlPorF3-Ru and AlPorF5-Ru are lower in intensity than that of the ruthenium compound alone.

2.2.3 FLUORESCENCE SPECTRA

As would be true for any fluorescence assay, the molecule of interest must be able to absorb strongly at the excitation wavelength chosen. For porphyrins, there are two main absorption bands which suggest themselves. These are the Soret band, in the near-UV region, and the Q-bands in the visible-light region of the spectrum. Excitation any further up the into the UV region would be too energetic, degrading the molecules involved; conversely, photons from the infrared region are not energetic enough to drive the processes of interest.

However, it is also important to consider the specific behavior that is being probed. The molecular systems being examined were designed such that the porphyrin serves as the driving force for an attached catalyst. When characterizing this behavior, it is therefore desirable to choose a wavelength which excites the porphyrin, but not the ruthenium complex. The UV-Vis absorption spectra of Ru-Me shows a broad, low band across the visible region, peaking at 490 nm. The intensity of this band is on the order of magnitude of the Q-bands of the reference porphyrins.

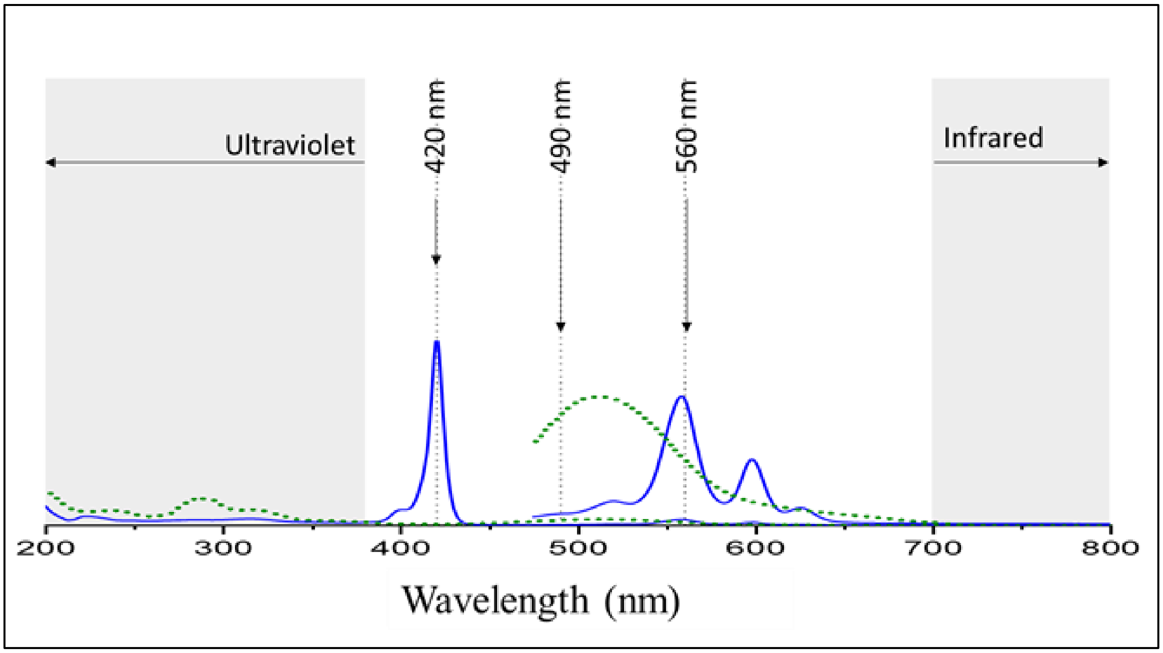

Figure 23. UV-vis absorption spectra of AlPor-Ph, highlighting the wavelengths considered for use as excitation wavelengths in fluorescence studies in acetonitrile. Solid line: AlPor-Ph. Dotted line: Ru-Me. The Q-band region is magnified by a factor of 20. (Solvent = acetonitrilie).

Fluorescence spectra were collected using all three wavelengths shown in Figure 23. Excitation of the porphyrin is represented by excitation at the Soret band (420 nm) and the Q-bands (560 nm). In order to examine the effects (if any) of exciting the ruthenium complex, fluorescence spectra were also gathered from the 490 nm excitation wavelength. As can be seen in Figure 24 (right), the ruthenium compound alone does not fluoresce at any of the wavelengths tested. As seen in Figure 24 (left), the reference porphyrins can fluoresce at this wavelength, though it is significantly less than that of the other two wavelengths.

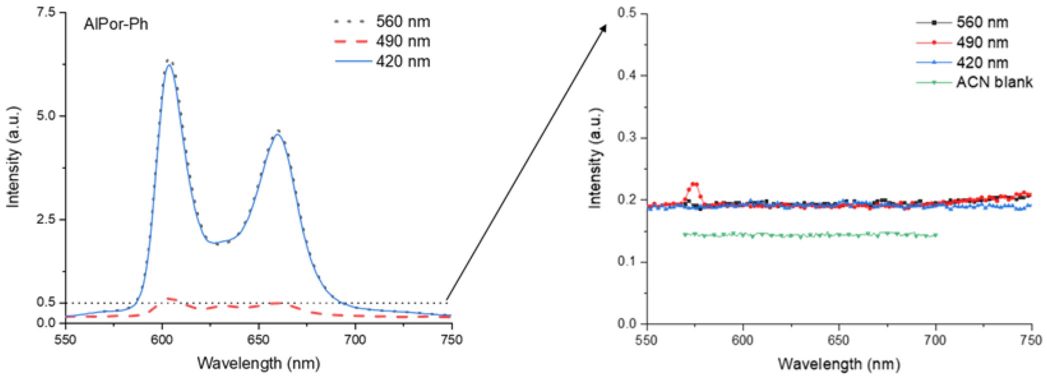

Figure 24. Left: Comparison of fluorescence spectra of AlPor-Ph at different excitation wavelengths. Right: fluorescence spectra of Ru-Me at different excitation wavelengths. All spectra taken in acetonitrile.

The effects of coordination by a Lewis base were examined by comparing the fluorescence spectra of several coordinating and non-coordinating solvents. Figure 25 directly compares the fluorescence spectra of the reference porphyrins in acetonitrile (a coordinating solvent) to that of the reference porphyrins in toluene (a non-coordinating solvent).

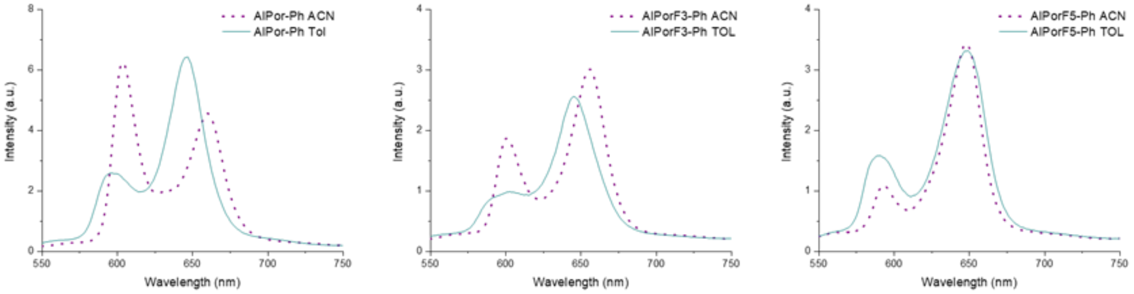

Figure 25. Effects of a coordinating solvent (acetonitrile) vs. a non-coordination solvent (toluene) on fluorescence spectra of the reference porphyrin compounds. Excitation wavelength: 420 nm.

The effect is strongest in the spectrum of AlPor-Ph and diminishes as the degree of fluorination increases. The cause of this is not immediately apparent.

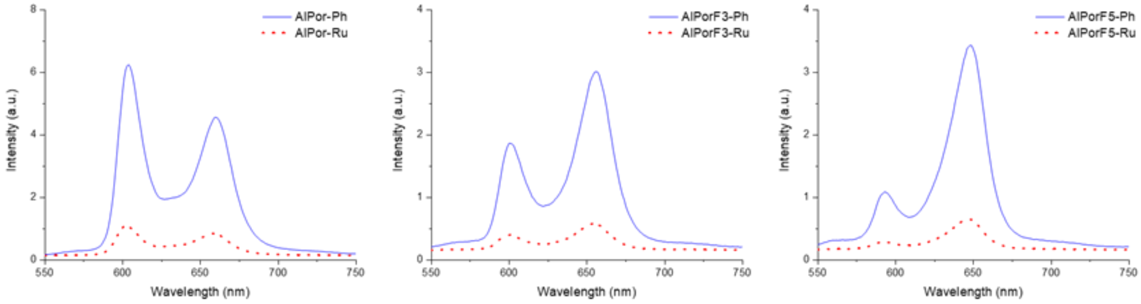

Figure 26. . Fluorescence spectra of the dyads compared against their relevant reference porphyrins. (Excitation = 420 nm. Solvent = acetonitrile. All spectra taken at room temperature. All concentrations standardized to 5 x 10^{-5} M)

Figure 26 compares the fluorescence of each dyad to its relevant reference porphyrin; qualitatively, significant quenching is apparent for all three dyads. Numerical values for this fluorescence quenching were calculated (Table 2). These values were calculated in the following manner: first, absolute values of fluorescence for each molecule were determined by integrating the area under the curve between 570 and 750 nm. The values of the porphyrin-ruthenium dyads (RU) and the reference porphyrins (PH) were then compared using the following equation:

$$quenching\ \% = \frac{PH - RU}{PH} * 100\% \qquad (7)$$

When electron transfer occurs across a molecule, the result is a radical-ion pair. Polar solvent molecules can serve to buffer these charges, stabilizing the molecule. In contrast to this, energy transfer across a molecule does not create such ionization, and no such charges are produced. Therefore, if there is a clear relationship between solvent polarity and degree of quenching, the quenching mechanism can be indirectly inferred. Relative to toluene, more quenching is seen in acetonitrile, but less is seen in THF. Therefore, based on these data, no reliable polarity/quenching trend is seen, and no conclusion is supported.

λ_{ex} = 420	ACN	THF	TOL
AlPor	77.83%	48.02%	61.45%
AlPorF3	71.68%	29.28%	57.99%
AlPorF5	70.65%	71.15%	62.24%
Avg.	73.38%	49.48%	60.56%

λ_{ex} = 560	ACN	THF	TOL
AlPor	79.37%	67.09%	77.21%
AlPorF3	83.18%	58.93%	67.59%
AlPorF5	70.57%	71.33%	66.18%
Avg.	77.71%	65.78%	70.33%

Table 2. Fluorescence quenching. Values calculated using equation 1, with spectral integrations between 570 and 750 nm.

Electron and energy transfer are both intramolecular events which can result in fluorescence quenching. The contribution of intermolecular quenching can be examined by comparing a mixture of porphyrin and ruthenium-complex monads to that of the related dyad. As seen in Figure 27, no quenching is seen in such a mixture of reference compounds. This is at least a prima facie indication that the source of the quenching is intramolecular in nature. However, under the concentrations tested, the ruthenium and porphyrin components would be much further apart than they would be in the assembled dyads. Since there are quenching mechanisms (such as Forster resonance energy transfer) which are extremely distance sensitive, this cannot be seen as a definitive proof.[30]

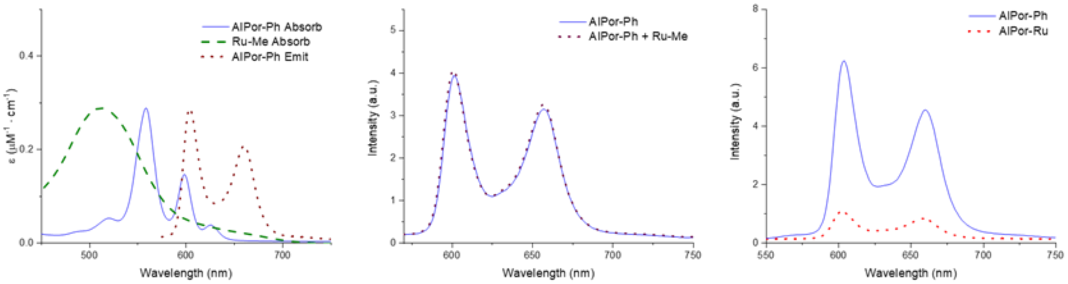

Figure 27. Comparison of fluorescence spectra for a mixture of monomers (middle), and the related dyads (right). All concentrations were standardized to 5 x 10^{-5} M, with the concentrations of the mixed materials being 5 x 10^{-5} M in each of the reference compounds (as opposed to 5 x 10^{-5} M combined). (Excitation = 560 nm, solvent = acetonitrile, spectra taken at room temperature). The overlap of the absorbance and fluorescence spectra of the relevant reference compounds is shown on the left. (solvent = acetonitrile)

2.3 ELECTROCHEMISTRY

The redox potentials of the dyads and reference compounds were assayed through cyclic and differential pulse voltammetry. The important features and trends are summarized in Figure 28 and Figure 29, and values for the redox potentials are summarized in Table 3. The full voltammograms for all compounds are compiled in the appendices.

The electrochemical data reveals two important trends; as seen in Figure 28, the voltammograms of the dyads are linear combinations of the voltammograms of the relevant reference compounds. Figure 29 shows that, as the degree of fluorination increases, the magnitude of the oxidation also increases. In all cases, the oxidation of the ruthenium complex occurs before that of the first oxidation of the porphyrins.

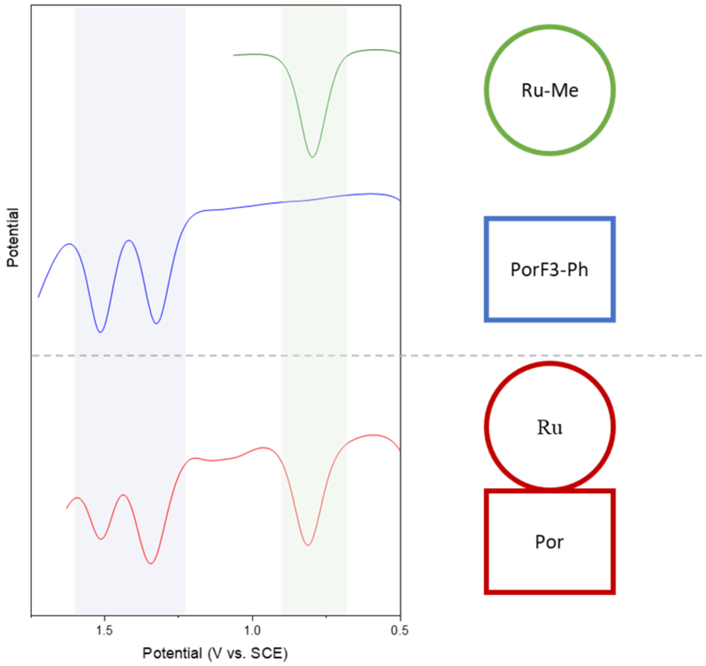

Figure 28. Comparison of the oxidative DPV of AlPorF5-Ru to that of the relevant reference compounds. (solvent = acetonitril, 0.1 M TBAPF6, Fc used as an internal standard).

For the most part, these same trends are seen in the reduction: the magnitude of the nonfluorinated porphyrin is smaller than that of the fluorinated porphyrins. In contrast to the oxidations, the porphyrin reductions show more variability across the F0 → F5 series. The porphyrin oxidations show two clear, consistently spaced peaks, whereas the reduction peaks vary in both number and spacing. The nonfluorinated porphyrin shows three clear peaks, the trifluorinated porphyrin shows two broad peaks, and pentafluorinated porphyrin shows one-clear and one-compound peak. Additionally, the magnitude of the trifluorinated porphyrin is very close to that of the pentafluorinated porphyrin. Despite this variability, it remains clear that the first porphyrin reductions are always of smaller magnitude than that of the first ruthenium-complex reductions.

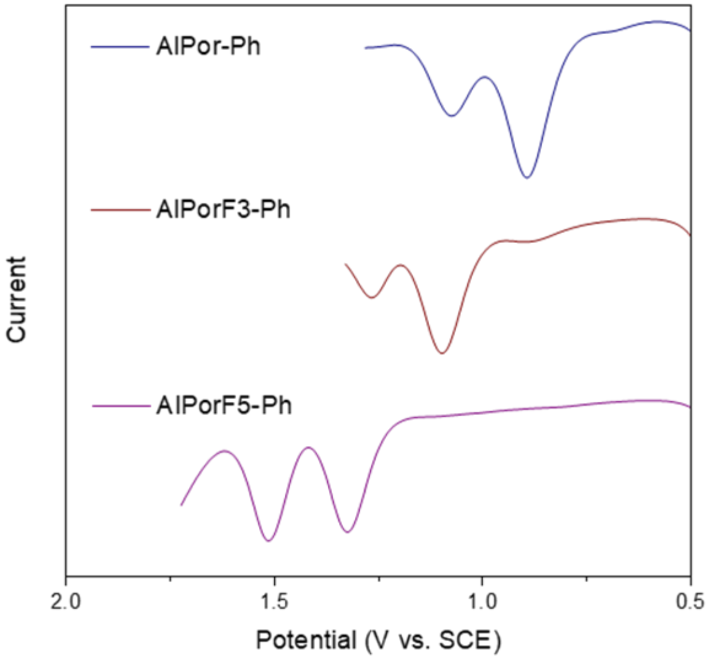

Figure 29. Differential pulse voltammograms of the three reference porphyrins. Solvent: 0.1 M TBAPF6 in ACN with Fc as an internal standard.

Both the absolute and relative (porphyrin vs. ruthenium complex) redox values are important in determining whether these molecules can function as designed. The desired behavior of the system involves simultaneous oxidation of the ruthenium complex and reduction of the porphyrin. The ordering of the magnitude of the redox values show that it is clearly energetically favorable for this to happen. Additionally, the magnitude of the energy gap between first-oxidation and first-reduction is indicative of the driving force available to effect electron transfer.

The cyclic voltammograms (CV) produced results in close agreement with that of the differential pulse voltammograms (DPV). As seen in **Error! Reference source not found.**, most of the peaks appear to be reversible. However, the CVs of the F3 and F5 porphyrins show nonreversible oxidation peaks. The CV of AlPor-Ph appears to have two nonreversible peaks; however, in the CV of the related dyad AlPorF5-Ru, the peak near +1.3 appears to be reversible. These nonreversible peaks and inconsistencies are minimal or absent in the DPVs. Therefore, in the name of consistency, all values displayed in tables and used in the calculations of energy levels were taken from the DPVs. The CVs remain useful in verifying that all of the peaks seen in the DPs are reversible in nature (they are). All CVs are provided in the appendices.

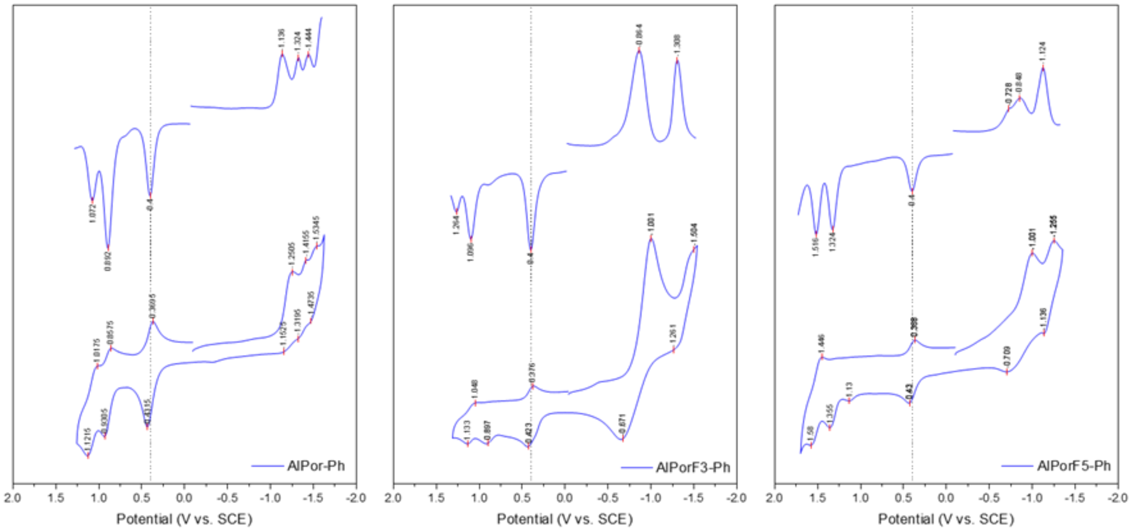

Figure 30. Comparison of CPV and DPV for the reference porphyrins. Ferrocene used as an internal standard. Solvent = acetonitrile; supporting electrolyte = TBAPF6.

2.4 ENERGY LEVEL DIAGRAMS

The optical and electrochemical data were used to calculate the transition energies shown in Table 3. The ΔE of the $S_0 \rightarrow S_1$ transitions were determined by finding the point of overlap between the Q-band absorption and fluorescence spectra; these values represent the 0-0 vibrational transitions. All absorb-fluorescence crossover spectra are given in the appendices. The redox values in Table 3 are simply the values given by the DPV.

	$S_0 \rightarrow S_1$	Oxidation (+)			Reduction (-)				
Ru-Me		0.80					-1.36		-1.52
AlPor-Ph	2.08		0.89	1.07	-1.14	-1.32	-1.44		
AlPor-Ru	2.09	0.82	1.07		-1.12	-1.37	-1.50	-1.64	
AlPorF3-Ph	2.14		1.10	1.26	-0.86	-1.31			
AlPorF3-Ru	2.15	0.81	1.10	1.26	-0.80	1.31	-1.38	-1.48	-1.72
AlPorF5-Ph	2.14		1.32	1.52	-0.73	-0.85	-1.12		
AlPorF5-Ru	2.13	0.81	1.34	1.51	-0.68	-0.82	-1.11	-1.36	-1.48

Table 3. Summary of redox potentials and excitation energies. All values are stated in electron volts. All redox values are taken from the direct pulse voltammograms, with potentials cited in terms of volts vs. SCE.

The energy values found in Table 3 were used to construct the energy level diagrams shown in (Figure 31). The energy levels of the radical ion pairs represent the energy difference between the first oxidation of the ruthenium complex, and the first reduction of the relevant aluminum porphyrin; these values were taken from the electrochemical data of the reference molecules.

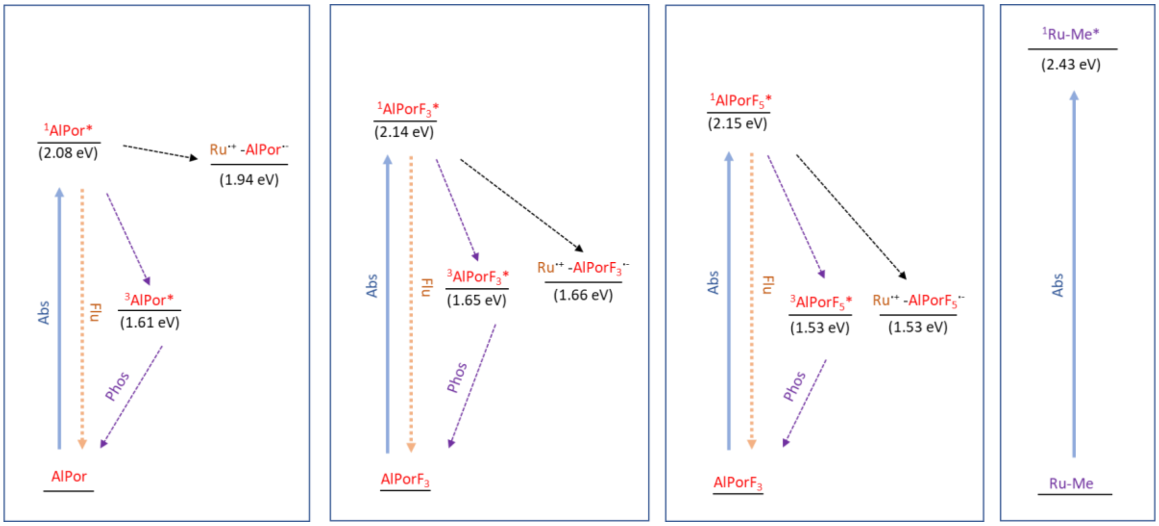

Figure 31. Energy level diagrams of the three porphyrin/ruthenium dyads.

The next step in the catalytic cycle is for the electron on the porphyrin radical to be transferred to a suitable electron acceptor. This resets the porphyrin to its ground state, allowing for the next turnover of the cycle to happen (as described in the introduction, multiple such cycles are required to effect the eventual oxidation of water, as ruthenium is pumped into the +5 oxidation state). In the eventual photochemical cell, this electron acceptor will be the conduction band of a semiconductor, but in the immediate term this behavior can be modeled by a fullerene ligand. The electronic interaction of the dyads with the electron acceptor occurs across a coordinate bond between the aluminum center and a suitable Lewis base. Optical monitoring of titrations between the dyads and fullerene ligands can show that this interaction occurs, and the calculation of binding coefficients from this data give indications of how strong (and therefore stable) these bonds are.

Titrations were conducted for the first of the three dyads (AlPor-Ru). The titrations were conducted in o-dichlorobenzene, a polar non-coordinating solvent. The absorption and fluorescence spectra for these titrations are shown in Figure 32 and Figure 33. In both cases, the ligands were added in 20 μL increments to a 1 mL volume of dimer (5×10^{-6} M), up to a total concentration of 3.05×10^{-5} M. The excitation wavelength for the fluorescence spectra (λ_{ex} = 557 nm) was derived by finding the isosbestic point in the C_{60}-Im UV-Vis titration.

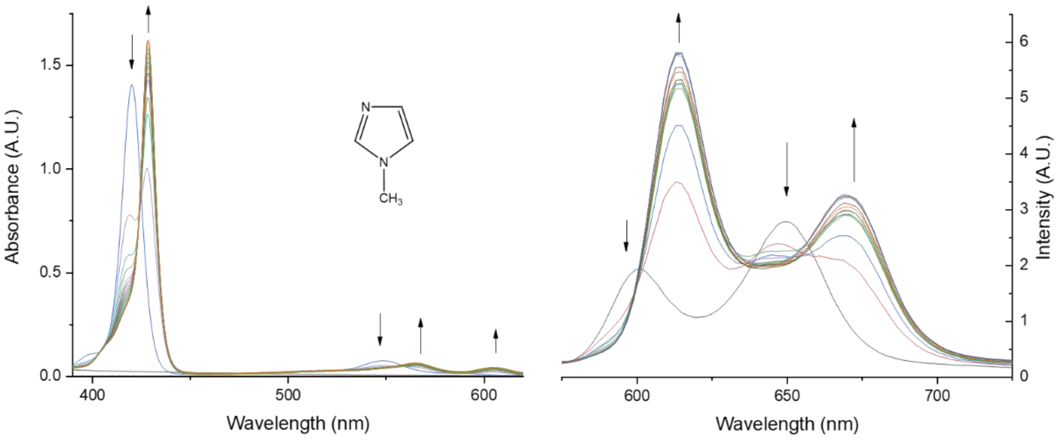

Figure 32. Absorption (left) and fluorescence (right) titrations of AlPor-Ru vs. methylimidazole in o-dichlorobenzene.

Figure 32 shows the absorption and fluorescence of the AlPor-Ru dyad with methylimidazole. Qualitatively, the fluorescence spectra shows a shift in peaks characteristic of coordination on the aluminum center of the porphyrin (as illustrated by Figure 25).

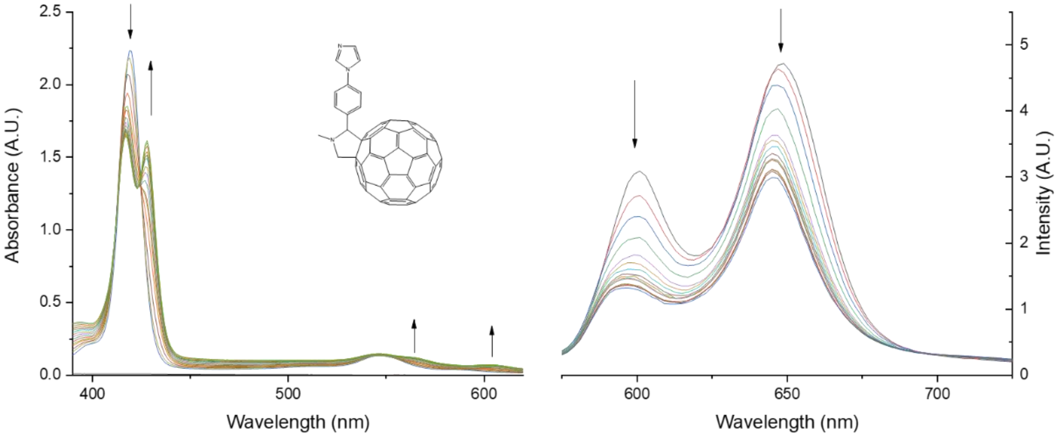

Figure 33. Absorption (left) and fluorescence (right) titrations of AlPor-Ru vs. C_{60}-Im in o-dichlorobenzene.

In examining Figure 33, it important to note that the C60-Im ligand absorbs significantly across the UV-Vis spectra. This essentially causes the baseline to float upward as increasing amounts of ligand are added. As can be seen by the associated fluorescence spectra, the triad (AlPor-Ru←C$_{60}$-Im) does not appear to be fluorescent. This complete loss of fluorescence is characteristic of electron transfer. Therefore, the population of bound/unbound dyads can be inferred by the decrease in fluorescent intensity.

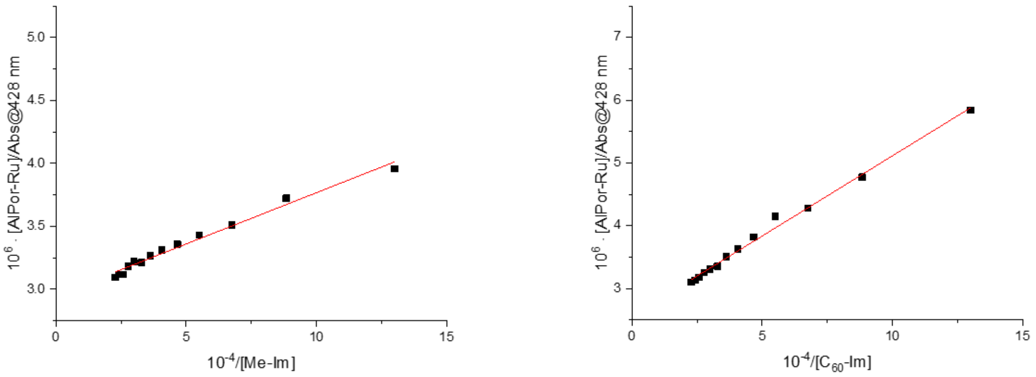

Figure 34. Benesi-Hildebrand plots for Me-Im and C$_{60}$-Im titrations. Values derived from the UV-Vis absorption spectra found in Figure 32 and Figure 33.

Benesi-Hildebrand analysis of the titration data yielded linear plots for both ligands (Figure 34), indicating a 1:1 ratio of complex formation. Linear regression also allowed for the derivation of binding constants, in accordance with the following equation:

$$\frac{[AlPor-Ru]}{Abs_{428\,nm}} = \frac{1}{[Ligand]}\frac{1}{\epsilon K} + \frac{1}{\epsilon} \qquad (8)$$

Binding constants were calculated to be $1 \cdot 10^4\ M^{-1}$ for AlPor-Ru←C$_{60}$-Im, and $3.6 \cdot 10^4\ M^{-1}$ for AlPor-Ru←Me-Im.

CHAPTER 3: CONCLUSIONS AND FUTURE WORK

3.1 DISCUSSION OF RESULTS

The characterization results discussed above reveal these aluminum porphyrins to be promising candidates for the activation of water oxidation catalysts. Qualitatively, the absorption spectra suggest that the electronic structure of both the aluminum porphyrins and ruthenium complexes are preserved in the formation of the dyads. Importantly, this means that the attachment of the ruthenium catalyst does not significantly disrupt the light-harvesting function of the porphyrins. Comparisons of the fluorescence of the dyads to that of the reference porphyrins indicate that a significant portion of this harvested energy is converted or transferred by some process other than the fluorescence seen in the unattached porphyrin. Most sources of this fluorescence quenching are ruled out by comparison to the fluorescence of the reference porphyrins, conducted under identical conditions and in a variety of solvents. The remaining reasonable sources of fluorescence quenching are electron or energy transfer, with electron transfer being the desirable process necessary to the function of the system. The spectra of the components of the dyads do overlap, but the nature of the overlap is not favorable towards energy transfer; the absorption of the ruthenium component is “uphill” relative to the fluorescence of the porphyrins (Figure 31). Therefore, the energetics are supportive of electron transfer being the underlying physical mechanism.

This electron transfer, resulting in the formation of a radical ion-pair, is the fundamental physical process needed to enable photosensitization of the system. At a basic level, the absorption of light-energy must result in electron separation which is long-lived enough for chemical work to be done (chemical work must be able to be done before recombination or relaxation).

The suitability of these systems is further supported by the electrochemical data, in which the aluminum porphyrins are shown to have several redox potentials in close proximity to those of the ruthenium catalyst. These redox values were also used to calculate the energies required for radical ion-pair formation. Comparisons between the optical and electrochemical data suggest that, from a theoretical standpoint, optical excitation of the porphyrins provides sufficient driving force to effect radical ion-pair formation of the dyads. The fluorescence quenching data empirically indicates that this does in fact happen.

3.3 FUTURE WORK

This document describes the physical properties of a procatalyst. A great deal of work remains before the ultimate goal can be reached: creation of a functioning device.

Additional titration studies must be done for the remaining two dyads, AlPorF3-Ru and AlPorF5-Ru. Transient absorption studies are currently being undertaken, the results of which were not ready at the time of this writing. Activated catalyst dyads have been prepared, and these must be fully characterized, as was done with the protocatalysts described in this work. Finally, the activated catalytic dyads can then be used to prepare prototypical photochemical devices, and the real-world performance of these photosensitized water oxidation catalysts can be assessed.

CHAPTER 4: EXPERIMENTAL DETAILS

Synthesis:

Unless otherwise specified, all chemicals and solvents were obtained from Alfa Aesar, MilliporeSigma, or Fisher Chemicals, and used as received. Chromatographic materials were purchased from either MilliporeSigma or Silicycle Inc. No solvents were freshly distilled, and where solvents are described "dry", water removal was accomplished by use of molecular sieves. In all cases where anaerobic conditions are specified, reactions were performed under N_2 gas, delivered by Schlenk line. In all cases where "dark" conditions are specified, light was excluded by simply wrapping the reaction vessels in aluminum foil.

Structural Characterization:

NMR were recorded on either a 500 MHz Varian Inova, or a 400 MHz Brucker Avance NEO. All NMR spectra are reported with shifts in ppm (parts per million).

Optical Studies:

UV-Vis spectra were gathered on an Agilent Cary 300 (instrument v12.00) scan software v4.20(470). Fluorescence spectra were recorded using a Photon Technologies International Quanta Master 8075-11 spectrofluorimeter, equipped with a 75 W xenon lamp, running with FelixGX software.

Electrochemistry:

In order to quantify redox potentials of all target and reference materials, both cyclic and differential pulse voltammetry were used. Electrochemical data was gathered on a BASi potentiostat, with a platinum working electrode, platinum wire auxiliary and silver reference electrode and by use of ferrocene as an internal standard, tetrabutylammonium.PF_6 as a supporting electrolyte, and HPLC grade acetonitrile as the solvent. Cyclic voltammetry settings were as follows: scan rate = 100 mV; current full scale = 100 μA; filter = 10 Hz; quiet time = 2 seconds. Differential pulse settings: step E = 4 mV; pulse amplitude = 50 mV; pulse width = 50 milliseconds; pulse period = 200 milliseconds; filter = 100 Hz; quiet time = 2 seconds.

Software:

Optical and electrochemical data was analyzed and plotted using Origin 2018 v95E. Unless otherwise notated, all molecule images, as well as related reaction schemes, were generated using ChemDraw Professional version 16.0.1.4 (77). NMR spectra were processed using MesReNova v12.0.0-20080. Word processing for the preparation of this document, as well as the construction of several tables, was performed using Microsoft Office 2016.

CHAPTER 5: SYNTHESIS

5.1 PORPHYRINS

THE ADLER-LONGO METHOD:

The method used to synthesize tetraphenyl porphyrins, shown in Scheme 1, was first developed by Rothemund[31], and improved upon by Adler and Longo[32]. This is an acid-catalyzed pyrrole/aldehyde condensation. The reaction is run open to air, using oxygen as an oxidant.

When the ester-derivatives are desired (as in Scheme 1), it is convenient to make the esters at the same time as the unsubstituted (symmetrical) tetraphenylporphyrin. When the proportions of the starting materials are as shown in Scheme 1, the products shown are produced in approximately equal proportions, and these two fractions can be easily separated via column chromatography. The higher-substituted fractions (i.e. disubstituted and trisubstituted) are also produced in minor portions; those fractions were not collected in this work.

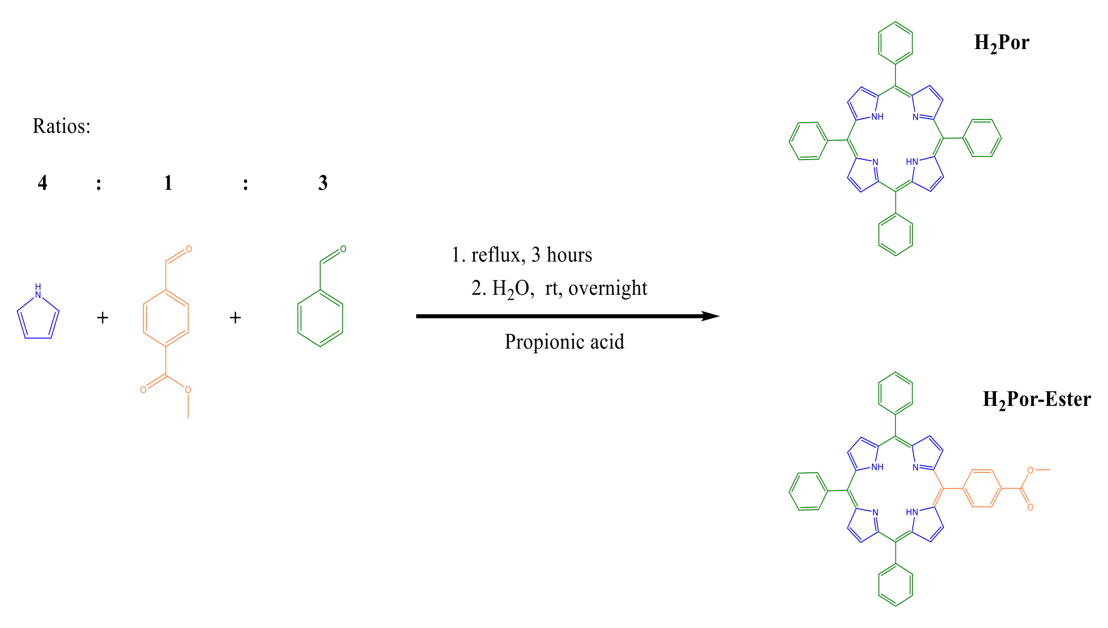

Scheme 1. Overview of a porphyrin synthesis showing all possible ester configurations. H_2Por and H_2Por-Ester are produced in nearly equal amounts.

Synthesis of 5,10,15,20-tetraphenylporphyrin, (H_2Por):

A mixture of benzaldehyde (0.70 mL, 6.9 mmol), methyl 4-formylbenzoate (377 mg, 2.3 mmol) and 40.0 mL of propionic acid were combined in a round-bottom flask and stirred at 100 °C. Pyrrole was added dropwise to this mixture (0.64 mL, 9.2 mmol). The mixture was then brought to reflux and stirred for 3 hours under dark conditions. The mixture was then cooled to room temperature, quenched with approximately 10 mL of deionized water, and then allowed to stir open to air overnight. The product was then filtered, and the resulting solid filter-cake was washed with approximately 100 mL of DI water. Thin layer chromatography revealed at least 4 distinct porphyrin products (alumina plate, 100% dichloromethane). Initial purification was done on a basic alumina column (100% dichloromethane eluent), during which the first two purple bands were collected and combined (due to being insufficiently resolved). Final purification was performed on a silica column (100% dichloromethane eluent), which successfully resolved the two pure porphyrin fractions.

Yield = 87.7 mg (6.2% based on pyrrole). ^{1}H NMR (500 MHz, Chloroform-*d*) δ 8.85 (s, 8H), 8.23 (d, *J* = 7.5 Hz, 8H), 7.76 (m, *J* = 8.1, 6.9 Hz, 12H), -2.76 (s, 2H).

Synthesis of Methyl 4-(10,15,20-triphenylporphyrin-5-yl)benzoate, (H_2Por-Ester):

Synthesis is identical to that for H_2Por, except the second fraction is collected, instead of the first.

Yield = 69.5 mg (5.7%). ^{1}H NMR (400 MHz, Chloroform-*d*) δ 8.88 (d, *J* = 2.6 Hz, 5H), 8.81 (d, *J* = 4.9 Hz, 2H), 8.47 (d, *J* = 8.1 Hz, 2H), 8.33 (d, *J* = 8.1 Hz, 2H), 8.24 (d, *J* = 7.4 Hz, 6H), 7.80 (t, *J* = 7.4 Hz, 10H), 4.14 (s, 3H), -2.75 (s, 2H).

THE LINDSEY METHOD:

The Adler-Longo method is carried out at relatively high temperatures, and this limits the aldehydes that can be used. In order to accommodate the fluorinated derivatives described below, a different method is needed. Such a method was developed by Lindsey and colleagues[33]. This 2-step procedure occurs at room temperature in dark, anaerobic conditions, and uses BF_3 or TFA as a catalyst. The mild conditions of this first step were designed to reach an equilibrium during condensation, minimizing the concentration of side-products. The second step involves the addition of DDQ or p-chloranil as a mild oxidizing agent, yielding the desired freebase porphyrin.

Synthesis of 5,10,15,20-tetrakis(3,4,5-trifluorophenyl)porphyrin, (H_2PorF3):

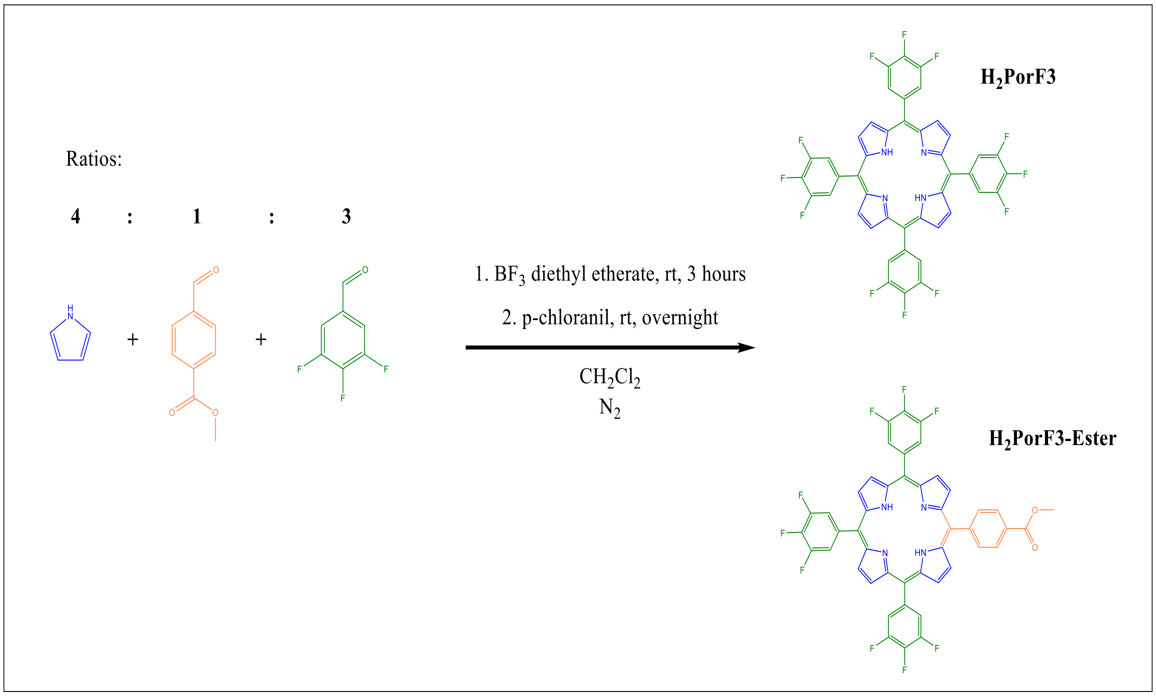

Scheme 2. Synthesis of H_2PorF3 and H_2PorF3-Ester.

Synthesis for H_2PorF_3 and its associated ester-derivatives proceeded similarly to that of the H_2PorF5 derivatives; a mixture of 4-methylcarboxybenzaldehyde (2.15 mmol, 0.35 g), pyrrole (8.6 mmol, 0.6 mL), and HPLC grade DCM was placed into a flask. The reaction system was then purged with N_2 gas for 30 minutes, after which time 3,4,5-trifluorobenzaldehyde (6.8 mmol, 0.77 mL) was added via syringe. After being allowed to stir for approximately 30 minutes, $BF_3\cdot$ diethyl etherate (0.22 mL) was added. After 3 hours of stirring, p-chloranil (4.18 g) was added, and the mixture was then allowed to continue stirring at room-temperature overnight. Purification was achieved by column chromatography (silica column, DCM/hexanes = 50:50), with the product (H_2PorF_3) being collected in the first fraction.

Yield = 388.6 mg (21.75% based on pyrrole).^1H NMR ^1H NMR (300 MHz, Chloroform-*d*) δ 8.90 (s, 8H), 7.86 (t, *J* = 6.7 Hz, 8H), -2.99 (s, 2H).

Synthesis of methyl 4-(10,15,20-tris(3,4,5-trifluorophenyl)porphyrin-5-yl)benzoate, (H_2PorF3-Ester):

The synthetic method for producing H2PorF3-Ester is the same as that for H_2PorF3, except the second fraction is collected, instead of the first.

Yield = 301.0 mg (16.77% based on pyrrole).

Synthesis of 5,10,15,20-tetrakis(pentafluorophenyl)porphyrin, (H_2PorF5):

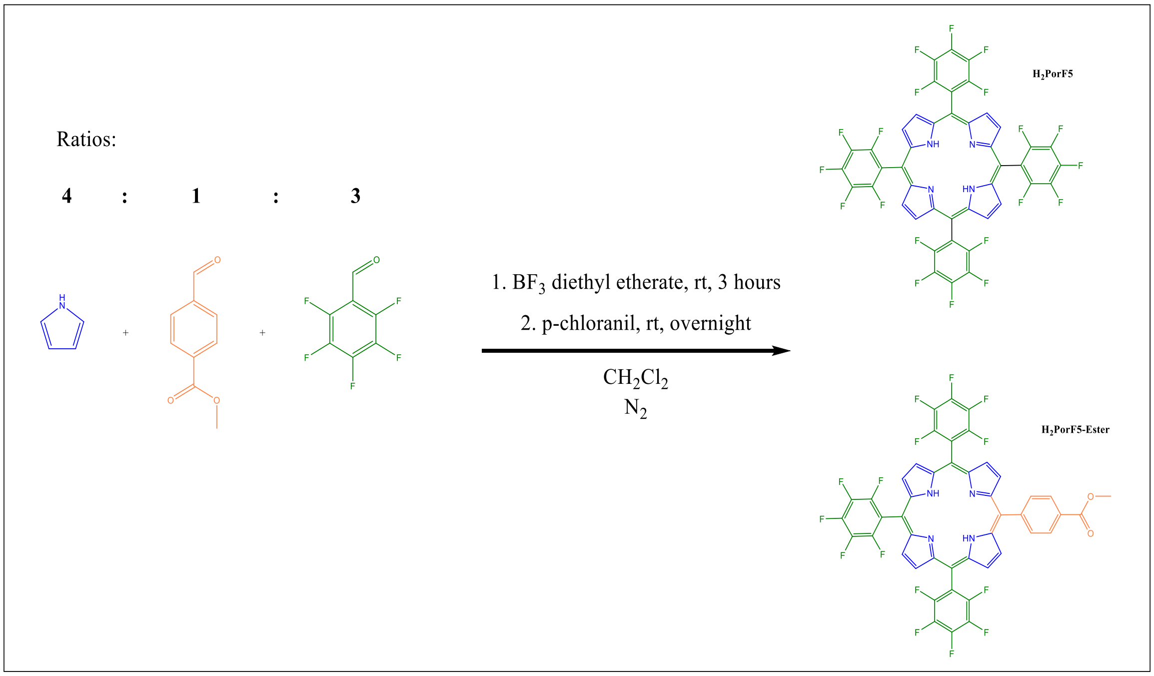

Scheme 3. Synthesis of H2PorF3 and H2PorF3-Ester

Into a round-bottom flask containing 1.25 L of CH_2Cl_2 was placed pyrrole (0.750 mL, 10.75 mmol), 2,3,4,5,6-pentafluorobenzaldehyde (0.77 mL, 3.70 mmol), and 4-methylcarboxybenzaldehyde (0.35 g, 2.13 mmol). The pentafluorobenzaldehyde was first melted by placing the container in a lukewarm water bath, then transferred to the flask via syringe. This mixture and reaction system was then thoroughly purged with N_2 (including directly bubbling N_2 into the stirring solution) for approximately 45 minutes. Once the long N_2 needle was removed from the solution (still leaving the system open to the N_2 Schlenk line), 0.21 mL of $BF_3 \cdot Et_2O$ was added to the flask via syringe. The flask was then covered in aluminum foil, and left to stir at room temperature for approximately 3.5 hours.

Once this time had elapsed, 4.18 g of p-chloranil was added into the flask, and the system was left to stir overnight at room temperature. Purification was achieved by column chromatography (silica column, DCM/hexanes = 50:50), with the product being collected in the first fraction. **Yield = 300 mg (11.45% based on pyrrole)**. 1H NMR (500 MHz, Chloroform-d) δ 8.93 (s, 8H), -2.90 (s, 2H).

Synthesis of methyl 4-(10,15,20-tris(perfluorophenyl)porphyrin-5-yl)benzoate (H_2PorF5-monoester):

Synthesis was the same as that for H_2PorF_5, except that the second fraction is collected instead of the first.

Yield = 367 mg (14.49% based on pyrrole). ^{1}H NMR (500 MHz, Chloroform-*d*) δ 8.91 (s, 6H), 8.84 (s, 2H), 8.51 – 8.46 (d, *J* = 8.2 Hz 2H), 8.31 (d, *J* = 7.3 Hz, 2H), 4.13 (s, 3H), -2.86 (s, 2H).

Preparation of Aluminum(III) Porphyrins:

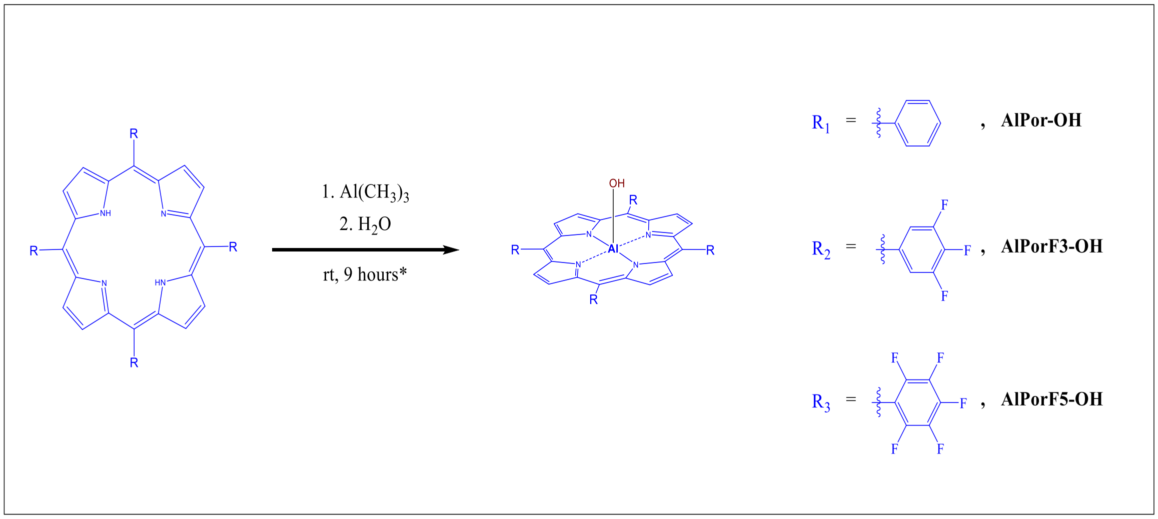

Scheme 4. Aluminum metalation of freebase porphyrins. The procedure is the same for both the nonfluorinated and pentafluorinated derivatives. *In the case of the trifluorinated derivative, low solubility of the porphyrin necessitated a longer reaction time described below).

Preparation of 5,10,15,20-tetraphenylporphyrinatoaluminum(III) hydroxide, (AlPor-OH), from H_2Por:

A mixture of 1 g of H_2Por and 60 mL of dry toluene were placed into a flask, and the reaction system was flushed with N_2 for 20 minutes, at which time 1 mL of trimethylaluminum was added. The solution was stirred at room temperature under nitrogen for 9 hours, at which time the reaction was quenched by addition of 5 mL of DI H_2O, then left to stir overnight. The solvent was then removed under reduced pressure, then re-dissolved in DCM/MeOH to allow for dry-packing of an alumina column. Pure DCM was used to elute-off unreacted freebase porphyrin. Following this, a 5% MeOH/95% DCM mixture was used to collect the product. This second fraction was collected, and the solvent removed under reduced pressure, producing the pure product as a purple opaque solid. Yield = 1.244 g (91.5%). ^{1}H NMR (500 MHz, Chloroform-*d*) δ 9.02 (s, 8H), 8.20 (s, 8H), 7.77 (m, 12H).

Preparation of 5,10,15,20-tetrakis(3,4,5-trifluorophenyl)porphyrinatoaluminum(III) hydroxide, (AlPorF3-OH), from H_2PorF_3:

The procedure is largely the same as for that of the nonfluorinated porphyrins. In the case of H_2PorF_3, the reaction is run for at least 5 days (as opposed to 4 hours), and a larger volume of solvent was used. This is due to the lower solubility of this porphyrin in toluene.

A mixture of 173 mg of H_2PorF_3 and 200 mL of dry toluene were placed into a flask, and the reaction system was flushed with N_2 for 20 minutes, at which time 1 mL of trimethylaluminum was added via syringe. The solution was stirred at room temperature under nitrogen for 6 days, at which time the reaction was quenched by addition of 5 mL of DI H_2O, then left to stir overnight. The solvent was then removed under reduced pressure, then re-dissolved in DCM/MeOH to allow for dry-packing of an alumina column. Pure DCM was used to elute-off unreacted freebase porphyrin. Following this, a 5% MeOH/95% DCM mixture was used to collect the product. This second fraction was collected, and the solvent removed under reduced pressure, producing the pure product as a purple opaque solid. Yield = 150 mg (91%). ^{1}H NMR (500 MHz, Acetonitrile-d_3) δ 9.13 (s, 8H), 8.02 (t, J = 7.5 Hz, 8H)

Preparation of Aluminum of 5,10,15,20-tetrakis(pentafluorophenyl)porphyrinatoaluminum(III) hydroxide (AlPorF$_5$-OH) from H$_2$PorF$_5$:

A mixture of 0.90 g of H$_2$PorF$_5$ and 200 mL of dry toluene were placed into a flask, and the reaction system was flushed with N_2 for 20 minutes, at which time 1 mL of trimethylaluminum was added via syringe. The solution was stirred at room temperature under nitrogen overnight, at which time the reaction was quenched by addition of 5 mL of DI H_2O, then left to stir approximately 4 hours. The solvent was then removed under reduced pressure, then re-dissolved in DCM/MeOH to allow for dry-packing of an alumina column. Pure DCM was used to elute-off unreacted freebase porphyrin. Following this, a 5% MeOH/95% DCM mixture was used to collect the product. This second fraction was collected, and the solvent removed under reduced pressure, producing the pure product as a purple opaque solid. Yield = 0.88 g (63%). ^{1}H NMR (400 MHz, Chloroform-*d*) δ 9.09 (s, 8H).

5.2 RUTHENIUM CATALYSTS

Preparation of Ru(II) catalyst:

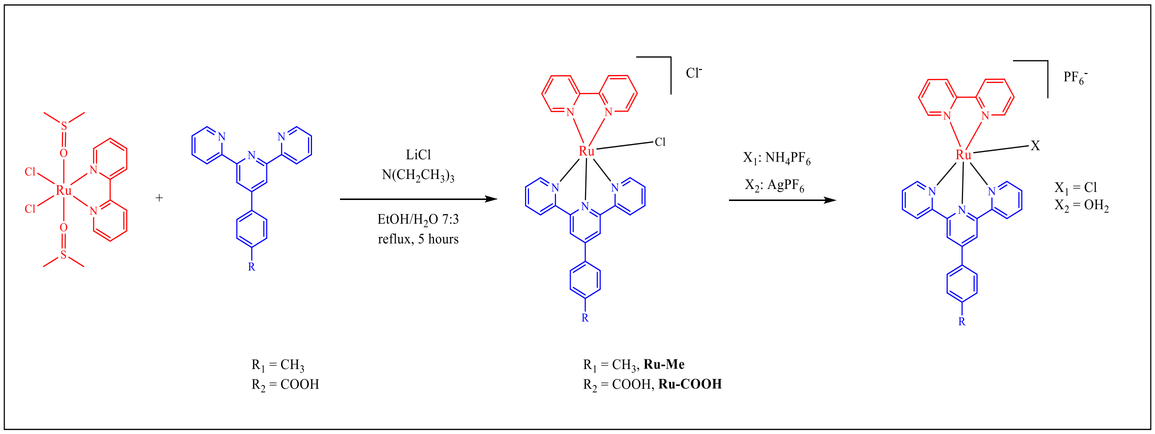

Scheme 5. Synthesis of the ruthenium catalyst and reference molecule.

[Ru(bpy)(DMSO)$_2$Cl$_2$]Cl: A mixture of reagent grade ethanol (4.25 mL, 99.5% purity), DMSO (0.55 mL), and 67 mg of 2,2’-bipyridine (bpy) was stirred under reflux for 20 minutes. To this was slowly added a mixture of $RuCl_3 \cdot 3H_2O$ (88.2mg, 0.426 mmol) in ethanol (4.25 mL); this was done by dropwise addition of approximately 1 mL aliquots spaced in 5-minute intervals. Once the addition of the above ruthenium mixture was complete, the mixture was stirred under reflux for 5 hours. This was followed by hot-filtration under vacuum, and successive washing with 10 mL of cold ethanol, then 75 mL of diethyl ether. This resulted in the product as a coppery-opaque powder. **Yield: 86 mg** (46% based on Ru center).

Preparation of [Ru(bpy)(tpy-ph-CH$_3$)Cl]Cl, (Ru-Me):

A mixture of LiCl (31.1 mg), 4'-(4-methylphenyl)-2,2':6',2"-terpyridine, (206.3 mg) and [Ru(bpy)2(DMSO)Cl$_2$]Cl (394.5 mg) were placed into a round bottom flask.. Into this was placed 35 mL of EtOH, 15 mL of DI H_2O and 150 μL of $N(CH_2CH_3)_3$. The mixture was stirred at reflux for 5.5 hours, hot-filtered, and the solvent was then removed under reduced pressure. The product was then recrystallized by first dissolving in MeOH, then pouring into an excess of diethyl ether, and filtered to yield the product as a reddish-brown opaque solid. Yield = 460 mg (79.6%). ^{1}H NMR (500 MHz, cd_3cn) δ 10.24, 10.23, 8.74, 8.74, 8.62, 8.60, 8.53, 8.52, 8.33, 8.31, 8.27, 8.26, 8.24, 8.02, 8.01, 7.97, 7.96, 7.95, 7.90, 7.89, 7.87, 7.68, 7.67, 7.65, 7.51, 7.49, 7.37, 7.36, 7.28, 7.27, 7.26, 6.96, 6.95, 6.93, 2.50, 2.15, 1.94.

Preparation of [Ru(bpy)(tpy-ph-COOH)Cl]Cl, (Ru-COOH):

Into a RBF was placed sodium 4-([2,2':6',2''-terpyridin]-4'-yl)benzoate (170 mg), $[Ru(bpy)(DMSO)_2(tpy\text{-}ph\text{-}COONa)]Cl_2Cl$ (200 mg), LiCl (25 mg), Et_3N (1 mL), EtOH (25 mL), and DI H_2O (8.75 mL). The above was stirred at reflux for 5 hours, then hot-filtered (gravity filtration through fast filter paper), and the solvent was then removed under reduced pressure. The product was then recrystallized by first dissolving in MeOH, then pouring into an excess of diethyl ether, and filtered to yield the product as a reddish-brown opaque solid. Yield = 300 mg (96%). ^{1}H NMR (500 MHz, DMSO-d_6) δ 10.09 (d, J = 5.5 Hz, 1H), 9.23 (s, 2H), 8.94 (dd, J = 13.6, 8.2 Hz, 3H), 8.64 (d, J = 8.2 Hz, 1H), 8.45 (d, J = 8.3 Hz, 2H), 8.36 (t, J = 7.8 Hz, 1H), 8.21 (d, J = 8.2 Hz, 2H), 8.07 (t, J = 6.7 Hz, 1H), 8.06 – 7.98 (m, 2H), 7.77 (t, J = 7.5 Hz, 1H), 7.63 (d, J = 5.5 Hz, 2H), 7.40 (q, J = 4.6 Hz, 3H), 7.07 (t, J = 6.7 Hz, 1H).

5.3 PREPARATION OF PORPHYRIN-CATALYST DYADS

The assembly of the aluminum porphyrin/ruthenium catalyst dyads is straightforward. In short, the respective monomers are simply dissolved, mixed together, and the ester linkage forms. This is accomplished at room temperature, and the reaction goes to completion in under 30 minutes, without the need for a catalyst. A set of reference compounds were made, as shown in the figure below. These were used to help isolate the change in behavior arising from communication between the aluminum porphyrins and ruthenium catalysts, as opposed to that arising from simple changes in structure and connectivity.

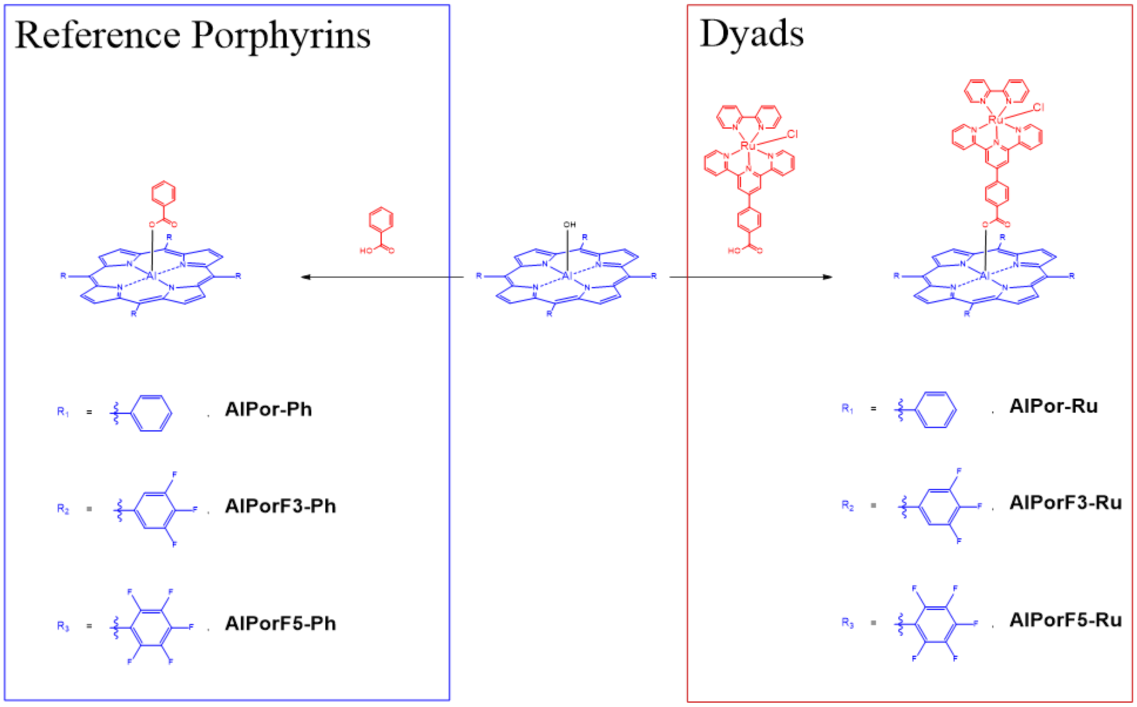

Figure 35. Structure and naming conventions of the ruthenium-porphyrin dyads, as well as the related reference porphyrins

5.4 PREPARATION OF THE FULLERENE LIGAND

Preparation of N-Methyl-20-(4-(1H-imidazol-1-yl)phenyl)-pyrrolidino-[30,40:1,2][60]fullerene, (C60-Im):

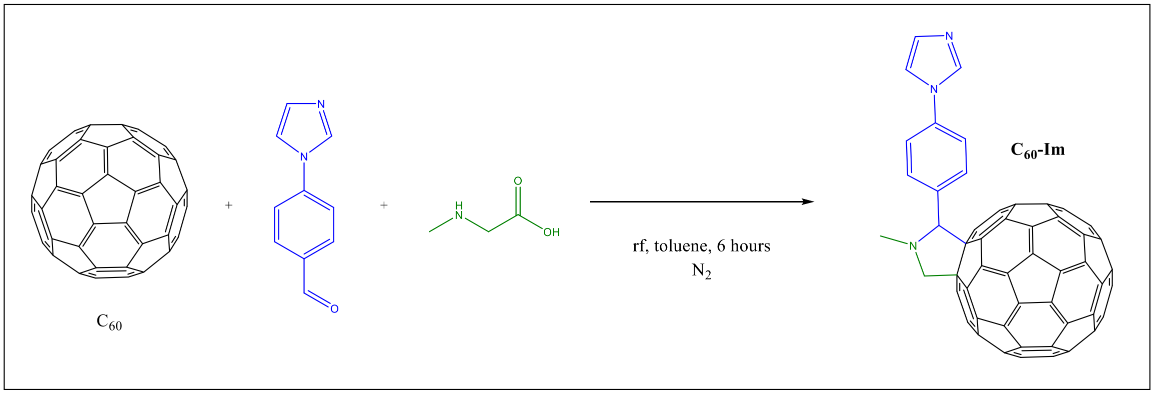

Scheme 6. C_{60}-Im synthesis.

A mixture of 50.0 mg of C_{60} fullerene, 15.5 mg sarcosine, and 26.0 mg of 4-imidazolyl benzaldehyde, and 40 mL of toluene were refluxed under nitrogen for 6 hours. This mixture was then cooled to room temperature, and the solvent was removed under reduced pressure. Thin layer chromatography on the resulting black solid product (alumina plate, 75/25 toluene/ethyl acetate) revealed the presence of at least 2 species. Thin layer chromatography done on alumina produced better separation than that done on a silica plate, and therefore alumina was chosen for purification by column-chromatography. This was done by first using pure toluene to elute off the purple C_{60} band, then 75/25 toluene/ethyl acetate to produce the desired product as a brown solid. Subsequent to removal of the solvent under reduced pressure, proton NMR was performed, which showed the presence of significant aldehyde impurity. Subsequent washing with methanol removed this impurity, finally producing the pure product. Yield = 12.5 mg, (20% yield).

BIBLIOGRAPHY

(1) Schmidt, G. A.; Ruedy, R. A.; Miller, R. L.; Lacis, A. A. Attribution of the Present-day Total Greenhouse Effect; 2010. https://doi.org/10.1029/2010JD014287.

(2) The Causes of Climate Change https://climate.nasa.gov/causes (accessed Apr 21, 2020).

(3) Climate and Earth's Energy Budget https://earthobservatory.nasa.gov/features/EnergyBalance/page2.php (accessed Apr 22, 2020).

(4) Daedalus, or, Science and the Future http://bactra.org/Daedalus.html (accessed Apr 23, 2020).

(5) A Hydrogen Economy. 2.

(6) Bockris, J. The Hydrogen Economy: Its History. *Int. J. Hydrog. Energy* **2013**, *38*, 2579–2588. https://doi.org/10.1016/j.ijhydene.2012.12.026.

(7) Centaur Rocket.Pdf.

(8) Das et al. - 2017 - Recent Advances and Challenges of Fuel Cell Based .Pdf.

(9) Das, V.; Padmanaban, S.; Venkitusamy, K.; Selvamuthukumaran, R.; Blaabjerg, F.; Siano, P. Recent Advances and Challenges of Fuel Cell Based Power System Architectures and Control – A Review. *Renew. Sustain. Energy Rev.* **2017**, *73*, 10–18. https://doi.org/10.1016/j.rser.2017.01.148.

(10) Hydrogen Production Pathways https://www.energy.gov/eere/fuelcells/hydrogen-production-pathways (accessed Apr 24, 2020).

(11) de Levie, R. The Electrolysis of Water. *J. Electroanal. Chem.* **1999**, *476* (1), 92–93. https://doi.org/10.1016/S0022-0728(99)00365-4.

(12) Bratsch - 1989 - Standard Electrode Potentials and Temperature Coef.Pdf.

(13) Gersten, S. W.; Samuels, G. J.; Meyer, T. J. Catalytic Oxidation of Water by an Oxo-Bridged Ruthenium Dimer. *J. Am. Chem. Soc.* **1982**, *104* (14), 4029–4030. https://doi.org/10.1021/ja00378a053.

(14) Patel, J.; Majee, K.; Ahmad, E.; Das, B.; Padhi, S. K. Effect of Pyridyl Substitution on Chemical and Photochemical Water Oxidation by [Ru(Terpyridine)(Bipyridine)(OH $_2$)] $^{2+}$ Scaffolds: Effect of Pyridyl Substitution on Chemical and Photochemical Water Oxidation by [Ru(Terpyridine)(Bipyridine)(OH $_2$)] $^{2+}$ Scaffolds. *Eur. J. Inorg. Chem.* **2017**, *2017* (1), 160–171. https://doi.org/10.1002/ejic.201601193.

(15) Patel, J.; Majee, K.; Ahmad, E.; Vatsa, A.; Das, B.; Padhi, S. K. Electronic Effect on Catalytic Water Oxidation by Single Site [Ru(QCl-Tpy)(Bpy)(OH $_2$)] $^{2+}$ Catalyst. *ChemistrySelect* **2017**, *2* (1), 123–129. https://doi.org/10.1002/slct.201601914.

(16) Vogel, E. The Porphyrins from the “annulene Chemist’s” Perspective. *Pure Appl. Chem.* **1993**, *65* (1), 143–152. https://doi.org/10.1351/pac199365010143.

(17) Sayer, P.; Gouterman, M.; Connell, C. R. Porphyrins. 34. Phosphorus Complexes of Octaethylporphyrin. *J. Am. Chem. Soc.* **1977**, *99* (4), 1082–1087. https://doi.org/10.1021/ja00446a018.

(18) Harriman, A. Luminescence of Porphyrins and Metalloporphyrins VII: Luminescence of Phosphorus Tetraphenylporphyrins. *J. Photochem.* **1983**, *23* (1), 37–43. https://doi.org/10.1016/0047-2670(83)80074-4.

(19) Kunimoto, K.; Segawa, H.; Shimidzu, T. Selective Synthesis of Unsymmetrical Dialkoxyphosphorus(V)Tetraphenylporphine Derivatives by Stepwise Substitution of Axial Position. *Tetrahedron Lett.* **1992**, *33* (42), 6327–6330. https://doi.org/10.1016/S0040-4039(00)60965-6.

(20) Gamgee, A. On the Absorption of the Extreme Violet and Ultra-Violet Rays of the Solar Spectrum by Haemoglobin, Its Compounds, and Certain of Its Derivatives. *Proc. R. Soc. Lond.* **1895**, *59*, 276–279.

(21) Gouterman, M.; Wagnière, G. H.; Snyder, L. C. Spectra of Porphyrins: Part II. Four Orbital Model. *J. Mol. Spectrosc.* **1963**, *11* (1), 108–127. https://doi.org/10.1016/0022-2852(63)90011-0.

(22) Gouterman, M. Spectra of Porphyrins. *J. Mol. Spectrosc.* **1961**, *6*, 138–163. https://doi.org/10.1016/0022-2852(61)90236-3.

(23) Ceulemans et al. - 1986 - Gouterman’s Four-Orbital Model and the MCD Spect.Pdf.

(24) Ceulemans, A.; Oldenhof, W.; Gorller-Walrand, C.; Vanquickenborne, L. G. Gouterman’s “Four-Orbital” Model and the MCD Spectra of High-Symmetry Metalloporphyrins. *J. Am. Chem. Soc.* **1986**, *108* (6), 1155–1163. https://doi.org/10.1021/ja00266a007.

(25) Kandrashkin, Y. E.; Poddutoori, P. K.; van der Est, A. Electron Transfer Pathways in a Tetrathiafulvalene-Aluminum(III) Porphyrin-Free-Base Porphyrin Triad Studied Using Electron Spin Polarization. *Appl. Magn. Reson.* **2016**, *47* (5), 511–526. https://doi.org/10.1007/s00723-016-0774-8.

(26) Lim et al. - 2017 - Interfacial Electron Transfer Followed by Photooxi.Pdf.

(27) Poddutoori, P. K.; Bregles, L. P.; Lim, G. N.; Boland, P.; Kerr, R. G.; D’Souza, F. Modulation of Energy Transfer into Sequential Electron Transfer upon Axial Coordination of Tetrathiafulvalene in an Aluminum(III) Porphyrin–Free-Base Porphyrin Dyad. *Inorg. Chem.* **2015**, *54* (17), 8482–8494. https://doi.org/10.1021/acs.inorgchem.5b01190.

(28) Akins, D. L.; Zhu, H.-R.; Guo, C. Aggregation of Tetraaryl-Substituted Porphyrins in Homogeneous Solution. *J. Phys. Chem.* **1996**, *100* (13), 5420–5425. https://doi.org/10.1021/jp951467c.

(29) Lash, T. D. Modification of the Porphyrin Chromophore by Ring Fusion: Identifying Trends Due to Annelation of the Porphyrin Nucleus. *J. Porphyr. Phthalocyanines* **2001**, *5* (3), 267–288. https://doi.org/10.1002/jpp.313.

(30) Chen, T.; He, B.; Tao, J.; He, Y.; Deng, H.; Wang, X.; Zheng, Y. Application of Förster Resonance Energy Transfer (FRET) Technique to Elucidate Intracellular and In Vivo Biofate of Nanomedicines. *Adv. Drug Deliv. Rev.* **2019**, *143*, 177–205. https://doi.org/10.1016/j.addr.2019.04.009.

(31) Rothemund, P. A New Porphyrin Synthesis. The Synthesis of Porphin1. *J. Am. Chem. Soc.* **1936**, *58* (4), 625–627. https://doi.org/10.1021/ja01295a027.

(32) Adler, A. D.; Longo, F. R.; Finarelli, J. D.; Goldmacher, J.; Assour, J.; Korsakoff, L. A Simplified Synthesis for Meso-Tetraphenylporphine. *J. Org. Chem.* **1967**, *32* (2), 476–476. https://doi.org/10.1021/jo01288a053.

(33) Lindsey, J. S. The Synthesis of Meso-Substituted Porphyrins. In *Metalloporphyrins Catalyzed Oxidations*; Montanari, F., Casella, L., Eds.; Ugo, R., James, B. R., Series Eds.; Catalysis by Metal Complexes; Springer Netherlands: Dordrecht, 1994; Vol. 17, pp 49–86. https://doi.org/10.1007/978-94-017-2247-6_2.

CHAPTER 6: APPENDICES

6.1 NMR

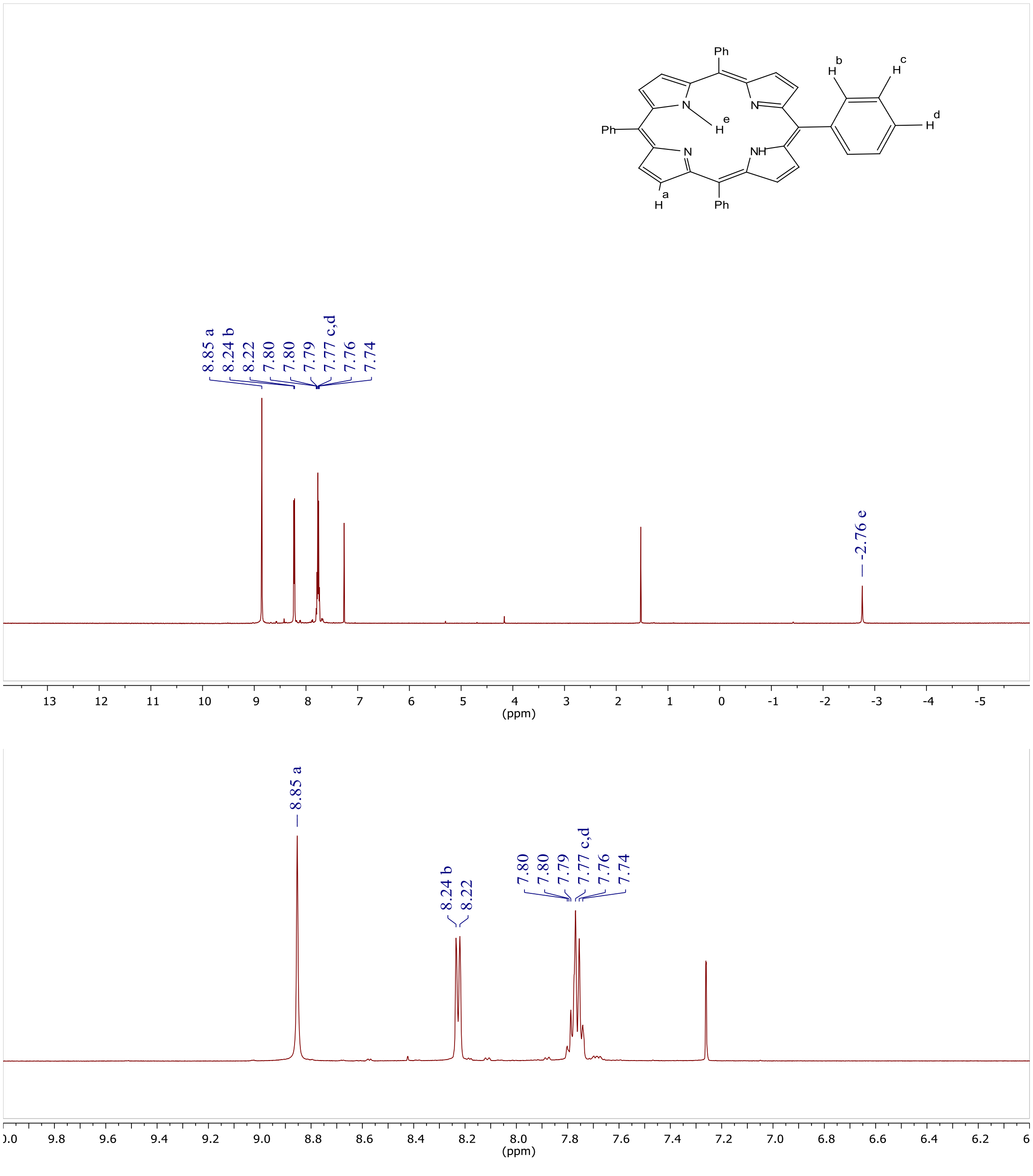

Figure 36. H_2Por proton NMR.

H_2Por: ^{1}H NMR (500 MHz, Chloroform-*d*) δ 8.85 (s, 8H), 8.23 (d, *J* = 7.5 Hz, 8H), 7.76 (m, *J* = 8.1, 6.9 Hz, 12H), -2.76 (s, 2H).

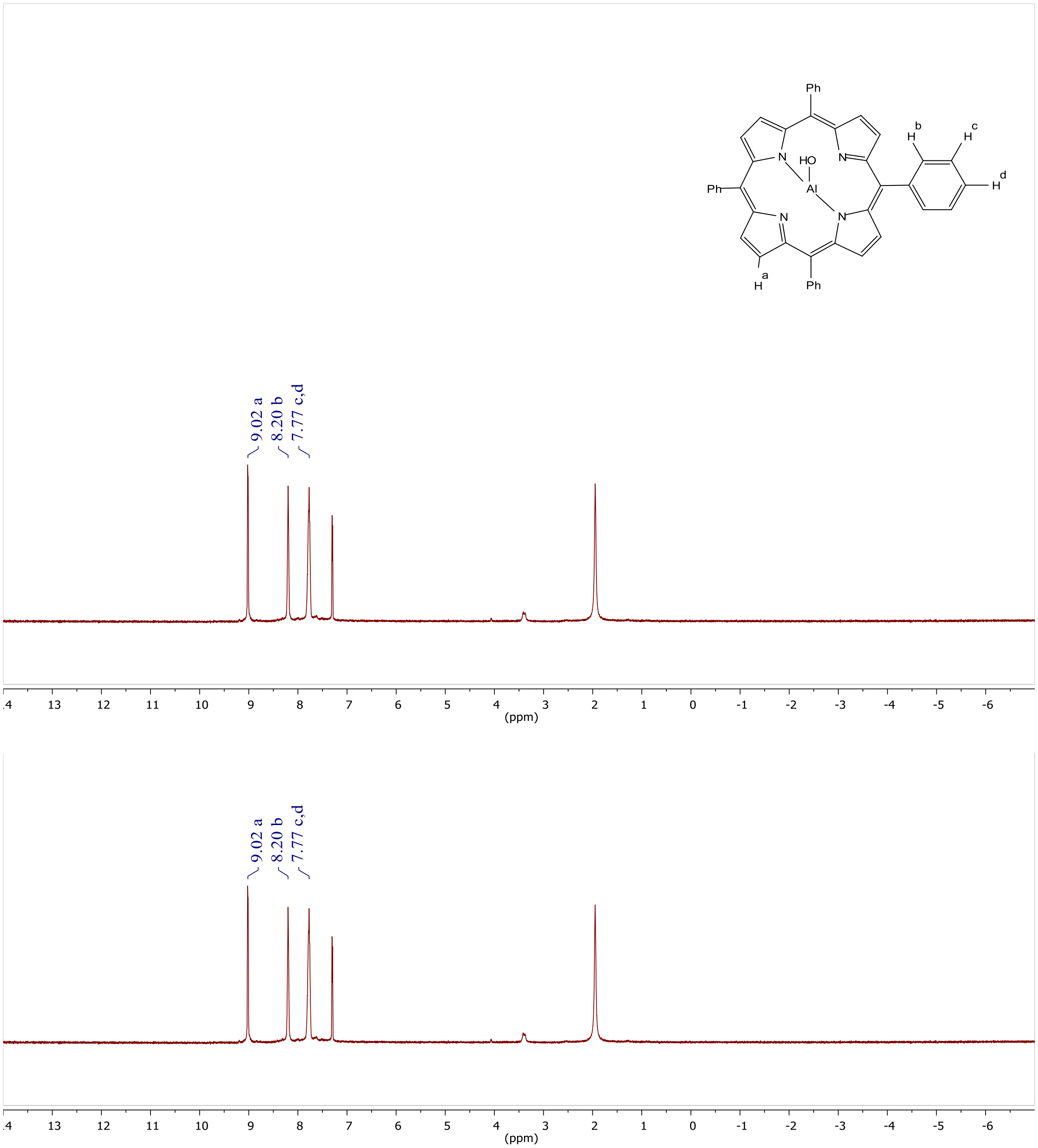

Figure 37. AlPor-OH proton NMR.

AlPor-OH: ^{1}H NMR (500 MHz, Chloroform-*d*) δ 9.02 (s, 8H), 8.20 (s, 8H), 7.77 (m, 12H).

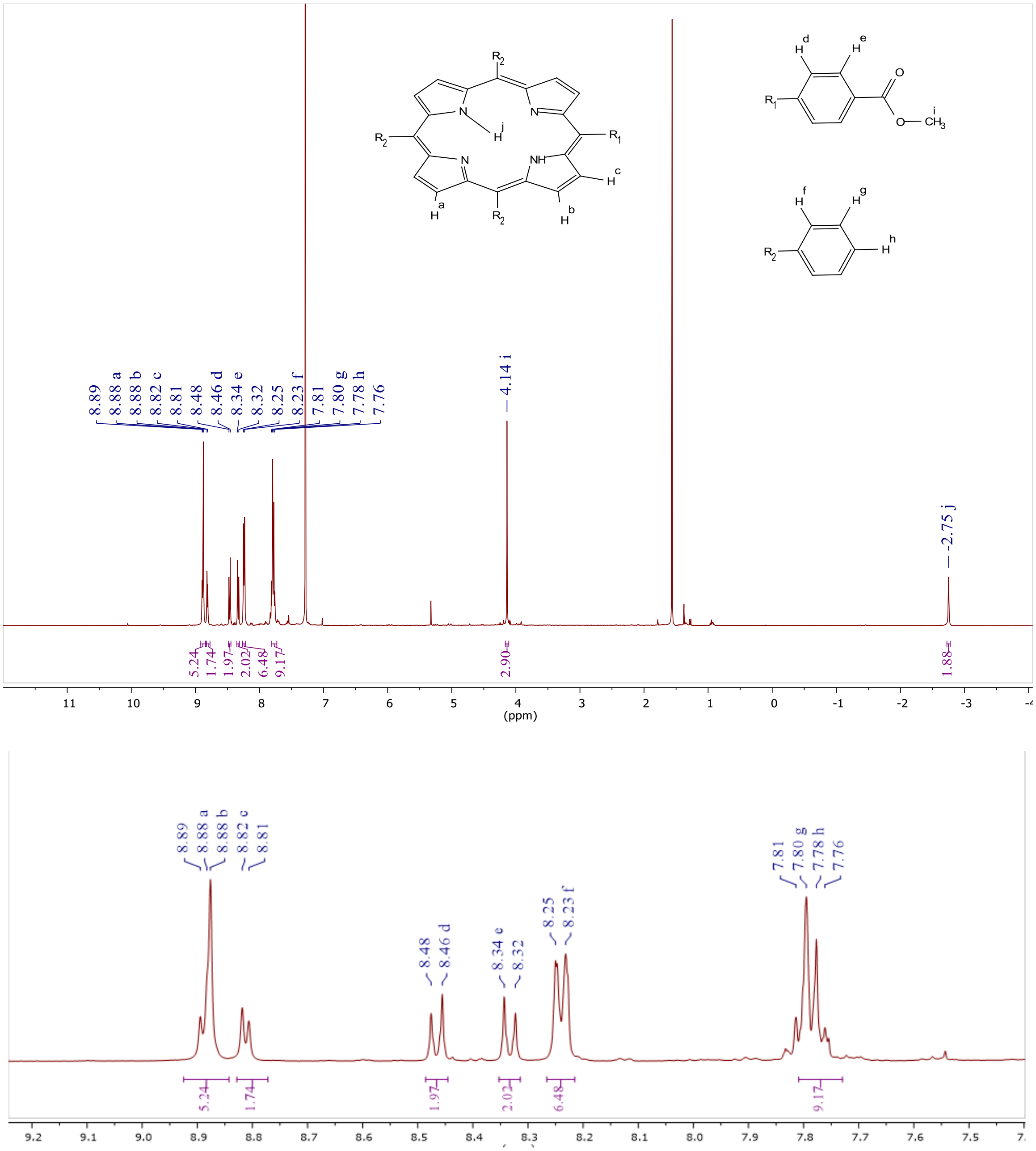

Figure 38. H_2Por-Ester proton NMR.

H_2Por-Ester. 1H NMR (400 MHz, Chloroform-d) δ 8.88 (d, J = 2.6 Hz, 6H), 8.81 (d, J = 4.9 Hz, 2H), 8.47 (d, J = 8.1 Hz, 2H), 8.33 (d, J = 8.1 Hz, 2H), 8.24 (d, J = 7.4 Hz, 6H), 7.79 (d, J = 7.3 Hz, 9H), 4.14 (s, 3H), -2.75 (s, 2H)

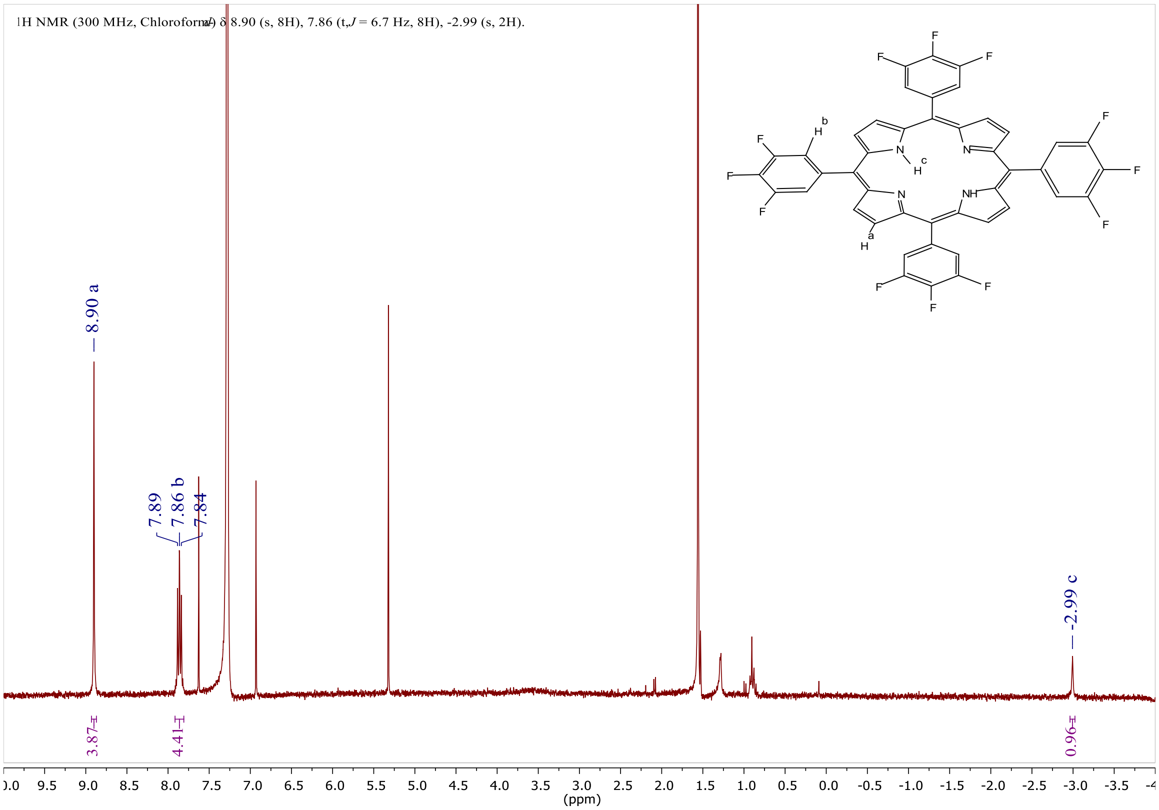

Figure 39. H_2PorF3

H_2PorF3. ^{1}H NMR (300 MHz, Chloroform-*d*) δ 8.90 (s, 8H), 7.86 (t, *J* = 6.7 Hz, 8H), -2.99 (s, 2H).

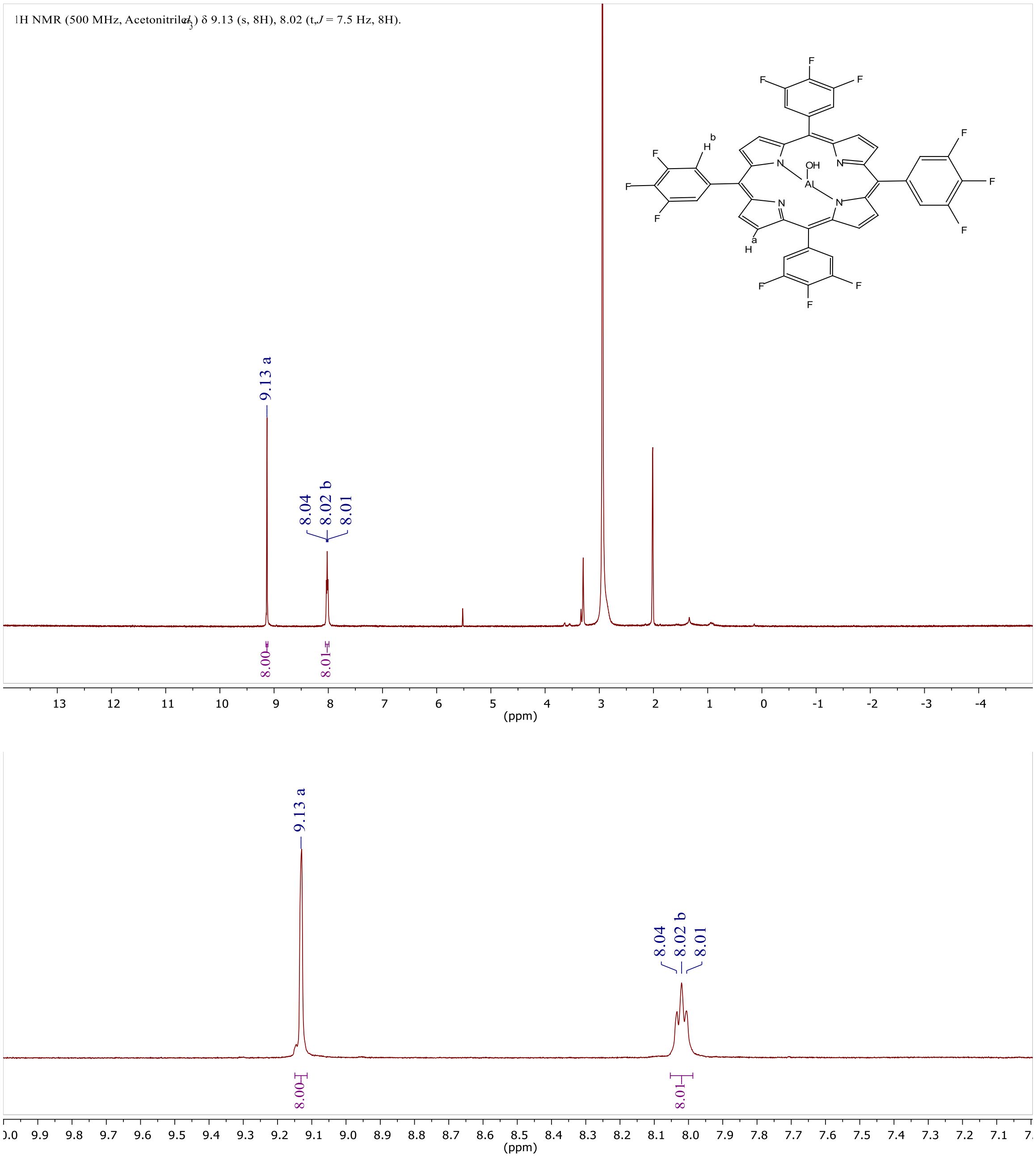

Figure 40. AlPorF3-OH proton NMR.

AlPorF$_3$-OH. ^{1}H NMR (500 MHz, Acetonitrile-d_3) δ 9.13 (s, 8H), 8.02 (t, J = 7.5 Hz, 8H)

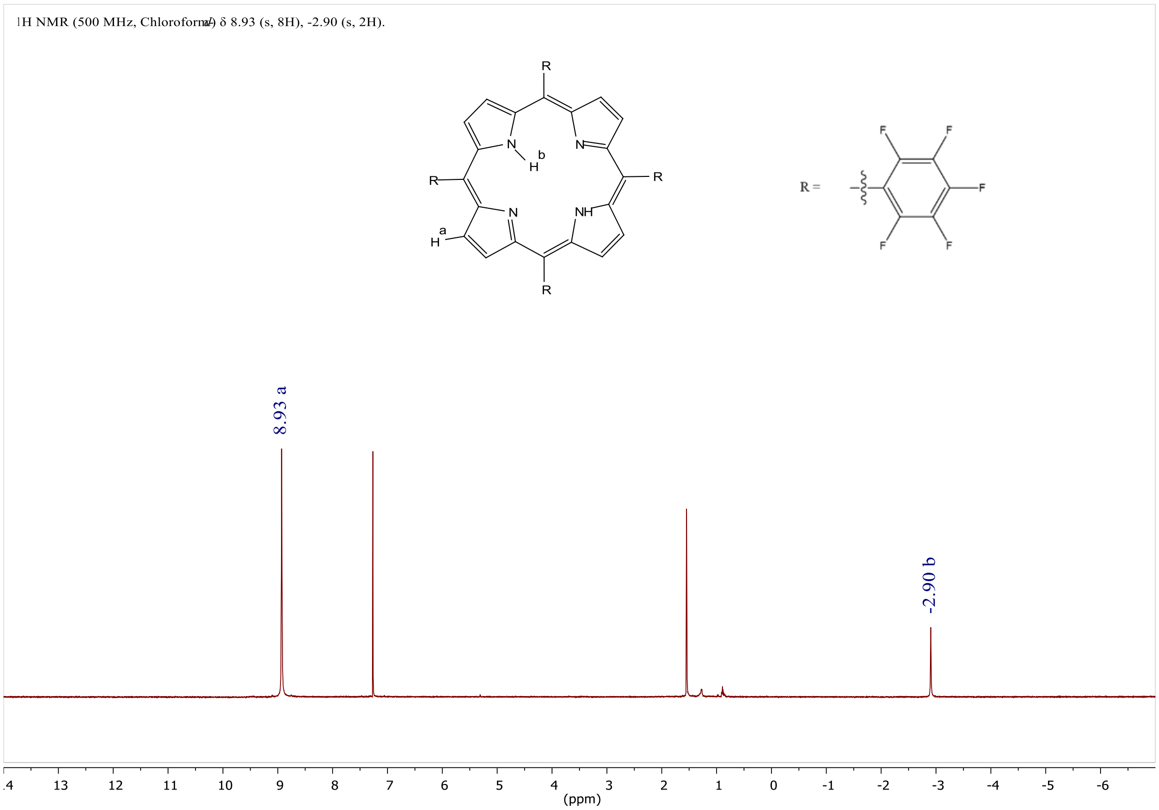

Figure 41. H_2PorF5 proton NMR.

H_2PorF5. ^{1}H NMR (500 MHz, Chloroform-d) δ 8.93 (s, 8H), -2.90 (s, 2H).

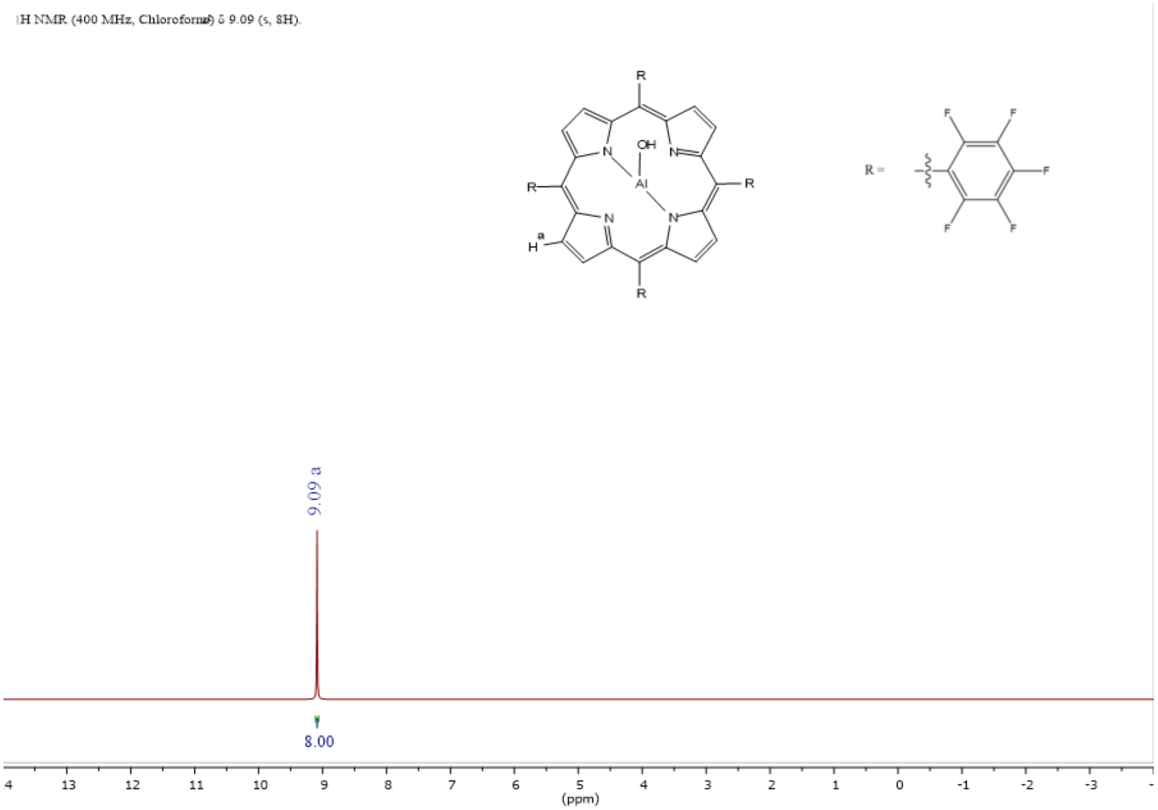

Figure 42. AlPorF5-OH proton NMR.

AlPorF5-OH. ^{1}H NMR (400 MHz, Chloroform-*d*) δ 9.09 (s, 8H).

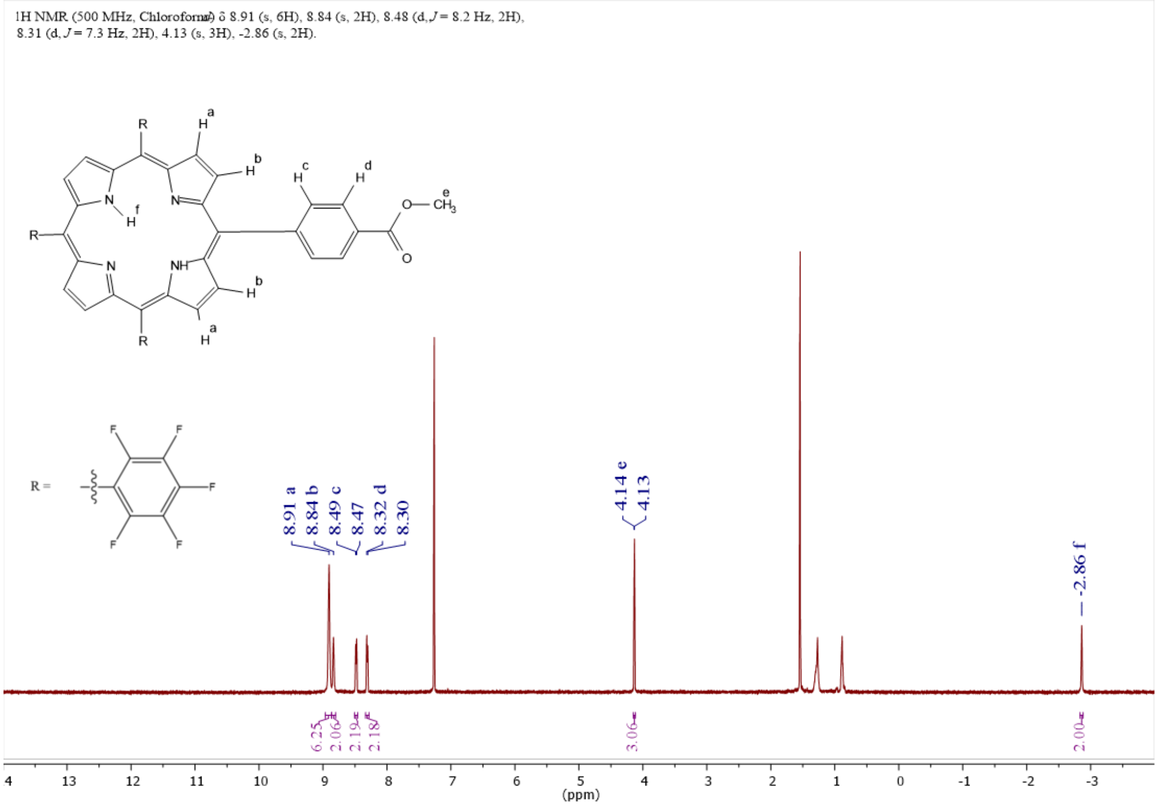

1H NMR (500 MHz, Chloroform-d) δ 8.91 (s, 6H), 8.84 (s, 2H), 8.48 (d, J = 8.2 Hz, 2H), 8.31 (d, J = 7.3 Hz, 2H), 4.13 (s, 3H), -2.86 (s, 2H).

Figure 43. H_2PorF5-Ester proton NMR.

H_2PorF5-Ester. ^{1}H NMR (500 MHz, Chloroform-*d*) δ 8.91 (s, 6H), 8.84 (s, 2H), 8.48 (d,, J = 8.2 Hz, 2H), 8.31 (d, J = 7.3 Hz, 2H), 4.13 (s, 3H), -2.86 (s, 2H).

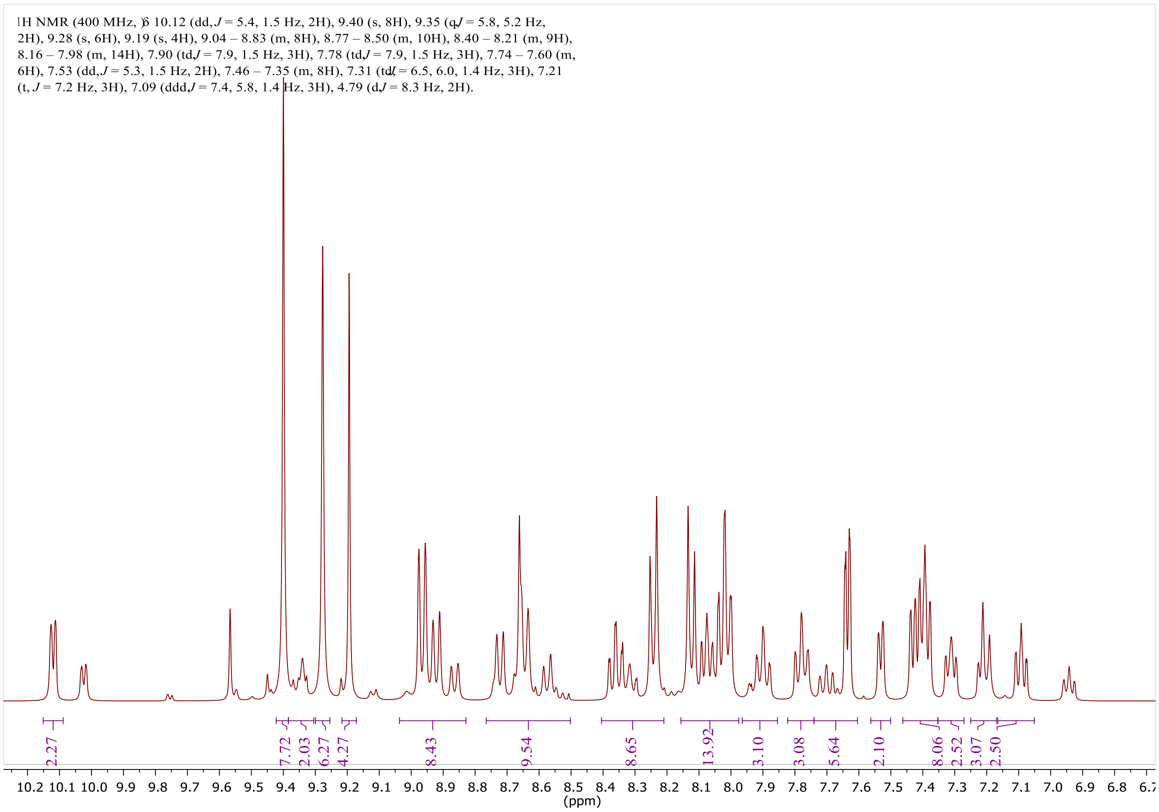

1H NMR (400 MHz,)δ 10.12 (dd, *J* = 5.4, 1.5 Hz, 2H), 9.40 (s, 8H), 9.35 (q, *J* = 5.8, 5.2 Hz, 2H), 9.28 (s, 6H), 9.19 (s, 4H), 9.04 – 8.83 (m, 8H), 8.77 – 8.50 (m, 10H), 8.40 – 8.21 (m, 9H), 8.16 – 7.98 (m, 14H), 7.90 (td, *J* = 7.9, 1.5 Hz, 3H), 7.78 (td, *J* = 7.9, 1.5 Hz, 3H), 7.74 – 7.60 (m, 6H), 7.53 (dd, *J* = 5.3, 1.5 Hz, 2H), 7.46 – 7.35 (m, 8H), 7.31 (td, *J* = 6.5, 6.0, 1.4 Hz, 3H), 7.21 (t, *J* = 7.2 Hz, 3H), 7.09 (ddd, *J* = 7.4, 5.8, 1.4 Hz, 3H), 4.79 (d, *J* = 8.3 Hz, 2H).

Figure 44. AlPor-Ru proton NMR.

AlPor-Ru. ^{1}H NMR (400 MHz,) δ 10.12 (dd, *J* = 5.4, 1.5 Hz, 2H), 9.40 (s, 8H), 9.35 (q, *J* = 5.8, 5.2 Hz, 2H), 9.28 (s, 6H), 9.19 (s, 4H), 9.04 – 8.83 (m, 8H), 8.77 – 8.50 (m, 10H), 8.40 – 8.21 (m, 9H), 8.16 – 7.98 (m, 14H), 7.90 (td, *J* = 7.9, 1.5 Hz, 3H), 7.78 (td, *J* = 7.9, 1.5 Hz, 3H), 7.74 – 7.60 (m, 6H), 7.53 (dd, *J* = 5.3, 1.5 Hz, 2H), 7.46 – 7.35 (m, 8H), 7.31 (td, *J* = 6.5, 6.0, 1.4 Hz, 3H), 7.21 (t, *J* = 7.2 Hz, 3H), 7.09 (ddd, *J* = 7.4, 5.8, 1.4 Hz, 3H), 4.79 (d, *J* = 8.3 Hz, 2H).

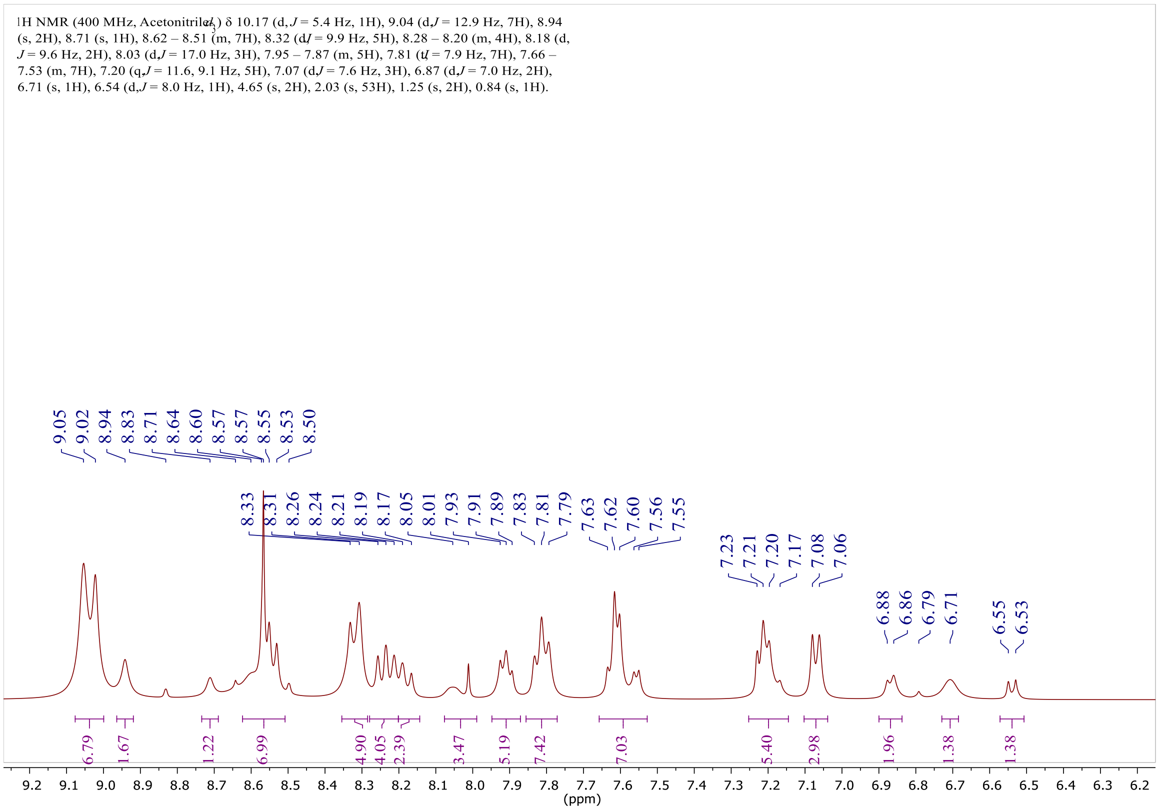

1H NMR (400 MHz, Acetonitrile-d_3) δ 10.17 (d, *J* = 5.4 Hz, 1H), 9.04 (d, *J* = 12.9 Hz, 7H), 8.94 (s, 2H), 8.71 (s, 1H), 8.62 – 8.51 (m, 7H), 8.32 (d, *J* = 9.9 Hz, 5H), 8.28 – 8.20 (m, 4H), 8.18 (d, *J* = 9.6 Hz, 2H), 8.03 (d, *J* = 17.0 Hz, 3H), 7.95 – 7.87 (m, 5H), 7.81 (t, *J* = 7.9 Hz, 7H), 7.66 – 7.53 (m, 7H), 7.20 (q, *J* = 11.6, 9.1 Hz, 5H), 7.07 (d, *J* = 7.6 Hz, 3H), 6.87 (d, *J* = 7.0 Hz, 2H), 6.71 (s, 1H), 6.54 (d, *J* = 8.0 Hz, 1H), 4.65 (s, 2H), 2.03 (s, 53H), 1.25 (s, 2H), 0.84 (s, 1H).

Figure 45. AlPorF3-Ru proton NMR.

AlPorF3-Ru. ^{1}H NMR (400 MHz,) δ 10.12 (dd, *J* = 5.4, 1.5 Hz, 2H), 9.40 (s, 8H), 9.35 (q, *J* = 5.8, 5.2 Hz, 2H), 9.28 (s, 6H), 9.19 (s, 4H), 9.04 – 8.83 (m, 8H), 8.77 – 8.50 (m, 10H), 8.40 – 8.21 (m, 9H), 8.16 – 7.98 (m, 14H), 7.90 (td, *J* = 7.9, 1.5 Hz, 3H), 7.78 (td, *J* = 7.9, 1.5 Hz, 3H), 7.74 – 7.60 (m, 6H), 7.53 (dd, *J* = 5.3, 1.5 Hz, 2H), 7.46 – 7.35 (m, 8H), 7.31 (td, *J* = 6.5, 6.0, 1.4 Hz, 3H), 7.21 (t, *J* = 7.2 Hz, 3H), 7.09 (ddd, *J* = 7.4, 5.8, 1.4 Hz, 3H), 4.79 (d, *J* = 8.3 Hz, 2H).

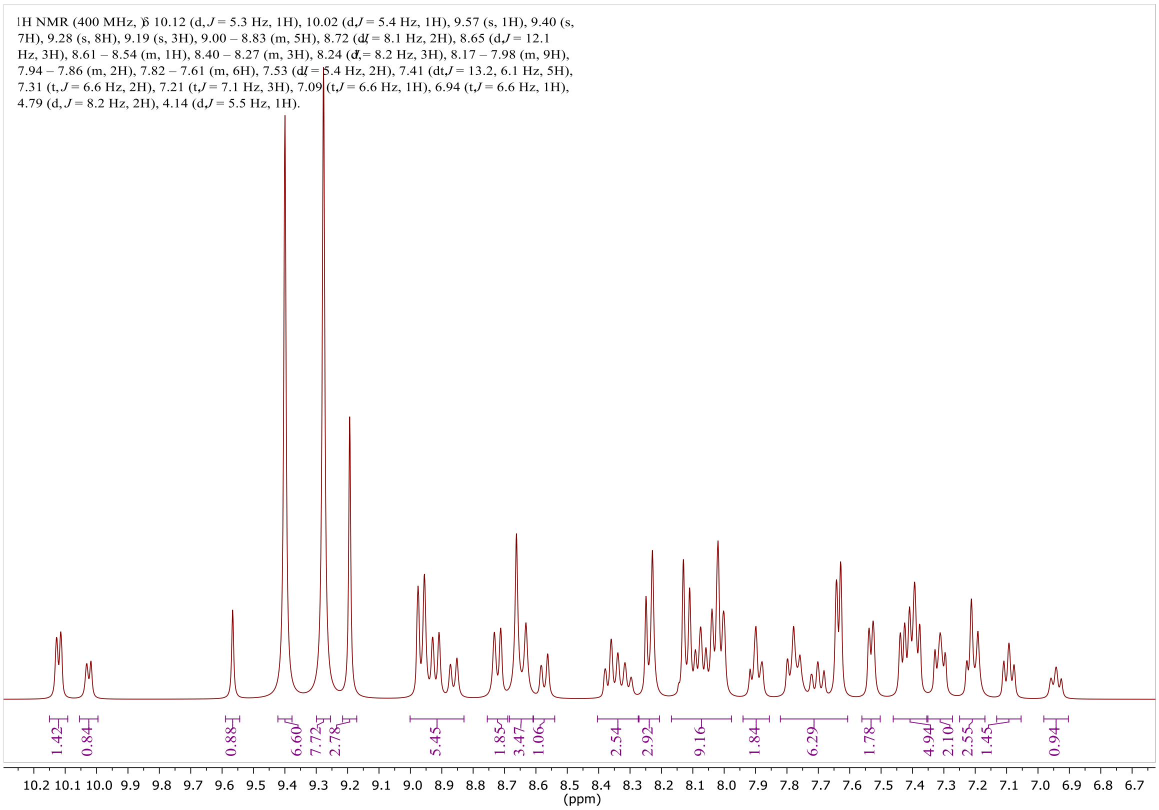

Figure 46. AlPorF5-Ru proton NMR.

AlPorF5-Ru. ^{1}H NMR (400 MHz,) δ 10.12 (d, *J* = 5.3 Hz, 1H), 10.02 (d, *J* = 5.4 Hz, 1H), 9.57 (s, 1H), 9.40 (s, 7H), 9.28 (s, 8H), 9.19 (s, 3H), 9.00 – 8.83 (m, 5H), 8.72 (d, *J* = 8.1 Hz, 2H), 8.65 (d, *J* = 12.1 Hz, 3H), 8.61 – 8.54 (m, 1H), 8.40 – 8.27 (m, 3H), 8.24 (d, *J* = 8.2 Hz, 3H), 8.17 – 7.98 (m, 9H), 7.94 – 7.86 (m, 2H), 7.82 – 7.61 (m, 6H), 7.53 (d, *J* = 5.4 Hz, 2H), 7.41 (dt, *J* = 13.2, 6.1 Hz, 5H), 7.31 (t, *J* = 6.6 Hz, 2H), 7.21 (t, *J* = 7.1 Hz, 3H), 7.09 (t, *J* = 6.6 Hz, 1H), 6.94 (t, *J* = 6.6 Hz, 1H), 4.79 (d, *J* = 8.2 Hz, 2H), 4.14 (d, *J* = 5.5 Hz, 1H).

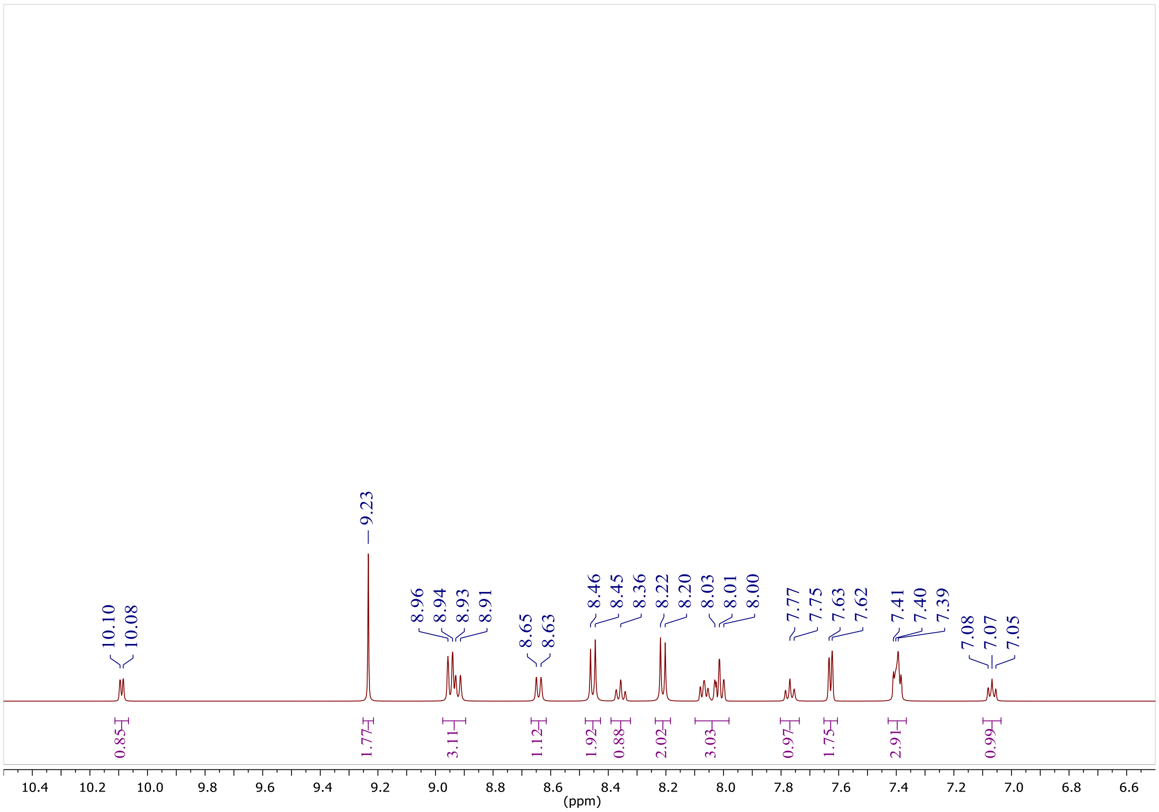

Figure 47. Ru-Me proton NMR.

Ru-Me. ^{1}H NMR (500 MHz,) δ 10.09 (d, *J* = 5.5 Hz, 1H), 9.23 (s, 2H), 8.94 (dd, *J* = 13.6, 8.2 Hz, 3H), 8.64 (d, *J* = 8.2 Hz, 1H), 8.45 (d, *J* = 8.3 Hz, 2H), 8.36 (t, *J* = 7.8 Hz, 1H), 8.21 (d, *J* = 8.2 Hz, 2H), 8.10 – 7.98 (m, 3H), 7.77 (t, *J* = 7.5 Hz, 1H), 7.63 (d, *J* = 5.5 Hz, 2H), 7.40 (q, *J* = 4.6 Hz, 3H), 7.07 (t, *J* = 6.7 Hz, 1H).

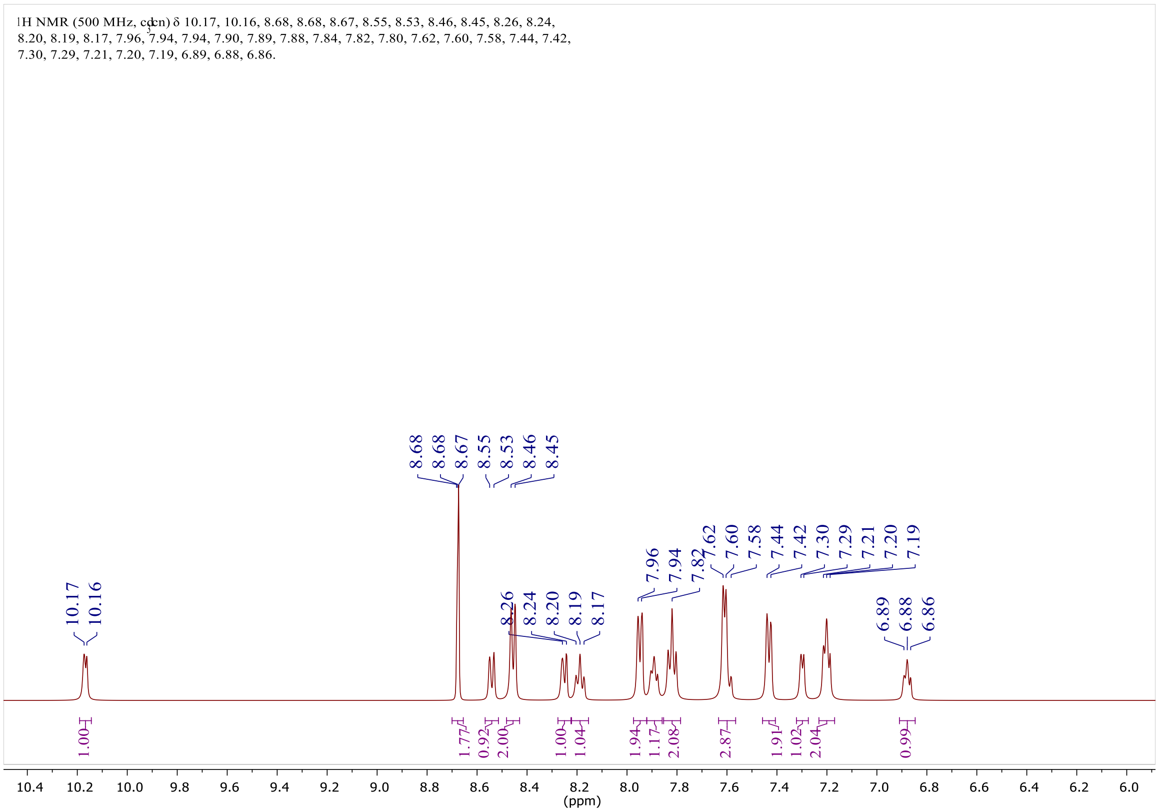

Figure 48. RuCOONa proton NMR.

Ru-COONa. ^{1}H NMR (500 MHz, cd$_3$cn) δ 10.17, 10.16, 8.68, 8.68, 8.67, 8.55, 8.53, 8.46, 8.45, 8.26, 8.24, 8.20, 8.19, 8.17, 7.96, 7.94, 7.94, 7.90, 7.89, 7.88, 7.84, 7.82, 7.80, 7.62, 7.60, 7.58, 7.44, 7.42, 7.30, 7.29, 7.21, 7.20, 7.19, 6.89, 6.88, 6.86.

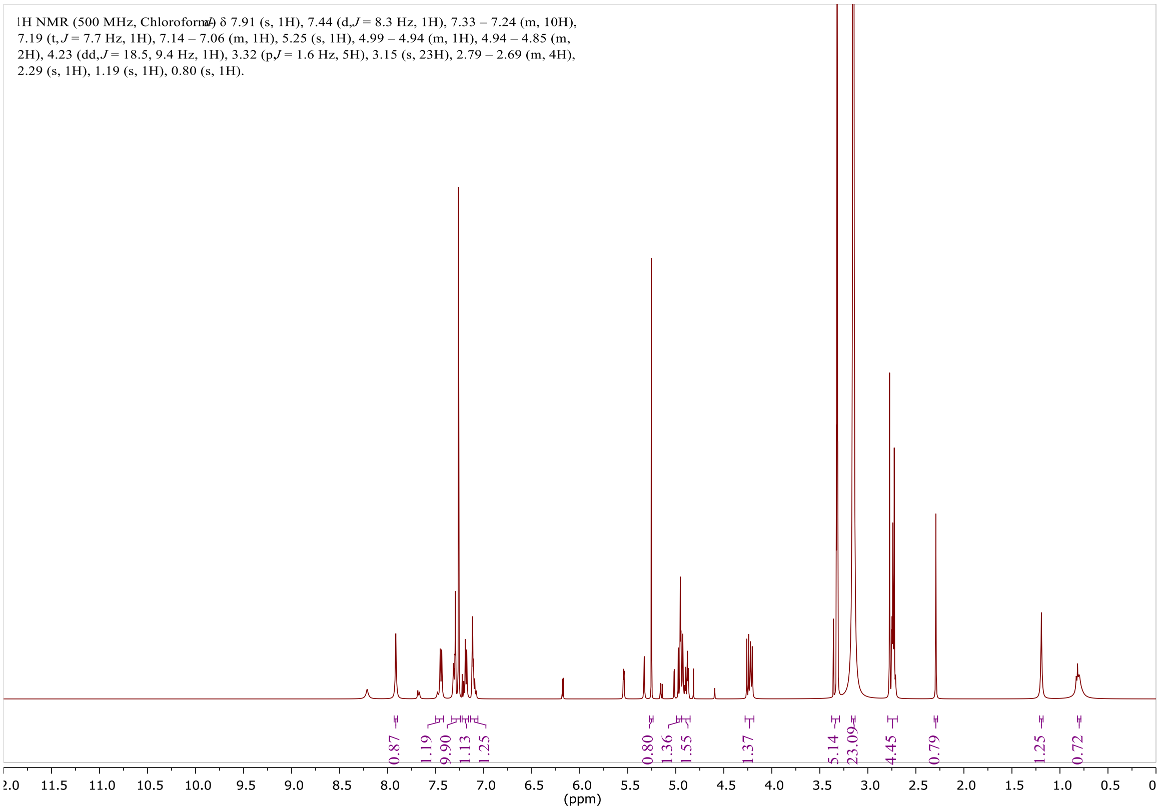
1H NMR (500 MHz, Chloroform-d) δ 7.91 (s, 1H), 7.44 (d, J = 8.3 Hz, 1H), 7.33 – 7.24 (m, 10H), 7.19 (t, J = 7.7 Hz, 1H), 7.14 – 7.06 (m, 1H), 5.25 (s, 1H), 4.99 – 4.94 (m, 1H), 4.94 – 4.85 (m, 2H), 4.23 (dd, J = 18.5, 9.4 Hz, 1H), 3.32 (p, J = 1.6 Hz, 5H), 3.15 (s, 23H), 2.79 – 2.69 (m, 4H), 2.29 (s, 1H), 1.19 (s, 1H), 0.80 (s, 1H).

Figure 49. C_{60}-Im proton NMR.

C_{60}-Im. ^{1}H NMR (500 MHz, Chloroform-*d*) δ 7.91 (s, 1H), 7.44 (d, *J* = 8.3 Hz, 1H), 7.33 – 7.24 (m, 10H), 7.19 (t, *J* = 7.7 Hz, 1H), 7.14 – 7.06 (m, 1H), 5.25 (s, 1H), 4.99 – 4.94 (m, 1H), 4.94 – 4.85 (m, 2H), 4.23 (dd, *J* = 18.5, 9.4 Hz, 1H), 3.32 (p, *J* = 1.6 Hz, 5H), 3.15 (s, 23H), 2.79 – 2.69 (m, 4H), 2.29 (s, 1H), 1.19 (s, 1H), 0.80 (s, 1H).

6.2 OPTICAL DATA

All UV-Vis absorption data taken in acetonitrile (excluding the titration data). All fluorescence data gathered with an excitation wavelength of 560 nm.

6.2.1 UV-VIS

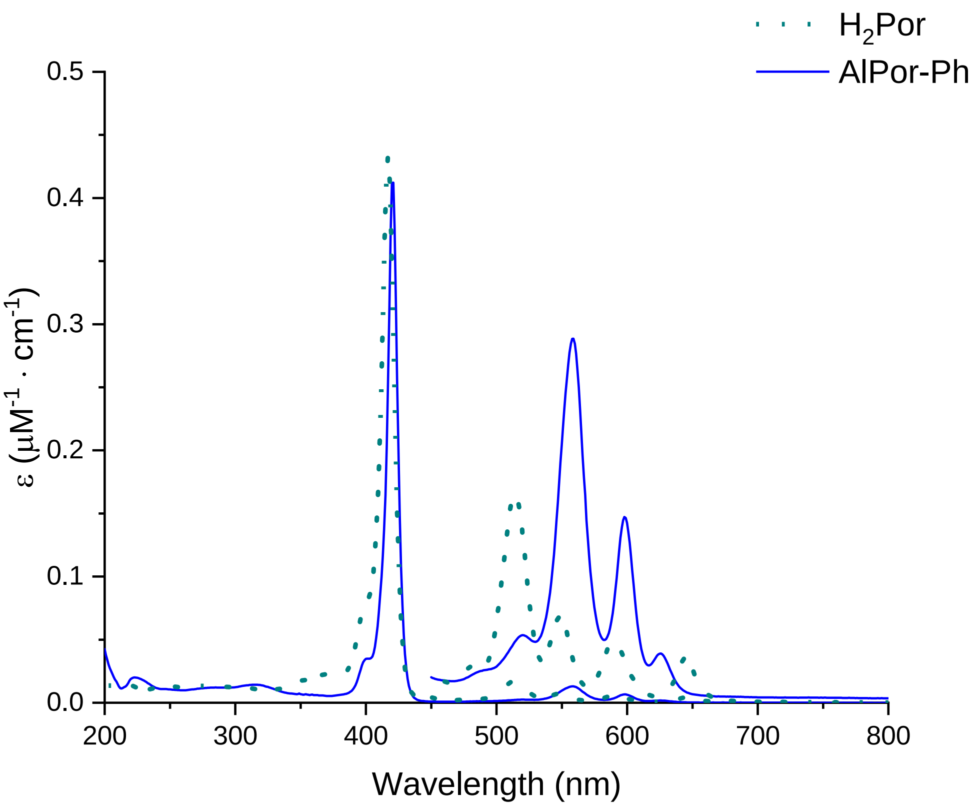

UV-Vis absorption spectra of H_2Por and AlPor-OH. Solvent = acetonitrile.

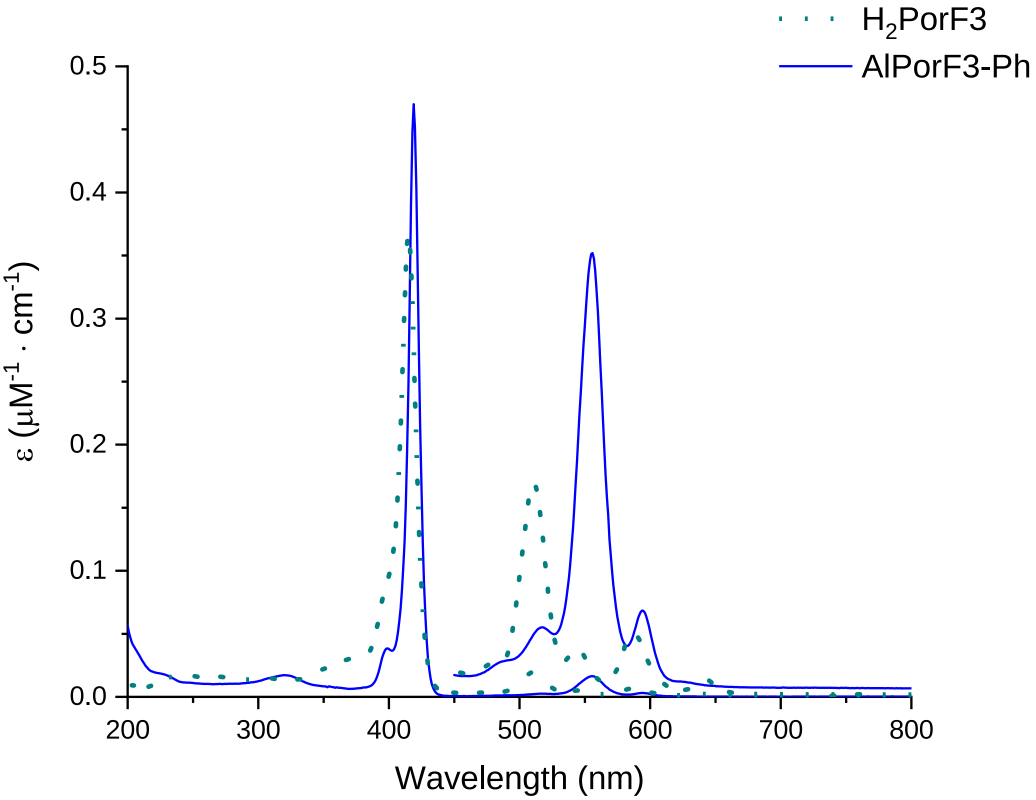

UV-Vis absorption spectra of H_2PorF3 and AlPorF3-OH. Solvent = acetonitrile.

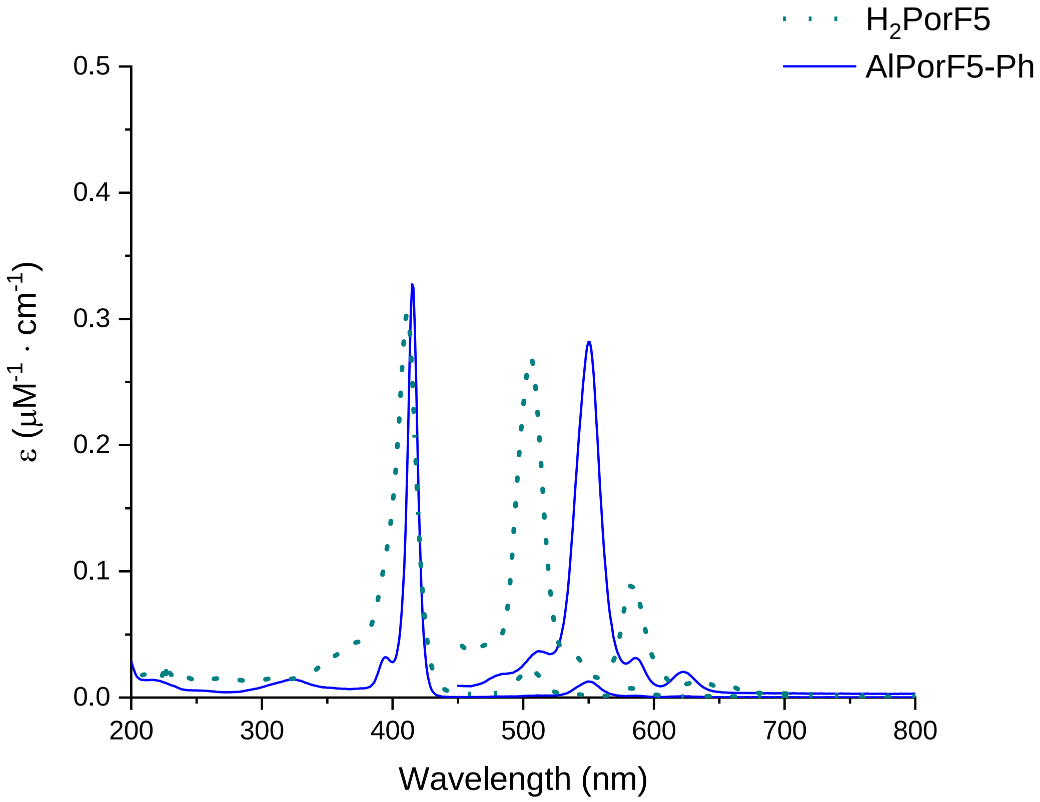

Figure 50. UV-Vis absorption spectra of H2PorF5 and AlPorF5-OH.

UV-Vis absorption spectra of H_2PorF5 and AlPorF5-OH. Solvent = acetonitrile.

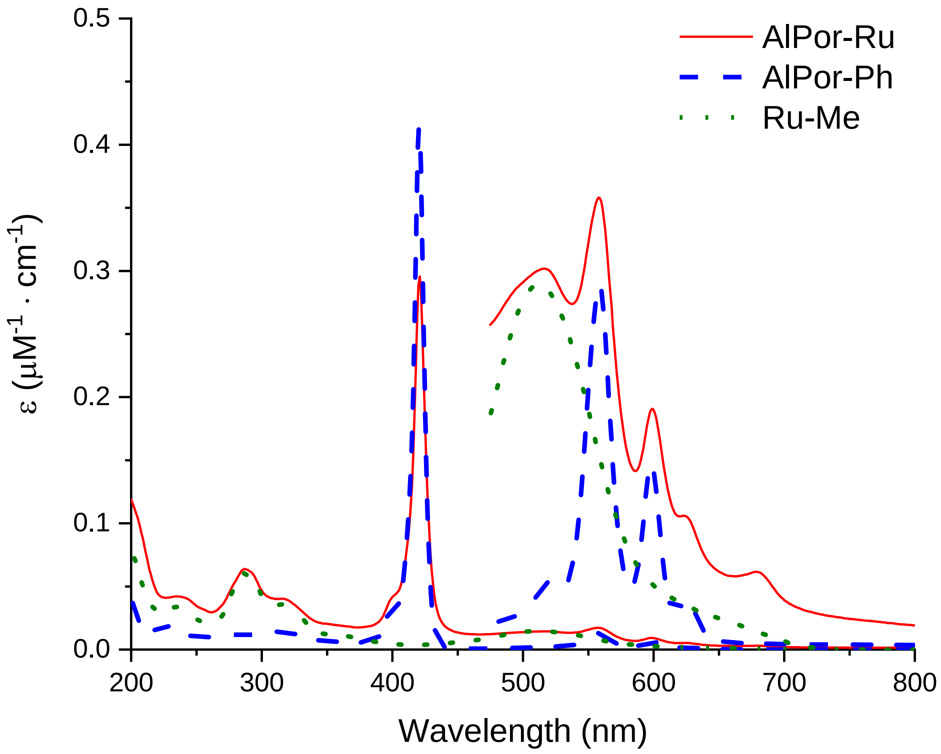

Figure 51. UV-Vis absorption spectra of AlPor-Ph, AlPor-Ru, and Ru-Me.

UV-Vis absorption spectra of AlPor-Ph, AlPor-Ru, and Ru-Me. Solvent = acetonitrile.

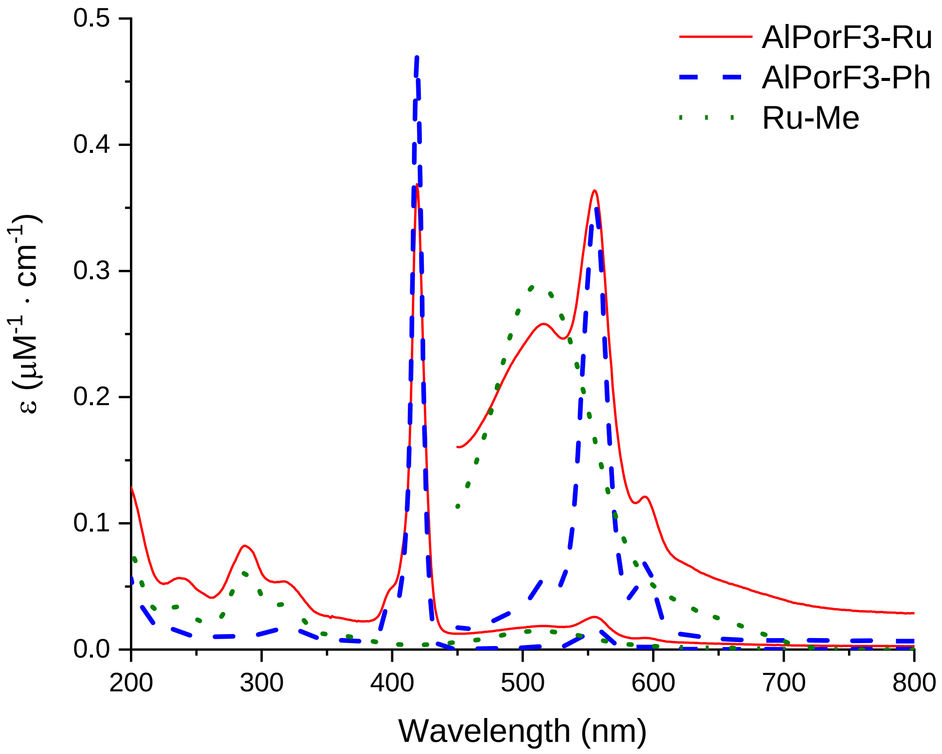

UV-Vis absorption spectra of AlPorF3-Ph, AlPorF3-Ru, and Ru-Me. Solvent = acetonitrile.

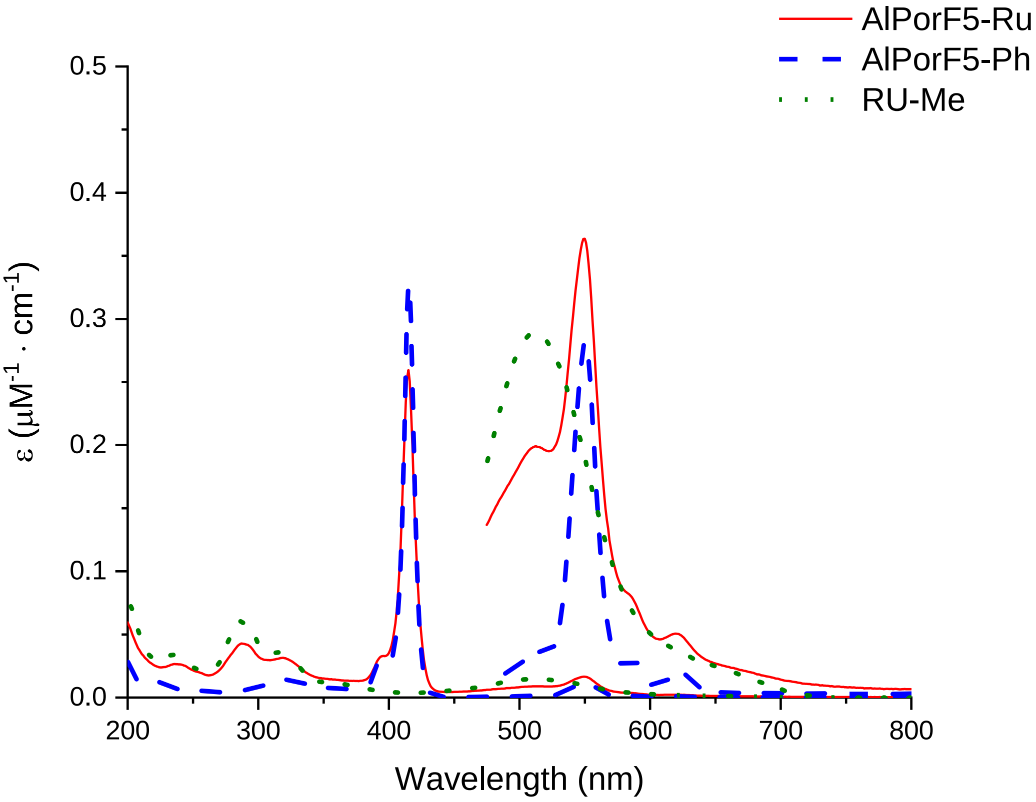

Figure 52. UV-Vis absorption spectra of AlPorF5-Ph, AlPorF5-Ru, and Ru-Me.

UV-Vis absorption spectra of AlPorF5-Ph, AlPorF5-Ru, and Ru-Me. Solvent = acetonitrile.

6.2.2 FLUORESCENCE SPECTRA

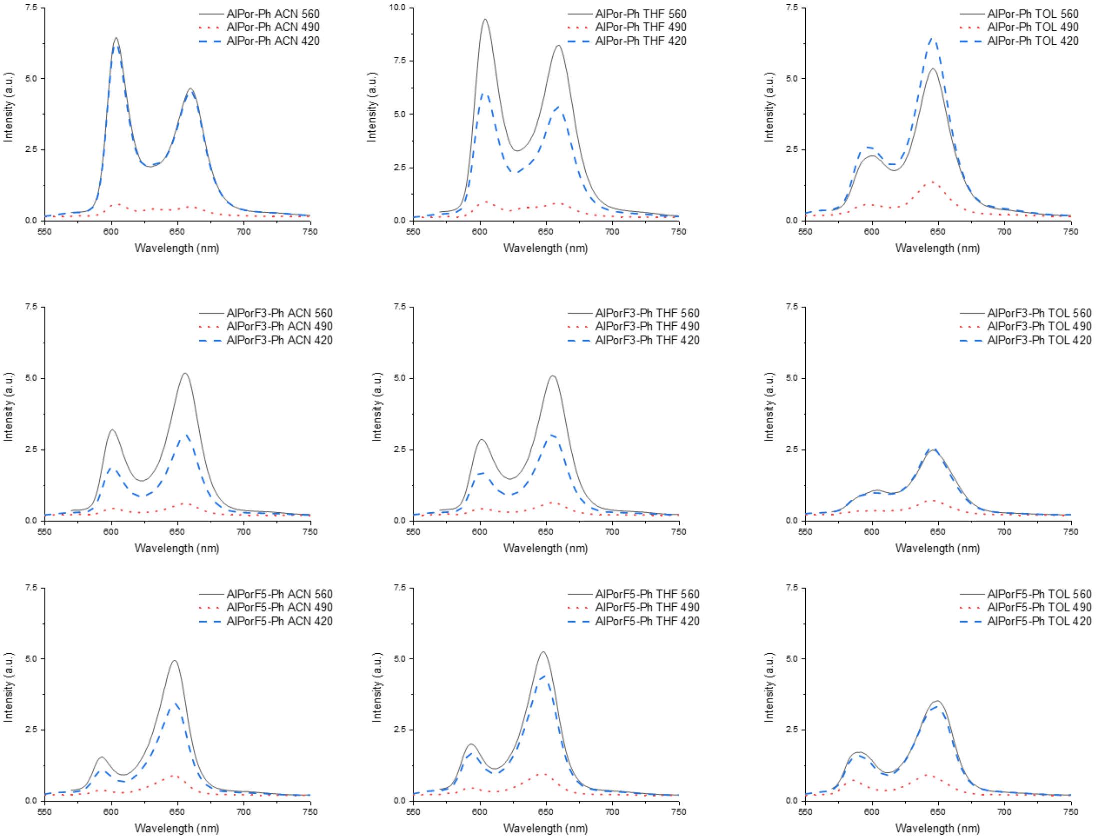

Figure 53. Fluorescence spectra of reference porphyrins at various excitation wavelengths.

Fluorescence spectra of the reference porphyrins, comparing the effects of different excitation wavelengths on intensity.

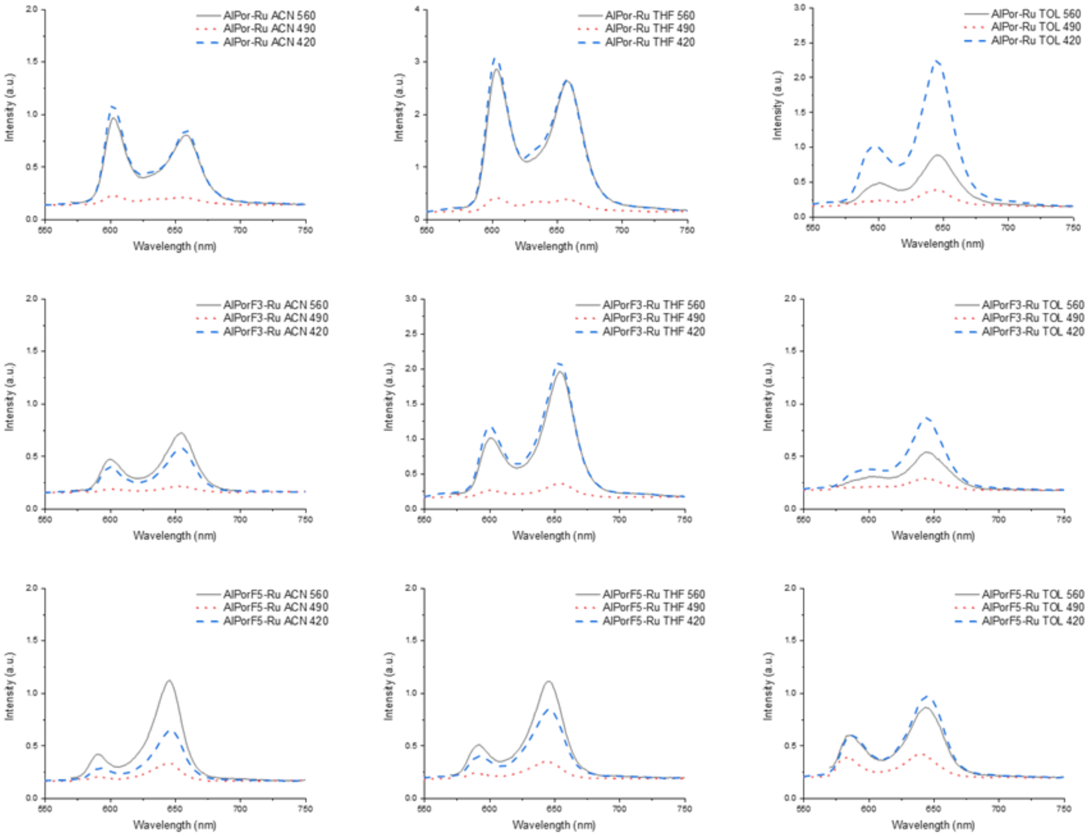

Figure 54. Fluorescence spectra of the catalytic dyads at various excitation wavelengths.

Fluorescence spectra of the dyads, comparing the effects of different excitation wavelengths on intensity.

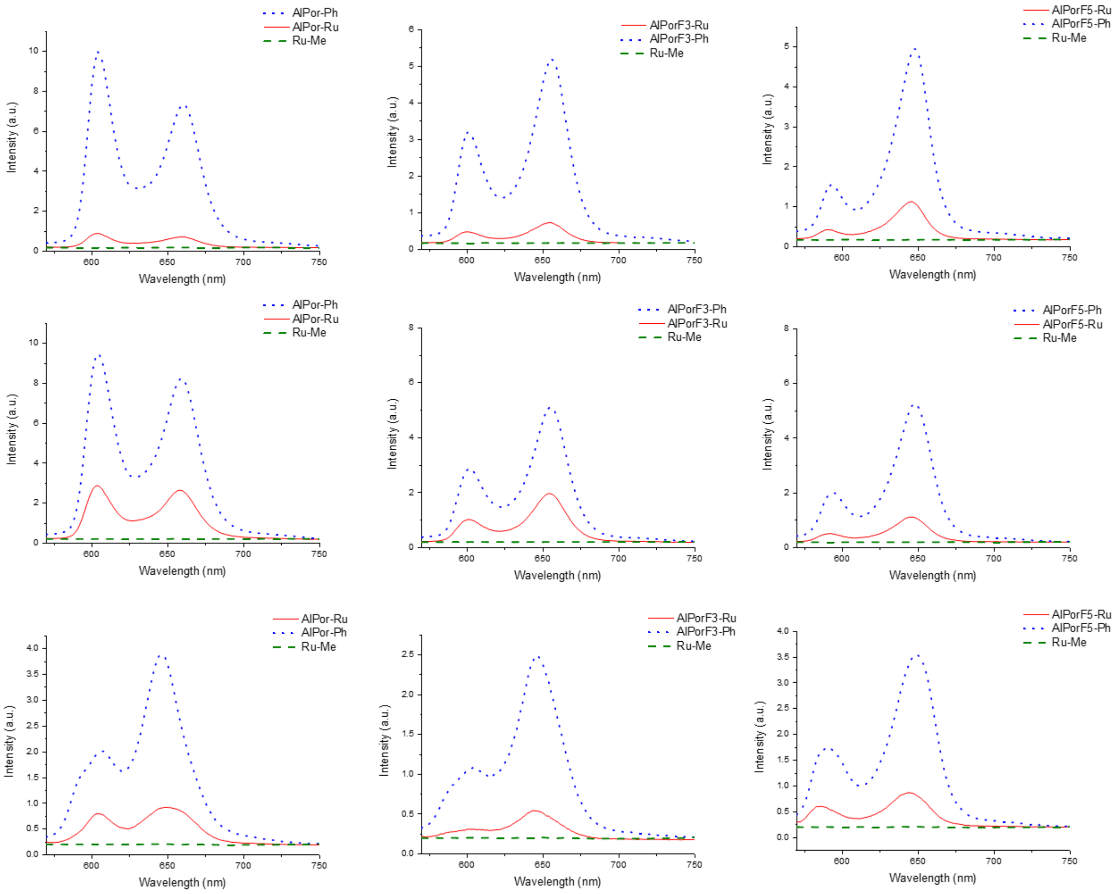

Figure 55. Fluorescence spectra of each catalytic dyads vs. its relevant reference compounds. (Excitation wavelength = 560 nm).

Fluorescence quenching: comparison of the fluorescence of the catalytic dyads to the reference porphyrins. Excitation = 560 nm. The solvents are as follows: top row = acetonitrile; middle row = tetrahydrofuran; bottom row = toluene. All spectra taken at room temperature.

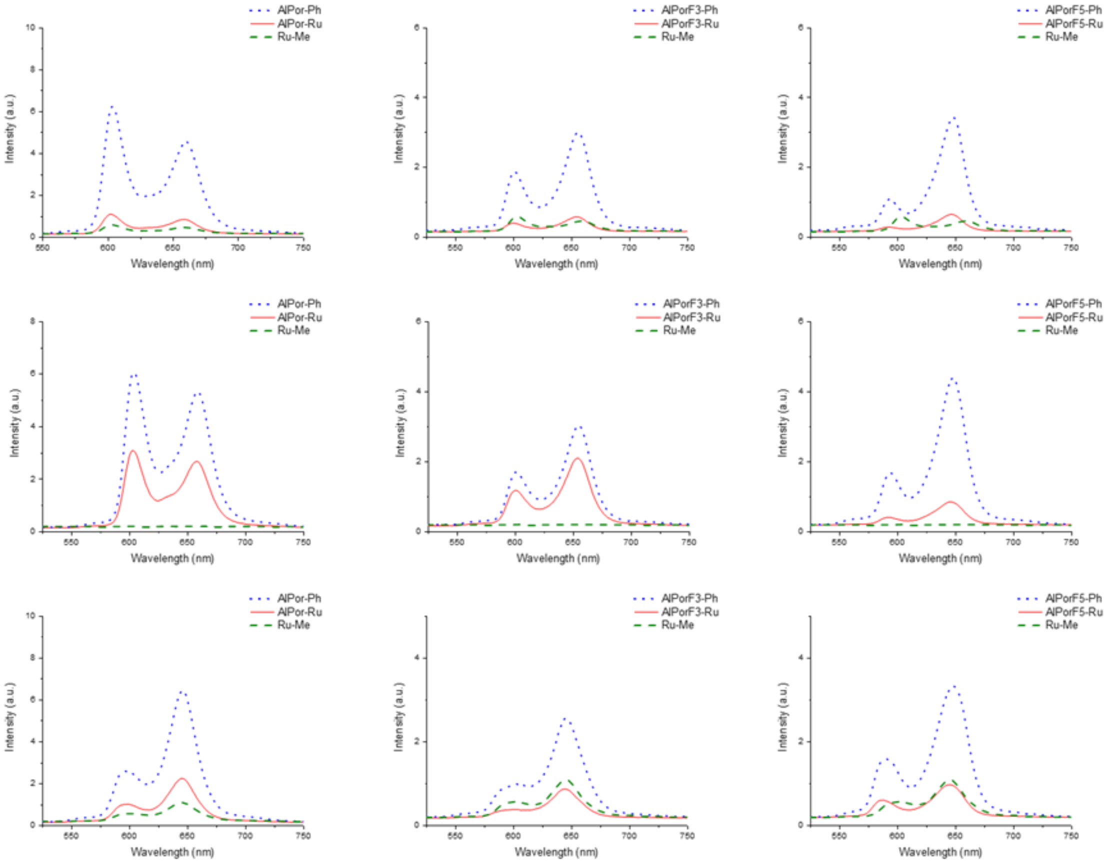

Figure 56. Fluorescence spectra of each catalytic dyads vs. its relevant reference compounds. (Excitation wavelength = 420 nm).

Fluorescence quenching: comparison of the fluorescence of the catalytic dyads to the reference porphyrins. Excitation = 420 nm. The solvents are as follows: top row = acetonitrile; middle row = tetrahydrofuran; bottom row = toluene. All spectra taken at room temperature.

6.2.3 DETERMINATION OF 0-0 TRANSITION ENERGY

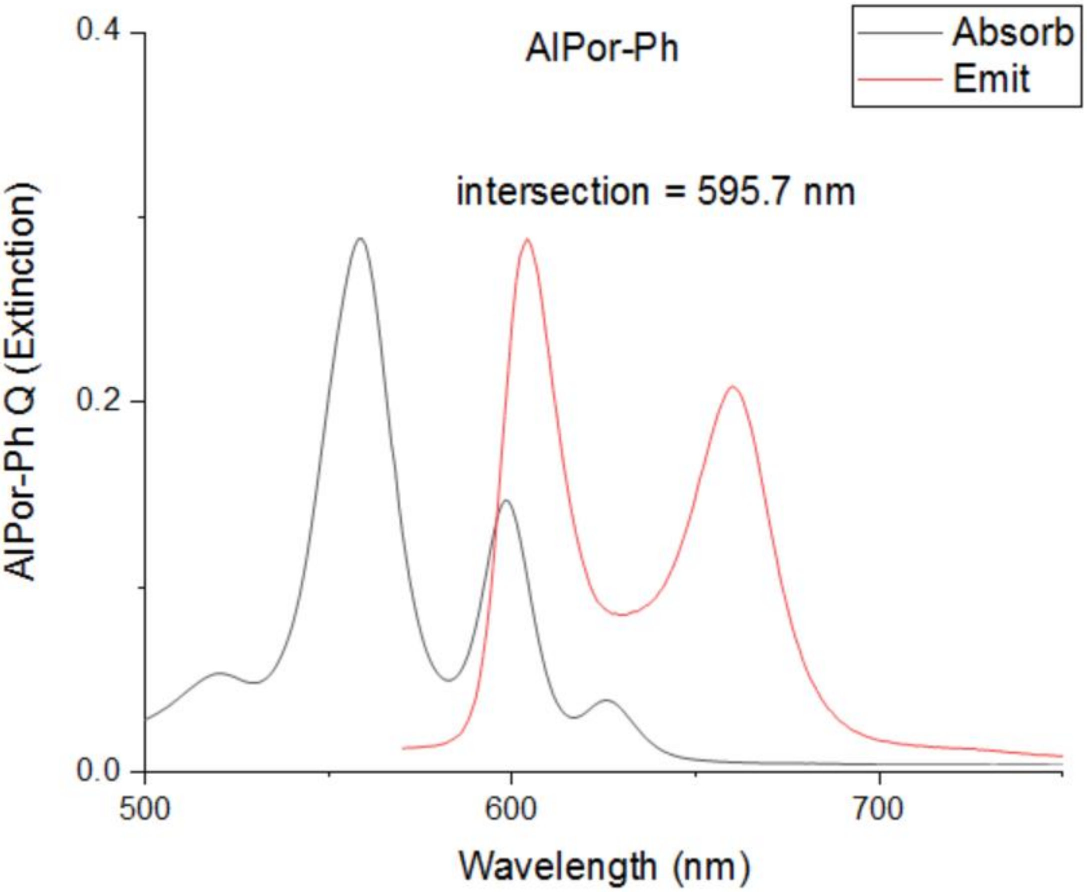

Figure 57. Absorption and emission spectra of AlPor-Ph.

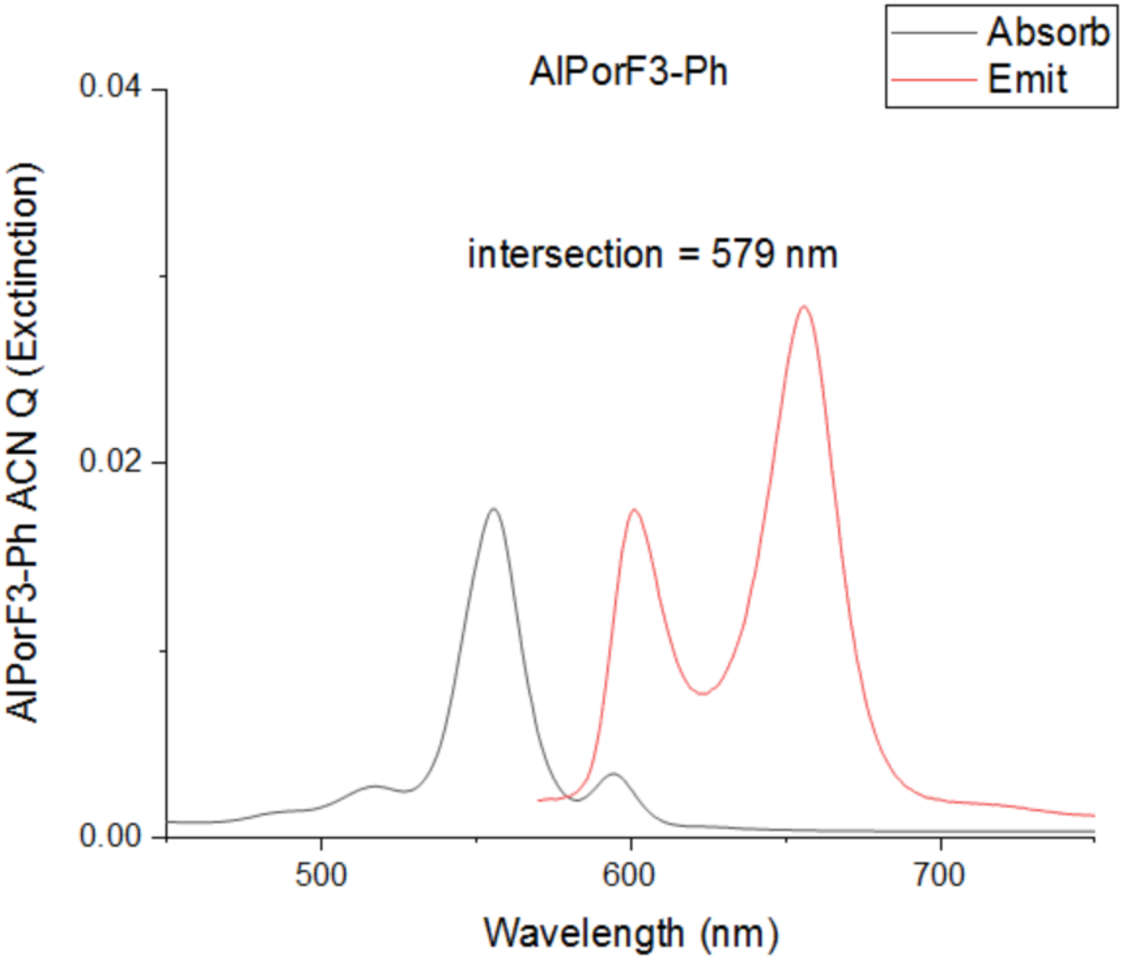

Figure 58. Absorption and emission spectra of AlPorF3-Ph.

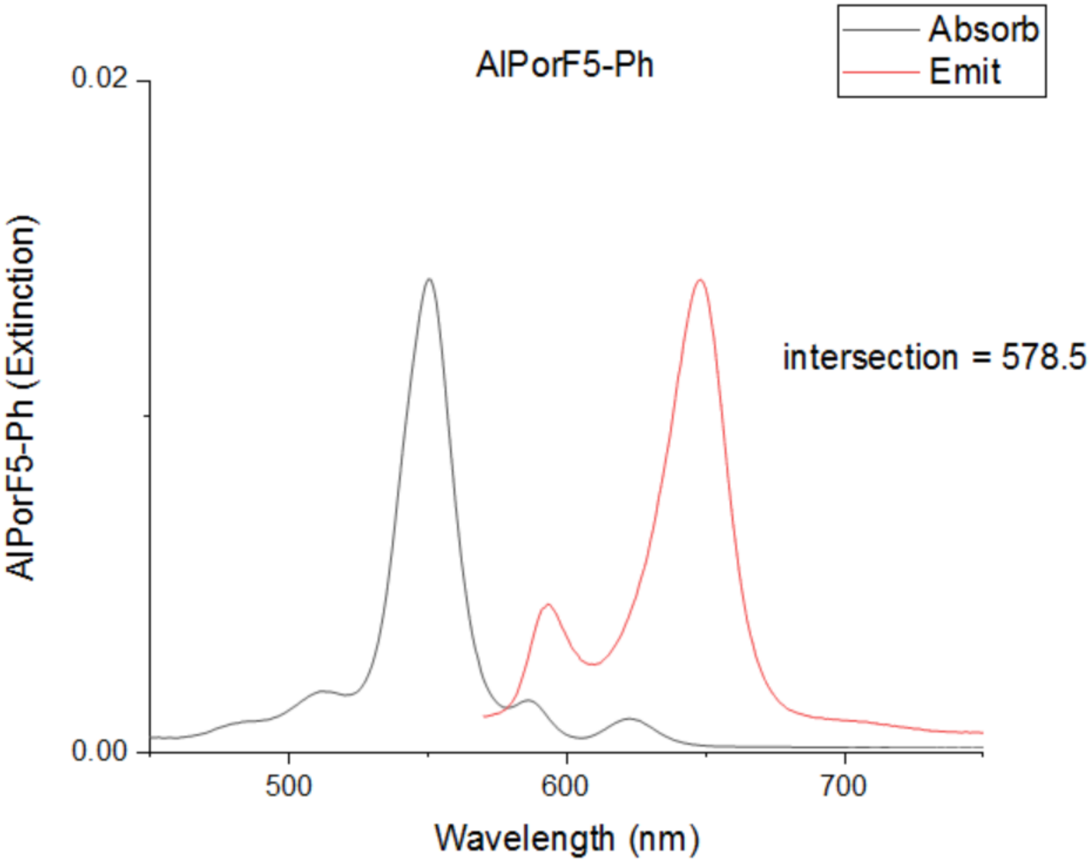

Figure 59. Absorption and emission spectra of AlPorF5-Ph.

6.4 ELECTROCHEMISTRY

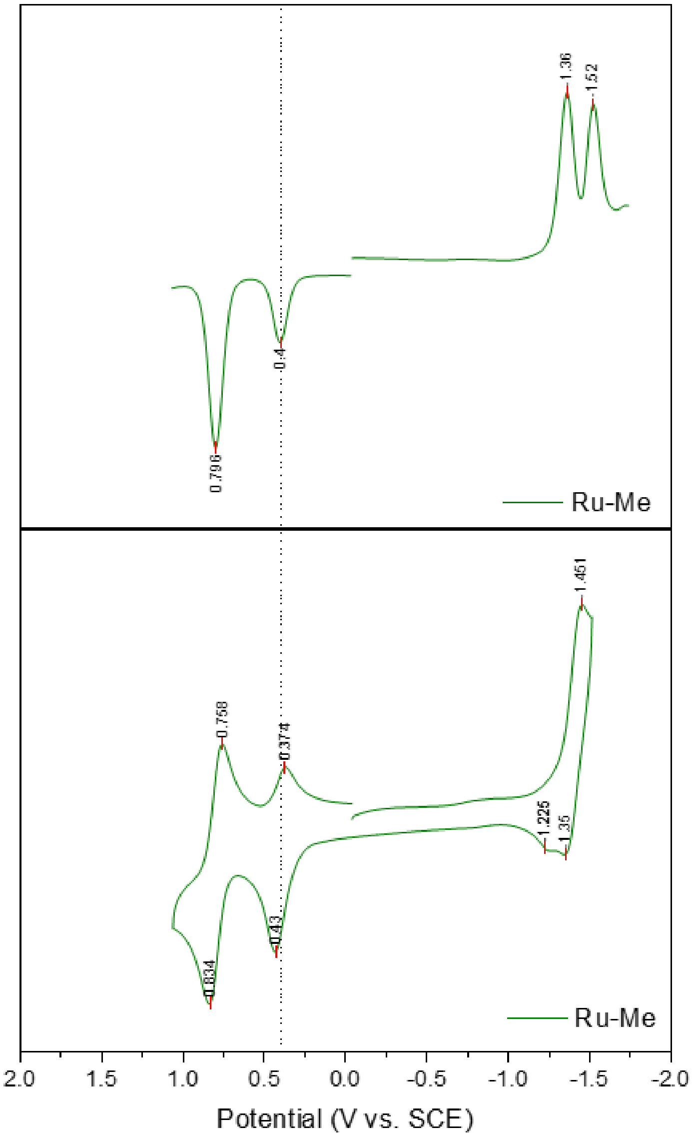

Figure 60. DPV and CV of Ru-Me.

Top: differential pulse voltammogram. Solvent: 0.1 M TBAPF6 in ACN with Fc as an internal standard. Oxidation of Fc set to +0.4 mV (notated by dotted vertical line). Bottom: cyclic voltammograms. Solvent: 0.1 M TBAPF6 in acetonitrile with Fc as an internal standard. Oxidation of ferrocene set to +0.4 mV (notated by dotted vertical line). Scan rate = 100 mV/s

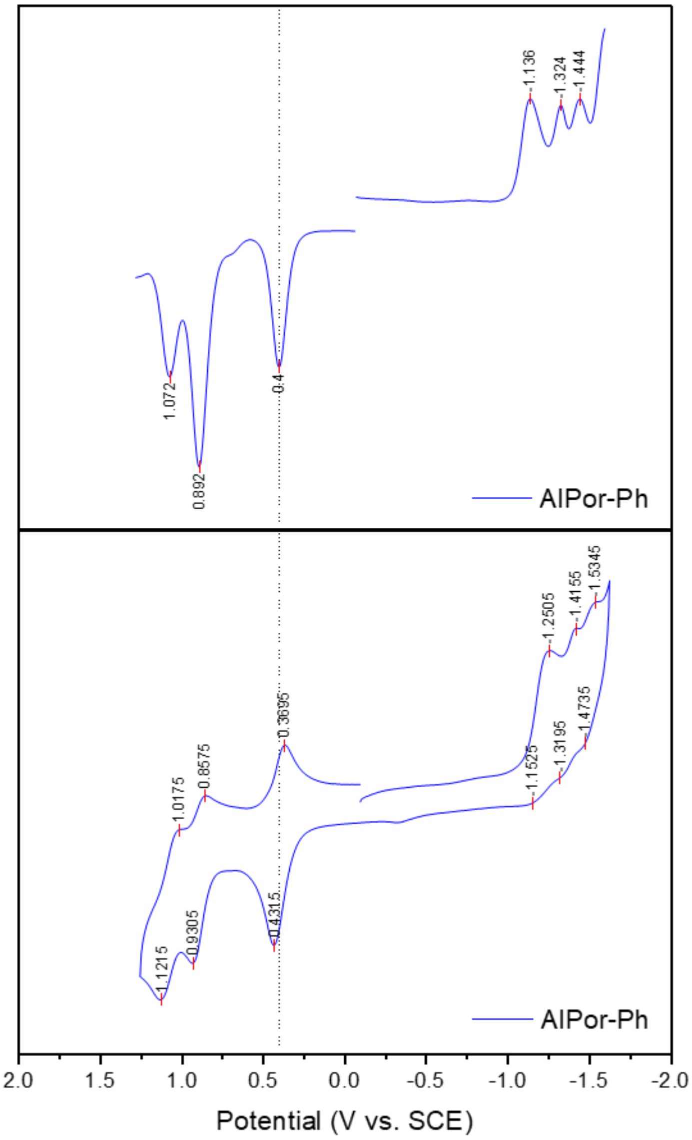

Figure 61. DPV and CV of AlPor-Ph.

Top: differential pulse voltammogram. Solvent: 0.1 M TBAPF6 in ACN with Fc as an internal standard. Oxidation of Fc set to +0.4 mV (notated by dotted vertical line).

Bottom: cyclic voltammograms. Solvent: 0.1 M TBAPF6 in acetonitrile with Fc as an internal standard. Oxidation of ferrocene set to +0.4 mV (notated by dotted vertical line). Scan rate = 100 mV/s

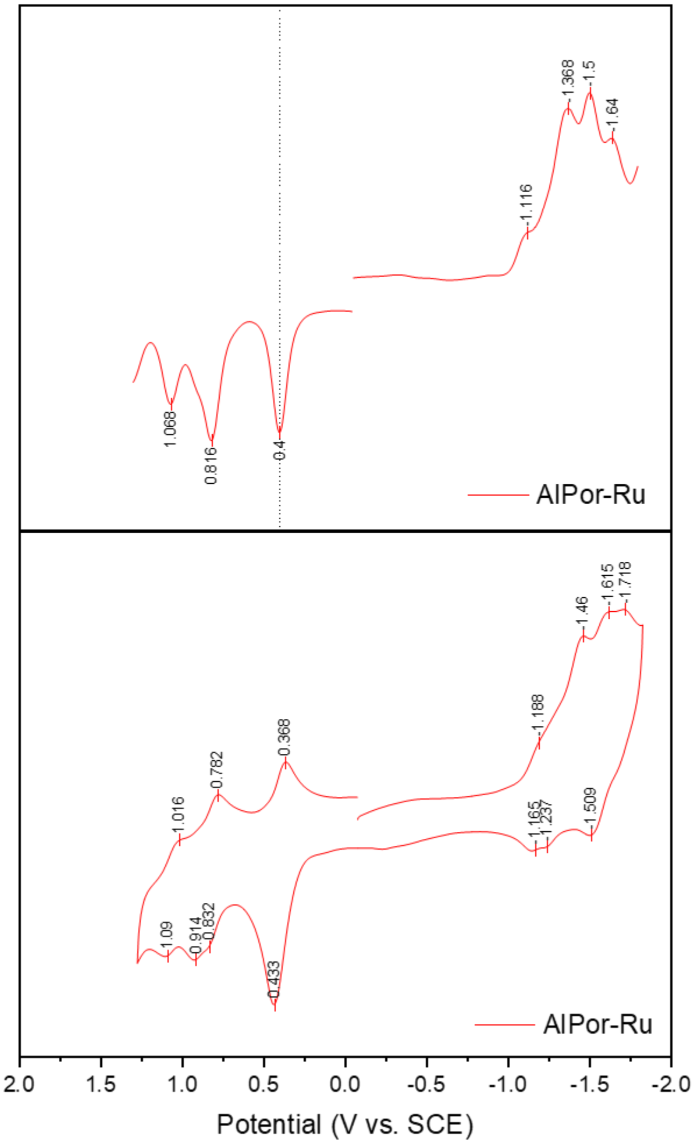

Figure 62. DPV and CV of AlPor-Ru.

Top: differential pulse voltammogram. Solvent: 0.1 M TBAPF6 in ACN with Fc as an internal standard. Oxidation of Fc set to +0.4 mV (notated by dotted vertical line).

Bottom: cyclic voltammograms. Solvent: 0.1 M TBAPF6 in acetonitrile with Fc as an internal standard. Oxidation of ferrocene set to +0.4 mV (notated by dotted vertical line). Scan rate = 100 mV/s

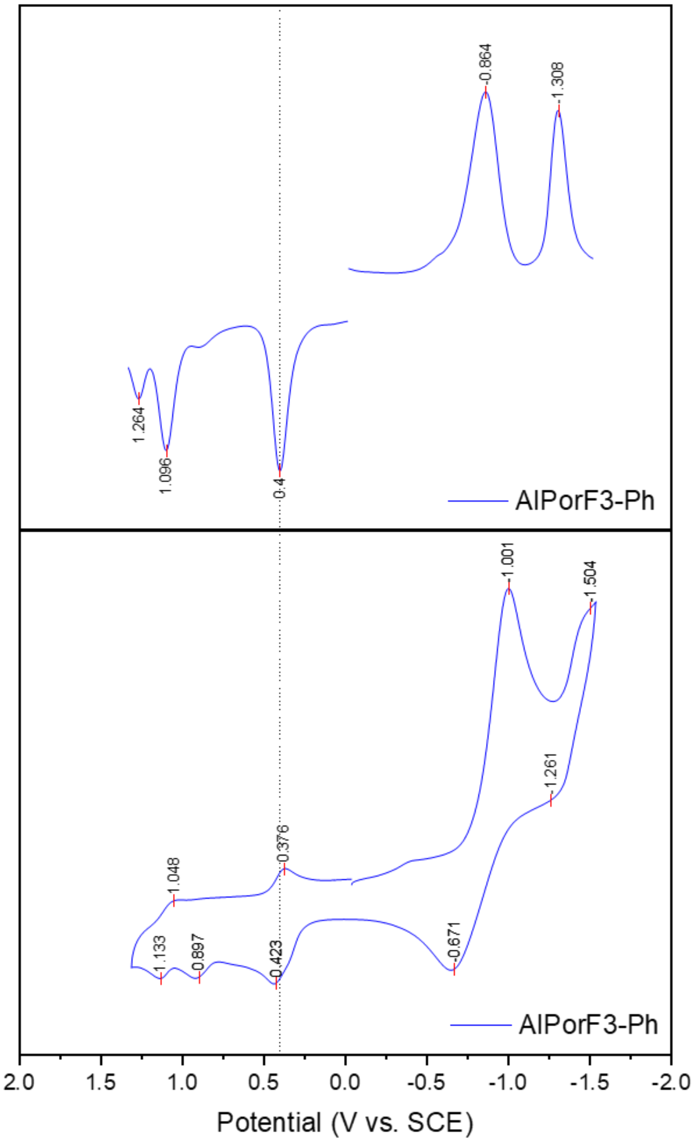

Figure 63. DPV and CV or AlPorF3-Ph.

Top: differential pulse voltammogram. Solvent: 0.1 M TBAPF6 in ACN with Fc as an internal standard. Oxidation of Fc set to +0.4 mV (notated by dotted vertical line).

Bottom: cyclic voltammograms. Solvent: 0.1 M TBAPF6 in acetonitrile with Fc as an internal standard. Oxidation of ferrocene set to +0.4 mV (notated by dotted vertical line). Scan rate = 100 mV/s

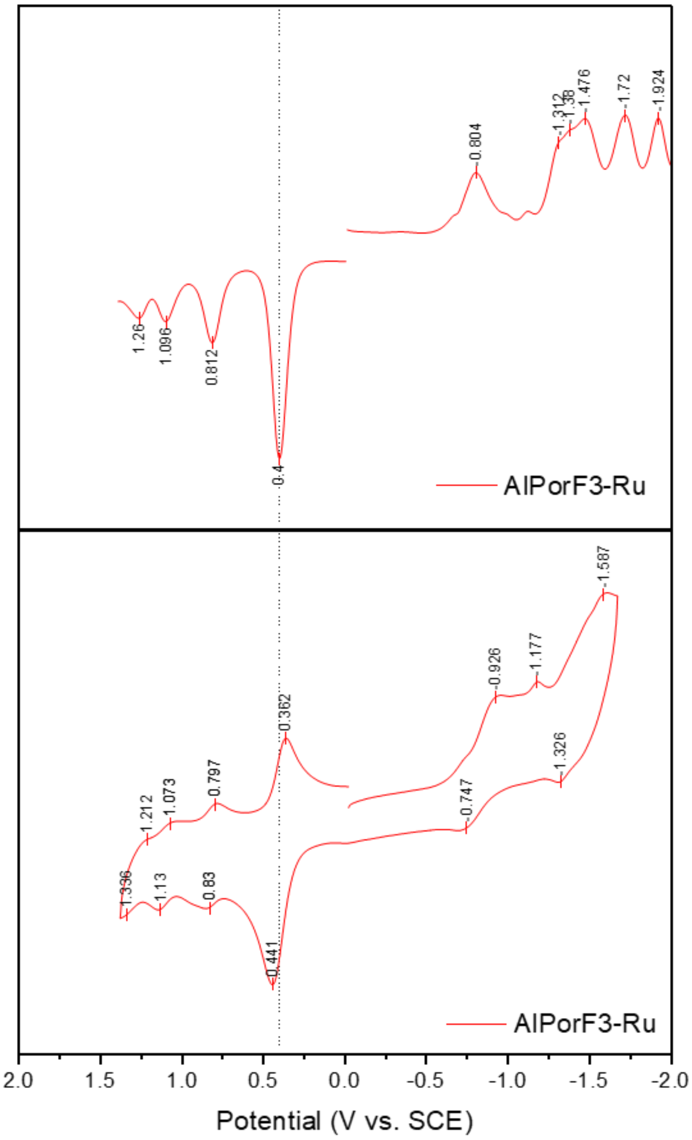

Figure 64. DPV and CV of AlPorF3-Ru.

Top: differential pulse voltammogram. Solvent: 0.1 M TBAPF6 in ACN with Fc as an internal standard. Oxidation of Fc set to +0.4 mV (notated by dotted vertical line).

Bottom: cyclic voltammograms. Solvent: 0.1 M TBAPF6 in acetonitrile with Fc as an internal standard. Oxidation of ferrocene set to +0.4 mV (notated by dotted vertical line). Scan rate = 100 mV/s

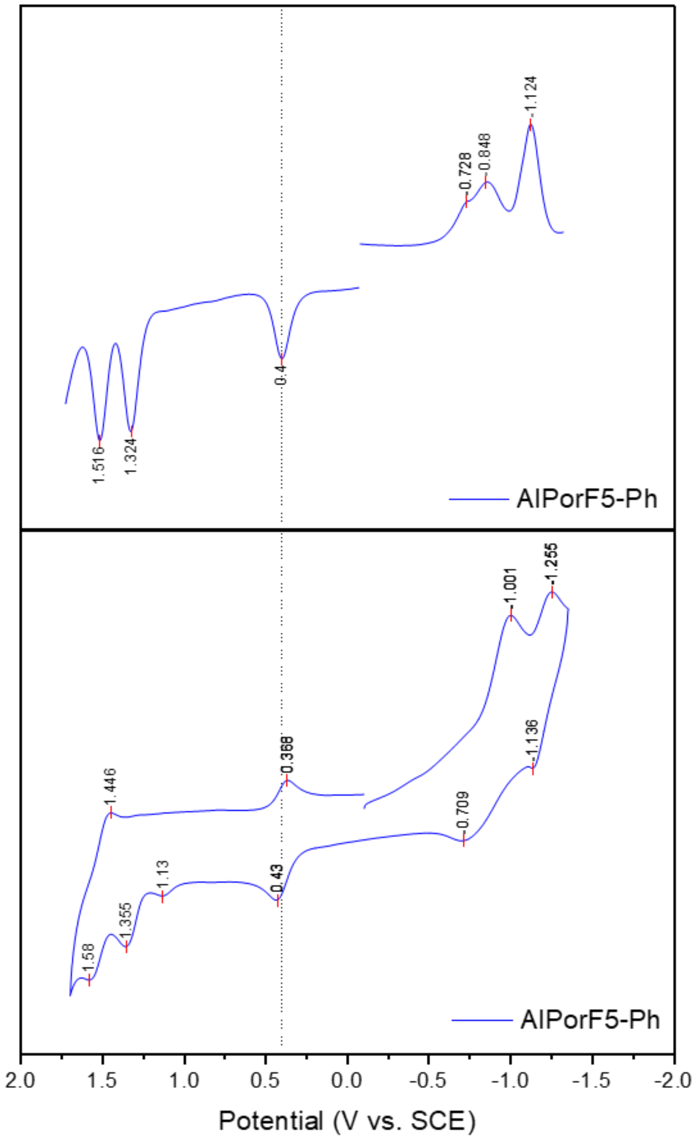

Figure 65. DPV and CV of AlPorF5-Ph.

Top: differential pulse voltammogram. Solvent: 0.1 M TBAPF6 in ACN with Fc as an internal standard. Oxidation of Fc set to +0.4 mV (notated by dotted vertical line).

Bottom: cyclic voltammograms. Solvent: 0.1 M TBAPF6 in acetonitrile with Fc as an internal standard. Oxidation of ferrocene set to +0.4 mV (notated by dotted vertical line). Scan rate = 100 mV/s

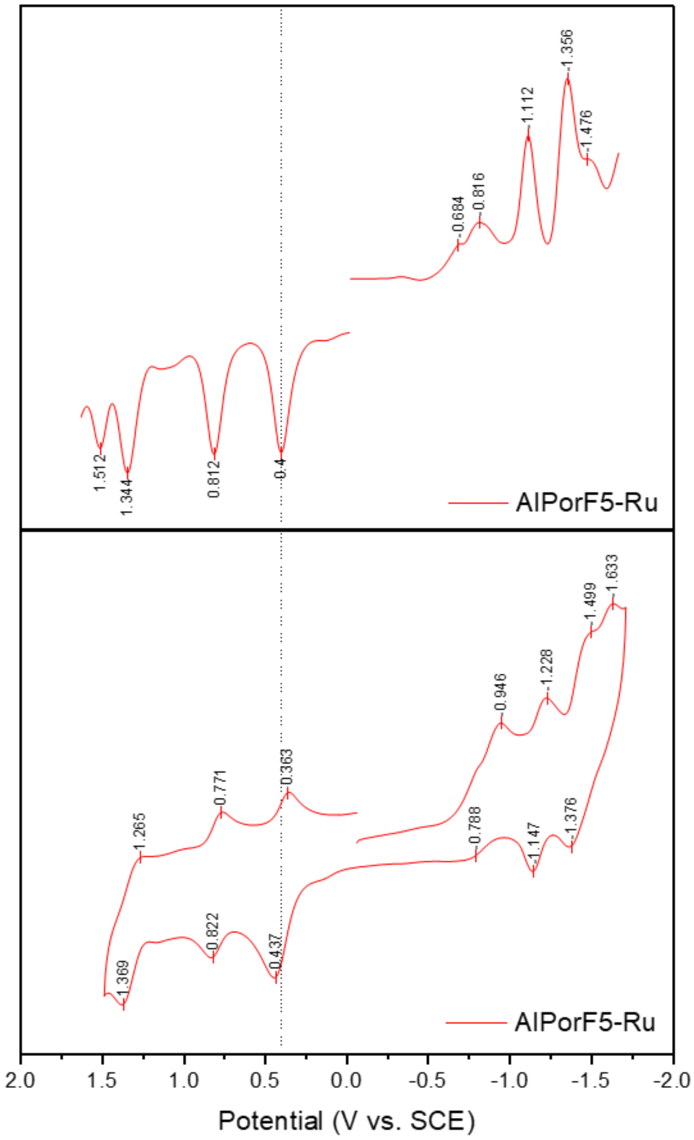

Figure 66. DPV and CV of AlPorF5-Ru.

Top: differential pulse voltammogram. Solvent: 0.1 M TBAPF6 in ACN with Fc as an internal standard. Oxidation of Fc set to +0.4 mV (notated by dotted vertical line).

Bottom: cyclic voltammograms. Solvent: 0.1 M TBAPF6 in acetonitrile with Fc as an internal standard. Oxidation of ferrocene set to +0.4 mV (notated by dotted vertical line). Scan rate = 100 mV/s